UPC CTTC

Development of CFD-based multi-fidelity surrogate models for indoor environmental applications

Heat and Mass Technological Centre
Departament de Màquines i Motors Tèrmics
Universitat Politècnica de Catalunya

Nina Morozova
Doctoral Thesis

Development of CFD-based multi-fidelity surrogate models for indoor environmental applications

Nina Morozova

PHD THESIS

submitted to the

Departament de Màquines i Motors Tèrmics
Escola Superior d’Enginyeries Industrial, Aeroespacial i Audiovisual de Terrassa
Universitat Politècnica de Catalunya

in partial fulfillment of the requirements for the degree of

Doctor of Philosophy in Thermal Engineering

Terrassa (Barcelona), June 2022

Development of CFD-based multi-fidelity surrogate models for indoor environmental applications

Nina Morozova

Thesis Supervisors

Prof. Assensi Oliva Llena
Prof. Francesc Xavier Trias Miguel

Committee Board

Dra. Anne Sergent
Sorbonne Universitė
Dr. Joaquim Rigola Serrano
Universitat Politècnica de Catalunya
Dr. Guilherme Carrilho Da Graça
Universidade de Lisboa

To my babushka Anya

Acknowledgements

I was born in a small miners' town located precisely in the middle of nowhere, where I attended Public School Number Two. Doing a PhD abroad was not an obvious life choice in the environment where I grew up. But somehow (with enormous efforts), I have found myself where I am now. This thesis would have been impossible without people that helped me along the way, so I would like to thank them here for their help and support.

I would like to thank Assensi Oliva - the head of CTTC, and my thesis director. Assensi, thank you for believing in me and admitting me into the CTTC family. I have spent very happy years under your supervision and guidance.

This thesis would have been absolutely impossible without my supervisor, coauthor, and friend Xavi Trias. Xavi, thank you for all the scientific and personal advice you gave me. If I ever become a Catedratic, it will be thanks to things that I learned from you. And also, thank you for the afternoon coffees, lunches in Ootoya, and Friday beers.

Roser, thank you for your support and guidance. Your remarks about my work, and especially about the manuscripts, have always been right to the point. And your mentoring has always been great nourishment for me.

Without these two people, I would have abandoned my PhD during the first week. Octavi and Jordi, thank you for technical support, programming tips, and for answering my silly questions.

On the other hand, without my fellow CTTC friends, I would have definitely finished this thesis much faster. But anyway I would like to thank them for the fun and happy moments. Adel, even though fate has put us in separate offices, we still remained friends. Xavi Álvarez, you have both exceptional organizational and liquid sustenance drinking skills. Aleix, our after-lunch coffee misanthropic conversations were an enormous pleasure for me. Eduard, thank you for introducing me to Catalan culture and for the lovely trips to Menorca. Arnau, your presence always brightens my day, even though sometimes you are too much. CTTC is generally full of delightful people. I am happy that I met Kike, Jannes, Guillem, Santiago (a.k.a. Chamo), Nico Valle and Nico Ablanque, Jiang, Eugenio, Carles, Jesus Ruano and Joan Calafell.

I would like to mention Evgeny Burnaev and Vladimir Vanovskiy from the Skoltech University, where I did my research stay. I hope that a long-lasting,

fruitful collaboration will grow out of these three months I spent in your lab.

I also want to express my gratitude to Anastasya Nagornaya and Vladimir Panferov from the HVAC department of the SUSU university in Chelyabinsk. You were my first university professors, and all the love I have for science I got from you.

There is a great deal of debts I owe to my partner Ali for providing me support during these hard but happy years. I am really grateful to you for being there when I needed it the most, giving me advice, and being my best friend. And special thanks for reading all my manuscripts and helping me to write all those tricky emails.

My family has always been my strongest supporter all along this journey. And I want to thank them for their unconditional love and support. But I also want to especially thank my parents, Marina and Sergey, for investing all this time and money into my education, my grandmother Anna for lending me her moral compass, and my brothers Vsevolod and Georgy for their very wise advice and suggestions.

I give my gratitude to Ministerio de Universidades de España for providing me with economic support during these years through their FPU predoctoral scholarship.

And at the end of all, I would like to thank somebody from times long gone - a girl that I once met in the corridor of the university during my first week there. She told me that I could get a higher student allowance if I studied hard. As weird as it sounds, it did motivate me to study hard. Allowance or not allowance, the motivation is still there because of the girl whose name I do not remember.

Abstract

This thesis presents a methodology for computational fluid dynamics (CFD) -based multi-fidelity surrogate models for indoor environmental applications. The main idea of this work is to develop a model that has an accuracy comparable to CFD simulations but considerably lower computational cost and is capable of performing real-time or faster than real-time simulations of indoor environments using ordinary office computers.

This work can be divided into three main parts. In the first part, a rigorous analysis of the feasibility of affordable high-fidelity CFD simulations for indoor environment design and control is carried out. In this chapter, we analyze two representative test cases, which imitate common indoor airflow configurations, on a wide range of different turbulence models and discretizations methods to meet the requirements for the computational cost, run-time, and accuracy. We apply the knowledge on the growth in computational power and advances in numerical algorithms in order to analyze the possibility of performing accurate yet affordable CFD simulations on ordinary office computers. We consider statistically steady-state simulations for indoor environment design and transient simulations for control. Among studied turbulence models, the no-model and large-eddy simulation (LES) with staggered discretizations show the best performance. We conclude that high-fidelity CFD simulations on office computers are too slow to be used as a primary tool for indoor environment design and control. Taking into account different laws of computer growth prediction, we estimate the feasibility of high-fidelity CFD on office computers for these applications for the next decades.

The second part of this thesis is dedicated to developing a surrogate data-driven model for the prediction of comfort-related flow parameters in a ventilated room. This chapter is an answer to the conclusions of the first part of the thesis, where we establish the unfeasibility of accurate and computationally cheap CFD simulations for routine use in building applications. This chapter uses a previously tested ventilated cavity with a heated floor case. The developed surrogate model predicts a set of comfort-related flow parameters, such as the average Nusselt number on the hot wall, jet separation point, average kinetic energy, average enstrophy, and average temperature, which were also comprehensively studied in the previous part of the thesis. The developed surrogate model is based on the gradient boosting regression, chosen due to its accurate performance among four tested machine learning methods. The model inputs are the temperature and velocity values in different locations, which act as a surrogate of the sensor readings. The locations and the number of these sensors were determined by minimizing the prediction error. This model does not require the repetition of CFD simulations in order to be applied since the structure of the input data imitates sensor readings. Furthermore, the low computational cost of model execution and good accuracy makes it an effective alternative to CFD for applications where rapid predictions of complex flow configurations are required, such as model predictive control.

The third part of the thesis is an extension of the surrogate model developed in the second part. In this chapter, we implement a multi-fidelity approach to reduce the computational cost of the training dataset generation. The developed surrogate model is based on Gaussian process regression (GPR), a machine learning approach capable of handling multi-fidelity data. The variable fidelity dataset is constructed using coarse- and fine-grid CFD data with the LES turbulence model. The surrogate model takes the temperature and velocity magnitude values at four different cavity locations determined as optimal in the previous part of the work. We test three multi-fidelity approaches: GPR trained on both high- and low-fidelity data without distinction, GPR with linear correction, and multi-fidelity GPR or co-cringing. The computational cost and accuracy of these approaches are compared with GPRs based only on high- or low-fidelity data. All of the tested multi-fidelity approaches successfully reduce the computational cost of dataset generation compared to high-fidelity GPR while maintaining the required level of accuracy. The co-cringing approach demonstrates the best trade-off between computational cost and accuracy.

Contents

Abstract **v**

Nomenclature **1**

1 Introduction **7**
1.1 Indoor environmental applications 7
1.2 Indoor environmental prediction models 8
1.3 Surrogate models 13
1.4 Objectives of the thesis 16
1.5 Outline of the thesis 18
1.6 Background of the research group 19
1.7 Related publications 20
References 22

2 On the feasibility of affordable high-fidelity CFD simulations for indoor environment design and control **33**
2.1 Introduction 34
2.2 Governing equations and physical problems 36
2.2.1 Governing equations 36
2.2.2 Test case 1: Differentially heated cavity 36
2.2.3 Test case 2: Mixed convection in a ventilated cavity . . 37
2.3 Numerical methods 39
2.3.1 Unsteady Reynolds-averaged Navier-Stokes approach 40
2.3.2 Large-eddy simulation approach 40
2.3.3 No-model approach 41
2.4 Results of the steady-state analysis 41
2.4.1 Test case 1 - differentially heated cavity. Results of the steady simulations 43
2.4.2 Test case 2 - mixed convection. Results of the steady simulations 46
2.5 Results of the transient analysis 47
2.5.1 Test case 1 - differentially heated cavity. Results of the transient simulations 49

2.5.2 Test case 2 - mixed convection. Results of the transient simulations . . . 52
2.6 Summary of the obtained results . . . 54
2.7 Discussion . . . 58
2.7.1 Extrapolation to real-size problems . . . 58
2.7.2 Availability of steady-state simulations for design applications . . . 59
2.7.3 Availability of transient simulations for MPC applications 61
2.8 Conclusions . . . 61
References . . . 62

3 A CFD-based surrogate model for predicting flow parameters in a ventilated room using sensor readings 67
3.1 Introduction . . . 68
3.2 Physical problem and dataset generation . . . 70
3.2.1 Governing equations . . . 70
3.2.2 Physical problem . . . 70
3.2.3 Dataset generation . . . 71
3.2.4 Input and output parameters . . . 72
3.3 Numerical methods . . . 73
3.3.1 CFD simulations . . . 73
3.3.2 Data-driven models . . . 76
3.3.3 Data preprocessing and metrics . . . 78
3.4 Results . . . 78
3.4.1 Comparison of different DDSM approaches . . . 78
3.4.2 Optimal sensor position for the prediction of flow parameters . . . 81
3.5 Discussion . . . 89
3.6 Conclusions . . . 91
References . . . 91

4 Application of multi-fidelity approach for surrogate modeling of indoor airflow parameters in a ventilated room 95
4.1 Introduction . . . 96
4.2 Test case description . . . 98
4.2.1 Governing equations . . . 98

- 4.2.2 Physical problem . . . 99
- 4.3 Dataset generation . . . 100
  - 4.3.1 Description of the dataset . . . 100
  - 4.3.2 Input and output parameters . . . 100
  - 4.3.3 CFD simulations . . . 101
- 4.4 Surrogate models . . . 103
  - 4.4.1 Gaussian process regression for single-fidelity data . . . 103
  - 4.4.2 Gaussian process regression with linear correction . . . 104
  - 4.4.3 Multi-fidelity Gaussian process regression . . . 105
  - 4.4.4 Data preprocessing and metrics . . . 105
- 4.5 Results . . . 106
  - 4.5.1 Single-fidelity models . . . 106
  - 4.5.2 Multi-fidelity models . . . 108
- 4.6 Discussion and conclusions . . . 112
- References . . . 114

5 Concluding remarks 119

A Results from the direct numerical simulation of a turbulent air-filled mixed convection 123

- References . . . 127

List of Figures

1.1 Schematic representation of a multizone model. 10
1.2 Left: schematic representation of a zonal model, grey area shows the cells which require using a jet model. Right: schematic representation of a CFD simulation. 11
1.3 Schematic representation of surrogate modeling principles. . . 14
2.1 Left: geometry of the differentially heated cavity case. Right: geometry of the mixed convection case. 37
2.2 Test case 1. Steady-state analysis. Average Nusselt number (top) and average stratification (bottom) on different grid resolutions and turbulence models against time ratio. Each point in the graph corresponds to a mesh from Table 2.1. "C" stands for collocated grid discretization and "S" - for staggered. 44
2.3 Test case 1. Steady-state analysis. Top: Average kinetic energy on different grid resolutions and turbulence models against time ratio. Bottom: Zoomed image of the graph at the top. Each point in the graph corresponds to a mesh from Table 2.1. "C" stands for collocated grid discretization and "S" - for staggered. 45
2.4 Test case 1. Steady-state analysis. Average enstrophy on different grid resolutions and turbulence models against time ratio. "C" stands for collocated grid discretization and "S" - for staggered. 46
2.5 Test case 2. Steady-state analysis. Average temperature with different grid resolutions and turbulence models against time ratio. Each point in the graph corresponds to a mesh from Table 2.2. "C" stands for collocated grid discretization and "S" - for staggered. 47
2.6 Test case 2. Steady-state analysis. Average kinetic energy (top) and average enstrophy (bottom) with different grid resolutions and turbulence models against time ratio. Each point in the graph corresponds to a mesh from Table 2.2. "C" stands for collocated grid discretization and "S" - for staggered. 48

2.7 Snapshot from a video of the DNS simulations of the mixed convection case (test case 2). The plotted quantity is the velocity magnitude. The full video is available at [54] 49

2.8 Test case 1. Top: Time evolution of the Nusselt number on the hot wall. Bottom: RMSE of the Nusselt number with different grids and turbulence models against time ratio. Each point in the bottom graph corresponds to a mesh from Table 2.1. “C” stands for collocated grid discretization and “S” - for staggered. 50

2.9 Test case 1. Top: Time evolution of the kinetic energy. Bottom: RMSE of the kinetic energy with different grids and turbulence models against time ratio. Each point in the bottom graph corresponds to a mesh from Table 2.1. “C” stands for collocated grid discretization and “S” - for staggered. 51

2.10 Test case 1. Top: Time evolution of the enstrophy. Bottom: RMSE of the enstrophy awith different grids and turbulence models against time ratio. Each point in the bottom graph corresponds to a mesh from Table 2.1. “C” stands for collocated grid discretization and “S” - for staggered. 53

2.11 Test case 2. Top: Time evolution of the average cavity temperature. Bottom: RMSE of the average cavity temperature with different grids and turbulence models against time ratio. Each point in the bottom graph corresponds to a mesh from Table 2.2. ”C” stands for collocated grid discretization and ”S” - for staggered. 54

2.12 Test case 2. Top: Time evolution of the kinetic energy. Bottom: RMSE of the kinetic energy against time ratio. Labeling is the same as in figure 2.11. 55

2.13 Test case 2. Top: Time evolution of the enstrophy. Bottom: RMSE of the enstrophy against time ratio. Labeling is the same as in figure 2.11. 57

2.14 Potential of accessing affordable high-fidelity CFD over the next years. Top: estimation for a generic closed system. Bottom: estimation for a generic open system. The solid line is the memory bandwidth growth rate, and the dashed line is Moore’s law growth rate, the shadowed area between the lines - intermediate possibilities. 60

3.1 Left: geometry of the studied test case. Right: locations of the input data probes at the mid-depth cavity plane ($z = D/2$). . . 71
3.2 Schematic image of the computational grid used in the study. 74
3.3 Mean relative error (MRE) of the studied flow parameters for different number of samples in the training dataset and different ML models. Top left: Nusselt number on the hot wall, $<Nu>$. Top right: average kinetic energy, $<E>$. Middle left: average enstrophy, $<\Omega>$. Middle right: average cavity temperature, $<T_V>$. Bottom: flow separation point, x_{sep}. 80
3.4 Studied combinations of temperature and velocity sensor locations. Thick black lines represent the possible positions of the probes. 82
3.5 Mean relative error of the averaged Nusselt number $MRE(<Nu>)$ for different sensor positions. Top left - sensors at the ceiling and the left wall (configuration 1 in Figure 3.4). Top right - sensors at the ceiling and the right wall (configuration 2 in Figure 3.4). Bottom - sensors at the left and right wall (configuration 3 in Figure 3.4), where the right wall is assigned to the x axis. 83
3.6 Mean relative error of the averaged kinetic energy $MRE(<E>)$for different sensor positions. Top left - sensors at the ceiling and the left wall (configuration 1 in Figure 3.4). Top right - sensors at the ceiling and the right wall (configuration 2 in Figure 3.4). Bottom - sensors at the left and right wall (configuration 3 in Figure 3.4), where the right wall is assigned to the x axis. 84
3.7 Mean relative error of the averaged enstrophy $MRE(<\Omega>)$ for different sensor positions. Top left - sensors at the ceiling and the left wall (configuration 1 in Figure 3.4). Top right - sensors at the ceiling and the right wall (configuration 2 in Figure 3.4). Bottom - sensors at the left and right wall (configuration 3 in Figure 3.4), where the right wall is assigned to the x axis. . . . 85

3.8 Mean relative error of the averaged cavity temperature $MRE(< T_V >)$ for different sensor positions. Top left - sensors at the ceiling and the left wall (configuration 1 in Figure 3.4). Top right - sensors at the ceiling and the right wall (configuration 2 in Figure 3.4). Bottom - sensors at the left and right wall (configuration 3 in Figure 3.4), where the right wall is assigned to the x axis. 86

3.9 Mean relative error of the flow separation point $MRE(x_{sep})$ for different sensor positions. Top left - sensors at the ceiling and the left wall (configuration 1 in Figure 3.4). Top right - sensors at the ceiling and the right wall (configuration 2 in Figure 3.4). Bottom - sensors at the left and right wall (configuration 3 in Figure 3.4), where the right wall is assigned to the x axis. . . . 87

3.10 Maximum (among studied flow parameters) mean relative error for different sensor positions. Top left - sensors at the ceiling and the left wall (configuration 1 in Figure 3.4). Top right - sensors at the ceiling and the right wall (configuration 2 in Figure 3.4). Bottom - sensors at the left and right wall (configuration 3 in Figure 3.4), where the right wall is assigned to the x axis. . . . 88

3.11 Locations of temperature and velocity sensors with the highest prediction accuracy. The thick blue lines show the best sensor positions. 89

4.1 Left: geometry of the studied test case. Right: locations of the input data probes at the mid-depth cavity plane ($z = D/2$). . . 99

4.2 Schematic image of the computational grid used in the study. 102

4.3 Mean relative error (MRE) of the studied flow parameters for different number of samples in the training dataset and different single-fidelity models. Top left: Nusselt number on the hot wall, $< Nu >$. Top right: average kinetic energy, $< E >$. Middle left: average enstrophy, $< \Omega >$. Middle right: average cavity temperature, $< T_V >$. Bottom: flow separation point, x_{sep}. . . . 107

4.4 HFLF GPR model. Left: Mean relative error (MRE) of the average enstrophy $< \Omega >$ for a different total number of training samples and different percentage of high-fidelity (HF) samples. Right: Computational cost of dataset generation for accurate predictions (< 0.1) using different percentages of HF samples. 109

4.5 LC GPR model. Left: Mean relative error (MRE) of the average enstrophy $< \Omega >$ for different total number of training samples and different percentage of high-fidelity (HF) samples. Right: Computational cost of dataset generation for accurate predictions (< 0.1) using different percentage of HF samples. . 110
4.6 MF GPR model. Left: Mean relative error (MRE) of the average enstrophy $< \Omega >$ for different total number of training samples and different percentage of high-fidelity (HF) samples. Right: Computational cost of dataset generation for accurate predictions (< 0.1) using different percentage of HF samples. . 110
4.7 Left: Mean relative error (MRE) of the average enstrophy $< \Omega >$ for different number of high-fidelity (HF) training samples using different surrogate models. Right: Computational cost of dataset generation for accurate predictions (< 0.1) using different number HF samples with different surrogate models. 111
A.1 Mean horizontal velocity in the median plan ($z = 0.15$). Left: at the cavity mid-height ($y = 0.50$). Right: at the cavity mid-width ($x = 0.50$). 123
A.2 Mean vertical velocity in the median plan ($z = 0.15$). Left: at the cavity mid-height ($y = 0.50$). Right: at the cavity mid-width ($x = 0.50$). 124
A.3 Mean temperature in the median plan ($z = 0.15$). Left: at the cavity mid-height ($y = 0.50$). Right: at the cavity mid-width ($x = 0.50$). 125
A.4 Instantaneous (left) and averaged (right) temperature fields in the median plan ($z = 0.15$). 125
A.5 Instantaneous (left) and averaged (right) horizontal velocity fields in the median plan ($z = 0.15$). 126
A.6 Instantaneous (left) and averaged (right) vertical velocity fields in the median plan ($z = 0.15$). 126

List of Tables

2.1 Computational grids used in the simulations of the differentially heated cavity case (test case 1). 38
2.2 Computational grids used in the simulations of the mixed convection case (test case 2). 39
2.3 Computational time ratios R, obtained for the differentially heated cavity (test case 1) and the mixed convection (test case 2) for several indoor environmental applications and different turbulence models. ″C″ stands for collocated grid discretization and ″S″ - for staggered. The shadows of blue from light to dark show computational time ratios from low to high, respectively. The red cross stands for the insufficient accuracy. 56
3.1 Combinations of the test case configurations for generating the CFD dataset. “CG” stands for coarse-grid “FG” for fine-grid CFD simulations. Each combination for A_w and Ra_H is tested for all of the 20 Fr numbers listed in the table. 72
3.2 Summary of the tested machine learning approaches and their hyperparameters. 76
3.3 Mean relative prediction error (MRE) of the studied flow parameters for different models on the test dataset. 79
4.1 Combinations of the test case configurations for generating the CFD dataset. “LF” stands for low-fidelity (coarse-grid) “HF” for high-fidelity (fine-grid) CFD simulations. Each combination for A_w and Ra_H is tested for all of the 20 Fr numbers listed in the table. 100
4.2 Mean MRE error (see Table 4.3 for details), computational cost and number of low- and high-fidelity dataset samples of the studied models with the best trade-off between computational cost and accuracy. 112
4.3 Mean relative prediction error (MRE) of the studied flow parameters for different models on the test data using training dataset configurations summarized in Table 4.2. 113

Nomenclature

Acronyms

ANN	Artificial neural network
CFD	Computational fuid dynamics
DDM	Data-driven model
DDSM	Data-driven surrogate model
DNS	Direct numerical simulation
FFD	Fast fluid dynamics
GBR	Gradient boosting regression
GP	Gaussian process
GPR	Gaussian process regression
HF	High-fidelity
HVAC	Heating ventilation and air conditioning
LBM	Lattice Boltzmann method
LCGPR	Gaussian process regression with linear correction
LES	Large-eddy simulation
LF	Low-fidelity
LOO	Leave-one-out
MFGPR	Multi-fidelity Gaussian process regression
ML	Machine learning
MPC	Model predictive control
MRE	Mean relative error
POD	Proper othognal decomposition
RANS	Reynolds average Navier-Stokes
RB	Radial-basis
ReLU	Rectified linear unit
RE	Relative error
RMSE	Root mean square error
SVR	Support vector regression
URANS	Unsteady Reynolds average Navier-Stokes

Dimensionless numbers

Fr	Froude number based on the ratio between the bulk inlet and buoyant velocity
$Fr_{h_{in}}$	Froude number based on the inlet height
Nu	Nusselt number on the hot wall
Pr	Prandtl number
Ra_H	Rayleigh number based on the cavity height
Re_H	Reynolds number n the cavity height
$Re_{h_{in}}$	Reynolds number based on the inlet height
Re_τ	friction Reynolds number

Latin symbols

A	surface area
A_d	depth aspect ratio
A_h	height aspect ratio
A_{in}	inlet slot aspect ratio
A_{out}	outlet slot aspect ratio
A_w	width aspect ratio
C_r	coefficient of the refinement
c	arbitrary constant
D	depth
DS	data sample
DS_h	high-fidelity data sample
DS_l	low-fidelity data sample
$d(\cdot,\cdot')$	Euclidean distance
E	kinetic energy
$\mathbf{g}$	gravitational acceleration
H	height
h_{in}	inlet height
h_{out}	outlet height
$K_{\nu_k}(\cdot)$	modified Bessel function
$k(\cdot,\cdot')$	covariance function

l	kernel length scale
$M(\mathbf{X}^d, \mathbf{y}^d)$	surrogate model
N	number of samples in the dataset
N_{bulk}	number of the vertical grid points in the bulk area
N_{in}	number of the vertical grid points in the inlet area
N_{out}	number of the vertical grid points in the outlet area
N_{total}	total number of grid points
N_x	number of grid points in the horizontal direction
N_y	number of grid points in the vertical direction
N_z	number of grid points in the spanwise direction
p	kinematic pressure
R	simulation time ratio
S	stratification
T	temperature
T_c	temperature on the cold wall
T_h	temperature on the hot wall
T_V	average cavity temperature
t	time
t_{end}	end of the time integration period
t_{ini}	beginning of the time integration period
t_{phy}	physically simulated time
t_{ref}	reference time
t_{sim}	computational time
U	velocity magnitude
U_{buo}	buoyant velocity
U_{in}	bulk inlet velocity
U_{ref}	reference velocity
$\mathbf{u}$	velocity vector
u	horizontal (x) component of the velocity vector
V	volume of the cavity
v	vertical (y) component of the velocity vector
W	width
w	spanwise (z) component of the velocity vector
$\mathbf{X}^d$	input data sample
$\mathbf{X}_h^d$	high-fidelity input data sample
$\mathbf{X}_l^d$	low-fidelity input data sample

$\mathbf{x}$	Cartesian coordinates vector
x	horizontal coordinate
x_{sep}	jet separation point
y	vertical coordinate
$\mathbf{y}^d$	output data sample
$\hat{\mathbf{y}}^d$	output of the multi-fidelity surrogate model
$\tilde{\mathbf{y}}^d$	output of the single-fidelity surrogate model
$\mathbf{y}_h^d$	high-fidelity output data sample
$\mathbf{y}_l^d$	low-fidelity output data sample
z	spanwise coordinate

Greek symbols

α	thermal diffusivity
β	thermal expansion coefficient
$\Gamma(\cdot)$	gamma function
γ_x	grid concentration factor in the horizontal direction
γ_x	grid concentration factor in the vertical direction
ΔT	temperature difference
Δx_{max}	maximum grid size in the horizontal direction
Δy_{max}	maximum grid size in the vertical direction
Δx_{min}	minimum grid size in the horizontal direction
Δy_{min}	minimum grid size in the vertical direction
$\Delta \mathbf{y}^d$	test set error of the surrogate model
Δz	grid size in the spanwise direction
$\delta(\cdot\hat{a}\cdot')$	Kronecker delta
ϵ	Gaussian white noise
$\eta_{Grö}$	Grötzbach estimate
ν	kinematic viscosity
ν_k	kernel smoothness
ρ	density
σ^2	variance
τ_W	wall-shear stress
ϕ	arbitrary variable
ϕ_{CFD}	arbitrary variable obtained via CFD simulation

ϕ_{SM}	arbitrary variable obtained via surrogate model
ϕ_{DNS}	arbitrary variable obtained via DNS CFD simulation
Ω	enstrophy
$\boldsymbol{\omega}$	vorticity

Brackets

$<>$	time-averaged values

1

Introduction

This thesis aims to develop fast and robust surrogate models for simulations of an indoor environment combining computational fluid dynamics (CFD) and machine learning (ML) techniques. This chapter presents an introduction to indoor environmental simulations and their state-of-the-art techniques. The chapter includes an extensive literature review on different approaches to indoor environmental modeling, discussing their advantages and disadvantages. The scope, objectives, and the outline of the thesis are presented at the end of this chapter.

1.1 Indoor environmental applications

Energy consumption in buildings is a significant aspect of the global energy-saving strategy. Nowadays, most heating ventilation and air conditioning (HVAC) systems are mechanical. They consume a significant amount of energy and account for approximately 40% of total primary energy consumption in developed countries [1]. Energy consumption in buildings can be decreased by various means, among them the proper design and precise control of indoor air parameters, which require knowledge of indoor air dynamics. However, indoor air dynamics is usually a nonlinear, transient process, which depends on many factors such as weather, building geometry, occupants' behavior, etc. Thus, indoor air dynamics usually involve various complex physical phenomena, such as stratification, natural and forced convection. As a result, the task of precise prediction of indoor air parameters is not straightforward.

Precise prediction of indoor air parameters is used to design effective ventilation setups. The design of HVAC systems is usually divided into two stages: early conceptual design and final detailed design. In the former, highly accurate simulations are not required. At this stage of a project, only conceptual decisions are made. More important for conceptual design is the speed of the calculations, which allows to test different design decisions. On the other hand, final stage design applications require accurate and detailed simulation results. A building project, in many cases, demands several representative daily simulations [2], which imposes constraints on the maximum computational cost. In many cases, simulations for indoor environmental design should be faster than real-time in order to be feasible for practical use. For example, a reasonable computational speed for a daily simulation should be at least twice faster than real-time since it would allow an engineer to start a 24 hours physical time simulation at the end of the working day and obtain the results the following day (in 12 hours approximately).

Another important application is indoor environment control. Many control methods have been developed or proposed for HVAC systems. However, because of their simplicity, simple on/off and proportional integral derivative control are still used in many HVAC systems, resulting in inconsistent performance and inadequate thermal comfort. With advances in data storage, computing, and communication devices, it is now feasible to adopt and implement a more precise control approach, such as model predictive control (MPC). MPC elaborates a model of the system evolution and executes control actions based on it [3]. Typically, building airflow MPC systems have a control horizon range of 4-5 hours with a time step of 1-3 hours [4], which is a relatively short period in the building dynamics scale. Transient simulations are necessary to develop high-quality MPC models since they help capture the system dynamics; moreover, the nature of MPC requires these simulations to be faster than real-time.

1.2 Indoor environmental prediction models

There are several common ways to evaluate air distribution in buildings, namely, analytical and empirical models, experimental measurements, and computer simulations. Analytical models are derived from fundamental equations of fluid dynamics and heat transfer; they simplify geometry and boundary conditions to obtain a solution. As a result, the final equations obtained for one case may not be used for another without modifications. The empirical models are developed from the conservation equations of mass, energy, and chemical species, similar to the analytical models. In many cases, experimental measurements or computer simulations are used to develop empirical models. In theory, the analytical and empirical models do not differ very much. The perception is that the empirical models may use more approximations than the analytical models. As a result, the complexity of indoor airflow and unique features of each building make the usage of analytical or empirical models very difficult [5]. The experimental models are based on either full- or small-scale experiments. Despite their high accuracy, they experience major scaling and generalization issues and are considered too expensive for studying ventilation performance in buildings. Nowadays, experimental models are mainly used for validation. As a result, computer simulations are considered the primary tool for evaluating indoor air dynamics since they allow a high degree of flexibility with smaller efforts.

Computer simulations of indoor environments are typically conducted using multizone (airflow network) models, zonal models, and CFD. Multizone models have the lowest computational cost and the lowest accuracy, while CFD simulations provide detailed information about indoor airflow at the cost of high computational effort. Airflow network models are one-dimensional models. They represent a building as a set of zones (rooms) connected by the airflow paths with resistances. The air parameters are uniform inside each zone. A schematic represenation of a multizone model is shown in Figure 1.1. These models are based on the Bernoulli equation, so the momentum effect is neglected [6]. Considering that each node represents a single room, its airflow distribution cannot be determined. Because of their simplicity, these models have severe limitations that produce significant errors in the results. Axley [7] provides a complete review of existing multizone models and their theoretical background. The multizone models are mainly used to predict air exchange rates [8], thermal loads [9], ventilation efficiency [10], and contaminant transport in buildings [11]. Despite their severe limitations, multizone models seem to be the only tool to obtain meaningful results for predicting ventilation performance in an entire building.

The well-mixing assumption used in the multizone models is not valid for large indoor spaces or rooms with stratified ventilation systems. Therefore, zonal models have been used to remedy the problem in predicting air

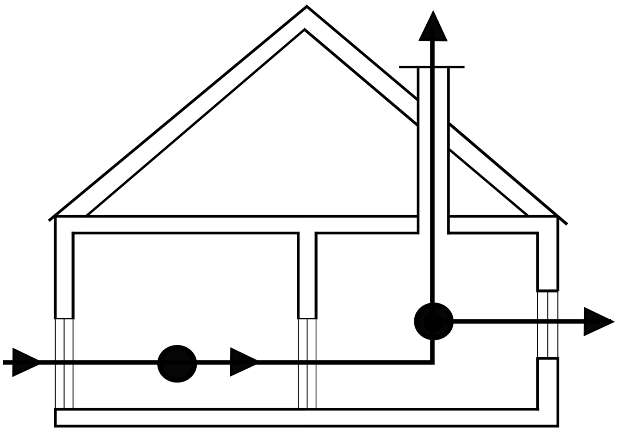

Figure 1.1: Schematic representation of a multizone model.

temperature distributions. Zonal models divide a room into a small number of cells (usually less than 1000 per room) and solve mass and energy balance equations in each cell. A schematic represenation of a room with zonal model is shown in Figure 1.2 (left). To reduce the computational cost, zonal models discard the momentum equation. When the flow momentum is strong, model accuracy may considerably drop [12]. To improve simulation accuracy, regions with strong flow momentum are treated separately using empirical jet models [13]. It significantly increases case dependency computational cost and decreases the stability of zonal models. A review of existing zonal models can be found in [14]. By comparing with very coarse-grid CFD simulations, the zonal models do not show much superiority in reducing computing time. In many cases, the overhead time in preparing data input for a zonal model may be longer than that for a CFD simulation [5], which makes them impractical.

In CFD simulations (Figure 1.2, right), Navier-Stokes equations are solved numerically on a finite number of control volumes, which divide the case domain. The solution provides a complete set of air parameters for each control volume. One of the primary CFD challenges is turbulence modeling [15]. The effect of turbulence can be resolved using a direct numerical simulation (DNS) or modeled using large-eddy simulation (LES) and Reynolds average Navier-Stokes (RANS) approaches. DNS is the most accurate and the most computationally expensive method because it resolves all the turbulent flow scales, which require very fine grids. LES models resolve only large scales of motion and model the small ones, while RANS solves the mean flow and models its turbulent fluctuations. LES models are computationally more expensive than RANS, but both methods successfully reduce computational cost compared to DNS. However, CFD still has a vast data processing cost in comparison with the above-explained multizone and zonal models.

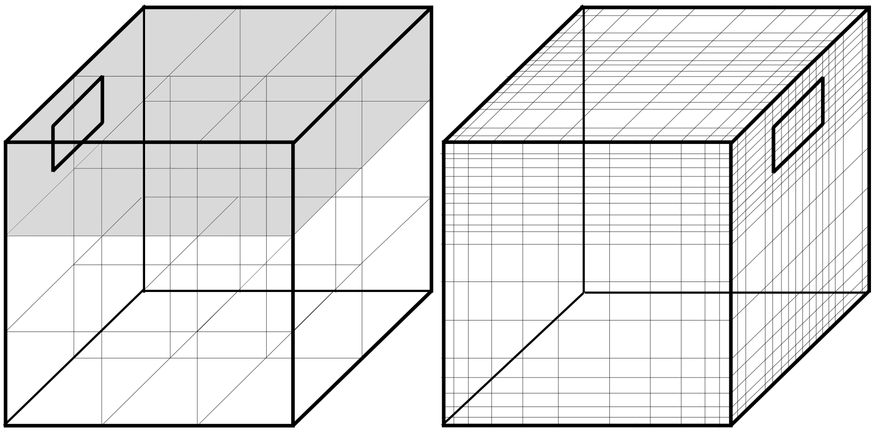

Figure 1.2: Left: schematic representation of a zonal model, grey area shows the cells which require using a jet model. Right: schematic representation of a CFD simulation.

CFD has been successfully used for detailed simulations of building airflows by many researchers [16–20]. Nevertheless, all of these studies show the need for a compromise between computational cost and accuracy. Van Hooff *et al.* [16] performed CFD simulations of a generic isolated building. They used a computational grid of 5×10^6 control volumes to achieve reliable results, which required using 14 CPU cores on a high-performance computer. Other studies also indicate the high computational cost of CFD. For example, Chen *et al.* [18] showed that an accurate simulation of a kitchen room would require at least 10^6 control volumes. Chen *et al.* [17] used a grid of 4×10^6 control volumes for an accurate simulation of an office room with a ceiling fan. Zheng *et al.* [20] studied the wind flow for buildings with balconies using a fine mesh of 2×10^7 cells. An ordinary office computer does not have sufficient memory and CPU power to complete such large simulations in a reasonable amount of time for indoor environment design and control. Moreover, the widely used RANS turbulence models do not always produce satisfactory results, making the use of more accurate (and more expensive) turbulence models indispensable [16, 20]. Accurate CFD simulations require large computational resources, while using ordinary office computers can result in unreasonably long run-times. Grid coarsening and RANS turbulence modeling are common ways to reduce the cost of CFD, but they can lead to overly inaccurate results. Therefore, the task of performing affordable yet accurate CFD is not straightforward.

Over the last decade, several attempts to reduce the computational cost of CFD for indoor environmental applications have been made. Wang & Zhai [21] examined the credibility of coarse-grid CFD for HVAC applications and optimized the space discretization to reduce the total truncation error. Kempe & Hantsch [22] applied the immersed boundary method to an LES simulation of a room with a heat source and achieved real-time LES simulations with 32 CPU cores. Zhang & Mirzaei [23] improved the results of coarse-grid CFD by mapping into them the results of fine-grid CFD simulations and then coupled these CFD simulations with building energy simulations achieving a computational speed about 200 times faster than ordinary coupling methods. Chen *et al.* [24] applied polyhedral meshes for the CFD simulations of indoor environment and reported saving almost 95% of computing time without sacrificing model accuracy, compared with the use of tetrahedral and hexahedral meshes. However, all of the aforementioned studies focus only on the specific aspects of computational cost reduction; thus, their methods have limited applicability. Moreover, they did not study the transient flows and did not consider different turbulence models.

Apart from classical CFD methods, two other similar approaches are used nowadays. Those are the lattice Boltzmann method (LBM) and fast fluid dynamics (FFD). LBM method [25–27] uses the discretized Boltzmann equation with density-momentum and internal energy distribution functions to calculate the flow [28]. The LBM deals with microscopic particle collision and streaming to construct the macroscopic quantities. Since the advection term limits the time step, LBM is shown to be slower than CFD simulations with similar grid resolutions [26] and has not gained much popularity in the field of indoor environmental simulations. However, the LBM method is still used in the simulations of indoor environments, which focus on particle tracking. For example, simulations of pollutant dispersion [29] or emission behaviors of organic compounds [30].

FFD was first introduced by Stam [31] for computer games. Zuo & Chen [32] adapted the numerical algorithm for airflow in buildings and introduced turbulence modeling. The FFD method uses a first-order semi-Lagrangian scheme to solve the advection term, computes the diffusion term implicitly, decouples pressure and velocity with fractional step method [33]. The implicit scheme allows an increased time step, besides computational speed is additionally enhanced by using low order discretization schemes. As a result, FFD has lower computing costs but also lower accuracy than the classic CFD [32]. FFD was claimed to be capable of faster than the real-time simulations, but due to the low accuracy of the predictions, it was recognized as a valid alternative to CFD. Nevertheless, FFD found its niche in the urban flow simulations because classical CFD models are unable to meet the demand for fast simulations with meter-level spatial resolution and minute-level temporal resolution due to the huge computational domain with numerous grids for urban residential areas [34, 35].

All the aforementioned methods are primarily used in indoor environment design. On the other hand, for MPC, usually, low order models such as multizone are used [36, 37]. So far, CFD has not been integrated into MPC directly due to the enormous computational cost and nonlinearity of the governing equations. However, several preliminary attempts have been made to simplify CFD to fit MPC requirements [38, 39].

1.3 Surrogate models

Surrogate models are models that approximate the behavior of complex systems, based on a limited set of computationally expensive simulations. Surrogate models mimic the complex behavior of the underlying simulation models as closely as possible while being considerably computationally cheaper to evaluate. Figure 1.3 shows the schematic representation of surrogate modeling principles. Surrogate models are constructed using a data-driven, bottom-up approach. Data-driven models (DDM) are based on using data analysis to find relations between system state variables without explicit knowledge of the physical behavior of the system. Essentially, they represent a shift from “knowledge-based” to “knowledge-learned” modeling. DDMs are classified as either statistical or ML-based models, depending on factors such as their origin, governing philosophy, and the typical size of the data sets analyzed. DDMs can be developed comparatively easily since they do not require an understanding of system physics. In order to train these models, a comprehensive set of input-output data of the system is needed under all possible working conditions. Thus, the ease of development of surrogate models comes at the cost of reduced generalization capability compared to the classical modeling approaches. The accuracy of DDMs decreases when training data deviates from testing data. Hence, it is critical to train these models with the data covering all the possible scenarios, which could be challenging, especially for indoor environmental applications that operate under a wide range of weather conditions throughout the year. However, difficulties in obtaining high-fidelity training data are compensated by the high accuracy and the low computational cost of the resulting models [40].

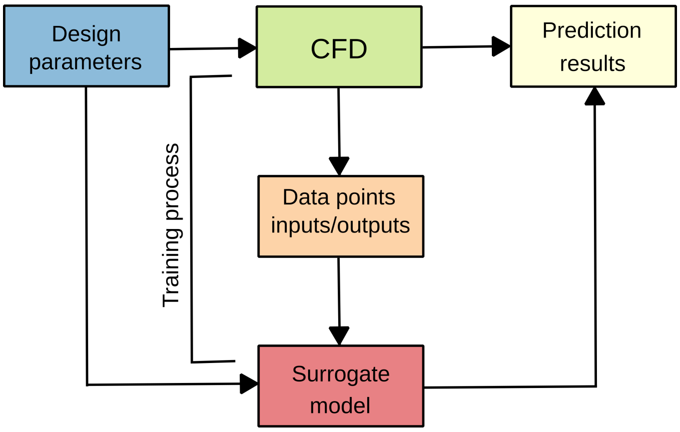

Figure 1.3: Schematic representation of surrogate modeling principles.

Statistical DDMs are usually based on proper orthogonal decomposition (POD). The POD method essentially provides an orthogonal basis for representing a given set of data in a certain least-squares optimal sense, *i.e.*, it offers ways to find optimal lower-dimensional approximations for the given data set. Modeling framework employing POD has been extensively employed for rapid prediction of indoor environmental parameters for different applications, like data centers [41,42] or airplane cabins [43]. Wang *et al.* [44] used a CFD-based POD model to optimize air supply schemes in indoor environments. The results from these studies indicate that POD-based models have good interpolative accuracy but quite poor extrapolative accuracy and are therefore impractical for predictions beyond the input parameter space [45]. However, according to [46], the POD method is successfully used as preprocessing dimensionality reduction step in ML-based DDMs.

Machine learning-based data-driven models are also regularly used to model indoor environments. ML-based models are used as surrogate models for building design, sensitivity and uncertainty analysis, thermal load predictions, and MPC [47]. For instance, DDM-MPC for HVAC systems were developed for a university building [48], an airport [49], and a residential building [40, 50]. DDM based MPC are used to minimize energy consumption [51], maintain thermal comfort at acceptable level [52], and minimize thermal discomfort hours [53]. Moreover, DDMs are widely used for HVAC load predictions. For example, DDMs for thermal load predictions were developed for a single building [54] and a non-residential district [55]. Besides, Park & Park [56] performed a comparative analysis on the predictability of natural ventilation rates. All of the aforementioned works show low computational cost and sufficient accuracy. However, these models primarily rely on other reduced-order models, experimental results, or historical data to generate the input-output data for their DDMs.

Surrogate modeling is often built from and compared with CFD simulations, which allows producing comparable to CFD results in terms of accuracy. Because of its inexpensiveness, surrogate modeling is the major focus of the current research of built environment applications. For example, Athavale *et al.* [42], and Fang *et al.* [57] compared different CFD-based ML-based DDM approaches for temperature prediction in data centers and concluded that results produced by these models are in good agreement with the reference CFD data. Warey *et al.* [58] created an accurate model of vehicle cabin thermal comfort prediction using ML algorithms and high-fidelity CFD simulation results. The models mentioned above are of practical significance. Nevertheless, they are developed for specific applications and cannot directly predict flow parameters in a more generic indoor environment. Zhang *et al.* [59] used DDMs in general indoor environments with CFD as training data to solve the inverse design problem and identify a possible relationship between thermal comfort and inlet boundary condition. On the other hand, Tian *et al.* [60]

used ML based on CFD and experimental data to model indoor environment indicators in the stratified environments in order to evaluate human thermal comfort. Ding *et al.* [60] developed data-driven regression model for coupled indoor-outdoor flow analysis together with CFD simulations. The researchers mentioned above note that CFD-based surrogate models produce accurate predictions at a low computational cost and could be a low-cost alternative to classical modeling techniques.

Using CFD simulations for surrogate modeling usually results in the high computational cost of dataset generation; thus, the increasing number of works is trying to optimize the computational cost of CFD database by using a data-driven multi-fidelity approach, which combines a large number of computationally cheap low-fidelity simulations and a smaller number of expensive high-fidelity simulations, in order to find a trade-off between simulation cost and surrogate model accuracy. Multi-fidelity is a new approach in surrogate modeling, and not many works have been published on this topic. For instance, Lamberti & Gorlé [61] combined RANS and LES simulations in order to create a ML-based model which predicts wind loads on buildings. They showed that the proposed multi-fidelity framework has the potential to significantly reduce the number of expensive LES simulations while retaining a significantly higher accuracy than standard empirical models. The multi-fidelity kriging technique was used by Li *et al.* [62] for the optimization of high-speed train cabin ventilation system design, which led to significant savings of computational time. Zhang *et al.* [63] combined high-fidelity models using a CFD evaluation with fine grid and the low-fidelity models using the same CFD model with a coarse grid to optimize the aerodynamic shape optimization of a RAE2822 airfoil, which improved optimization efficiency and outperformed the single-fidelity method. However, to the best of the author's knowledge, multi-fidelity surrogate modeling has not yet been applied to simulations of the indoor environment.

1.4 Objectives of the thesis

Traditional reduced-order modeling approaches like multizone and zonal models are extensively used in building simulations due to their low computational, even though they offer minimal information about indoor airflows.

On the other hand, CFD represents a certainly more economical solution than physical experiments. However, as later shown in Chapter 2, CFD is still not feasible for routine use in indoor environmental design and control. Because CFD simulations are either not to be trusted entirely due to the insufficient grid resolutions and wrong turbulence models choice or are too computationally expensive to run. Besides, the problem with CFD simulations in a built environment is that, even with a small indoor domain, the airflow is quite complex, making simulations, especially demanding in the design process with a number of scenarios. Moreover, the different attempts to reduce the computational cost of CFD have not resulted in models with acceptable accuracy. From this perspective, surrogate modeling looks like an attractive option due to its low computational cost and comparable with CFD accuracy.

Eventually, surrogate modeling is a valuable technique whose main advantage resides in the possibility to obtain fast and inexpensive predictions, otherwise unfeasible with more expensive CFD simulations. It also comes with limitations such as being case dependent and needing extensive training data sets. However, the ability of surrogate models to imitate the accuracy of CFD simulations makes them especially useful for applications where a rapid prediction of a complex flow phenomenon is required, and traditional reduced-order models cannot be relied on, while CFD simulations turn out to be prohibitively expensive. Moreover, the multi-fidelity approach can help to reduce the computational cost of CFD database generation and improve the model's generalization by increasing the size of the training dataset. On the other hand, case dependence is less significant for indoor environmental applications requiring standard room geometries.

This work aims to show how surrogate modeling can fill a gap between multizone models and CFD, resulting in models which provide more information about indoor airflow than multizone models and demanding considerably less than CFD computational resources. The developed surrogate model acts as a proof of concept. The problem of case dependency is reduced by considering two representative cases of the indoor environment, namely, a tall differentially-heated cavity and a ventilated cavity with a heated floor. These are the classical benchmark test cases used by many researchers in the field of indoor environmental simulations [64–68] for testing novel simulation methods. We have chosen these test configurations because of the challenges they present and because of the availability of both experimental [69,70] and

DNS CFD [71,72] data for validation. The multi-fidelity approach is used to overcome another bottleneck of the surrogate modeling by reducing the computational cost of dataset generation and further increasing the developed model's prediction capabilities.

We believe this thesis significantly contributes to developing surrogate models for fast predictions of indoor environmental parameters. It also helps to better understand different numerical aspects of these models and their effect on the accuracy and computational cost of the resulting models. Moreover, we demonstrate the capability of the proposed methods to prove almost instantaneous predictions of the indoor environmental parameters on an office computer.

1.5 Outline of the thesis

This thesis is organized into five chapters. The first chapter provides an introduction and an extensive literature review on indoor environmental modeling techniques. The main contributions of this research work are presented in three main chapters (chapters 2-4). These chapters are selfâcontained and could be read on their own, without the need to read the complete document. Each chapter contains a short introduction that aims to highlight the contribution of the chapter and put it in the proper context by reviewing related works in the literature. The content of each main chapter is published as original research articles in international journals and presented in different scientific conferences. The last chapter provides concluding remarks and possible future works.

Chapters 2 to 4 present the main contributions of this thesis. Chapter 2 studies the feasibility of affordable high-fidelity CFD for indoor environmental applications using the aforementioned test cases of a tall differentially-heated cavity and a ventilated cavity with a heated floor. Both cases are tested on a wide range of staggered and collocated grids with different LES, RANS, and DNS approaches. Performed CFD simulations are analyzed in terms of computational cost and accuracy to meet the indoor environmental applications requirements. Moreover, the estimation of the feasibility of high-fidelity CFD on office computers for these applications for the next decades is performed using different laws of computer growth prediction. The chapter provides a comprehensive analysis of the capabilities and limitations of CFD for simulations of the indoor environment, taking into account the growth in computational power and advances in numerical algorithms.

Chapter 3 focuses on developing a data-driven surrogate model, which is based on the data from CFD simulations. The model predicts comfort-related airflow parameters in the aforementioned test case of a ventilated room with a heated floor. The main focus of this chapter is on investigating the capabilities and limitations of surrogate modeling as a fast and robust alternative to CFD, taking into account specific requirements for indoor environmental applications. First, different ML methods are tested in order to choose the approach that best fits the developed model specifics. After selecting the appropriate ML method, the surrogate model is optimized to accommodate the requirements of indoor environment design and control applications. The optimization consists of two steps. First, the structure of the input data is changed so that it takes the values of temperature and velocity in the locations, which in a practical case could be replaced by sensor readings. Then different combinations of input probe positions are tested in order to find the optimal sensor placement.

Chapter 4 presents the improvements of the model, developed in Chapter 3 by adopting a multi-fidelity approach combining a small number of high-fidelity simulations with a large number of low-fidelity simulations. LES simulations used in the previous chapter act as high-fidelity data, while low-fidelity data is obtained using coarse-grid LES simulations. The developed model is based on multi-fidelity Gaussian process regression. The model is analyzed in terms of computational cost and accuracy in order to find a trade-off between the number of simulations and their fidelity.

Chapter 5 summarizes and concludes the thesis and contains suggestions for future works.

1.6 Background of the research group

This work was conducted in the Heat and Mass Transfer Technological Center (CTTC) at the Universitat Politècnica de Catalunya. CTTC was created in the 1990s, with a research focus on mathematical modeling and numerical solution of fluid dynamics and heat transfer phenomena, complemented with experimental research for their validation. The main objective of the research work at CTTC is to develop efficient fluid and thermal systems and equipment. In the early 2000s, the simulation tools developed within the group were joined and generalized to create two CFD software packages, namely TermoFluids [73] and STG [74]. TermoFluids is a robust general-purpose software for fluid and heat transfer problems, using state-of-the-art methods for turbulent flows [75,76] and complex thermal systems [77,78], with high computational efficiency and parallel scalability [79]. On the other hand, STG is a fast and highly-scalable [80] in-house code for numerical simulations of three-dimensional problems with one periodic direction [81,82], mainly used in the turbulence modelling [83,84] and regularization techniques [85,86] research. The numerical simulations presented in this thesis were carried out using both TermoFluids and STG software, as well as open-source CFD software - OpenFOAM [87].

1.7 Related publications

The material of this thesis have appeared in the following publications:

- **N. Morozova**, F.X. Trias, R. Capdevila, E. Schillaci and A. Oliva. A CFD-based surrogate model for predicting flow parameters in a ventilated room using sensor readings. *Energy and Buildings* **266**:112146, 2022.

- **N. Morozova**, F.X. Trias, V. Vanovskiy, C. Oliet and E. Burnaev. A CFD-based multi-fidelity surrogate model for prediction of flow parameters in a ventilated room. *In Proceedings of 8th European Congress on Computational Methods in Applied Sciences and Engineering*, June 5-9, 2022, Oslo, Norway.

- E. Schillaci, J. Vera, **N. Morozova** and J. Rigola. A numerical set-up for the simulation of infection probability from SARS-CoV-2 in public transport vehicles. *In Proceedings of 8th European Congress on Computational Methods in Applied Sciences and Engineering*, June 5-9, 2022, Oslo, Norway.

- **N. Morozova**, F.X. Trias, R. Capdevila and A. Oliva. Data-driven prediction of flow parameters in a ventilated cavity using high-fidelity CFD simulations. *In Building Simulation Conference Proceedings*, Sept. 1-3, 2021, Bruges, Belgium.

- **N. Morozova**, F.X. Trias, R. Capdevila and A. Oliva. Investigating the capabilities of CFD-based data-driven models for indoor environmental design and control. *In Proceedings of 7th European Congress on Computational Methods in Applied Sciences and Engineering*, Jan. 11-15, 2021, Virtual Congress.
- **N. Morozova**, F.X. Trias, R. Capdevila, C. D. Pérez-Segarra and A. Oliva. On the feasibility of affordable high-fidelity CFD simulations for indoor environment design and control. *Building and Environment*, **184**:107144, 2020.
- **N. Morozova**, R. Capdevila, F.X. Trias, and A. Oliva. On the feasibility of CFD for transient airflow simulations in buildings. *In Building Simulation Conference Proceedings*, Sept 2-4, 2019, Rome, Italy.
- **N. Morozova**, , R. Capdevila, F.X. Trias, and A. Oliva. Towards real-time CFD simulation of indoor environment. *In Proceedings of 10th International Conference on Computational Fluid Dynamics*, July 9-13, 2018, Barcelona, Spain.

References

[1] X. Cao, X. Dai, and J. Liu. Building energy-consumption status worldwide and the state-of-the-art technologies for zero-energy buildings during the past decade. *Energy and Buildings*, 128:198–213, 2016.

[2] O. Neu, S. Oxizidis, D. Flynn, F. Pallonetto, and D. Finn. High resolution space - time data: Methodology for residential building simulation modelling. In *Proceedings of 13th Conference of International Building Performance Simulation Association*, pages 2428–2435, August 26-28 2013.

[3] F. Oldewurtel, A. Parisio, C. N. Jones, D. Gyalistras, M. Gwerder, V. Stauch, B. Lehmann, and M. Morari. Use of model predictive control and weather forecasts for energy efficient building climate control. *Energy and Buildings*, 45:15–27, 2012.

[4] A. Afram and F. Janabi-Sharifi. Theory and applications of HVAC control systems - A review of model predictive control (MPC). *Building and Environment*, 72:343–355, 2014.

[5] Q. Chen. Ventilation performance prediction for buildings: A method overview and recent applications. *Building and Environment*, 44(4):848–858, 2009.

[6] J.-M. Fürbringer, C. A. Roulet, and R. Borchiellini. Annex 23: Multizone air flow modelling. Evaluation of COMIS. Technical report, International Energy Agency (IEA), 1996.

[7] J. Axley. Multizone airflow modeling in buildings: History and theory. *HVAC&R Research*, 13(6):907–928, 2007.

[8] L. C. Ng, W. S. Dols, and S. J. Emmerich. Evaluating potential benefits of air barriers in commercial buildings using NIST infiltration correlations in EnergyPlus. *Building and Environment*, 196:107783, 2021.

[9] A. Żabnieńska-Góra, N. Khordehgah, and H. Jouhara. Annual performance analysis of the PV/T system for the heat demand of a low-energy single-family building. *Renewable Energy*, 163:1923–1931, 2021.

[10] P. Eguía-Oller, S. Martínez-Mariño, E. Granada-Álvarez, and L. Febrero-Garrido. Empirical validation of a multizone building model coupled with an air flow network under complex realistic situations. *Energy and Buildings*, 249, 2021.

[11] J. Guo, J. Liu, D. Tu, J. Zhang, J. Xu, and P. Xue. Multizone modeling of pressure difference control analyses for an infectious disease hospital. *Building and Environment*, 206(92):108341, 2021.

[12] K. C. Mendonça, M. O. Abadie, C. Béghein, and P. Blondeau. Assessing the capabilities of the zonal model to predict the isothermal airflow induced by a linear ceiling diffuser. *Building Simulation*, 7:489–501, 2014.

[13] M. O. Abadie, M. M. de Camargo, K. C. Mendonça, and P. Blondeau. Improving the prediction of zonal modeling for forced convection airflows in rooms. *Building and Environment*, 48(1):173–182, 2012.

[14] A. C. Megri and H. Fariborz. Zonal modeling for simulating indoor environment of buildings: Review, recent developments, and applications. *HVAC&R Research*, 13(6):887–905, 2007.

[15] Y. Li and P. V. Nielsen. Commemorating 20 years of Indoor Air: CFD and ventilation research. *Indoor Air*, 21(6):442–453, 2011.

[16] T. van Hooff, B. Blocken, and Y. Tominaga. On the accuracy of CFD simulations of cross-ventilation flows for a generic isolated building: Comparison of RANS, LES and experiments. *Building and Environment*, 114:148–165, 2017.

[17] W. Chen, S. Liu, Y. Gao, H. Zhang, E. Arens, L. Zhao, and J. Liu. Experimental and numerical investigations of indoor air movement distribution with an office ceiling fan. *Building and Environment*, 130:14–26, 2018.

[18] Z. Chen, J. Xin, and P. Liu. Air quality and thermal comfort analysis of kitchen environment with CFD simulation and experimental calibration. *Building and Environment*, 172:106691, 2020.

[19] E. Katramiz, D. Al Assaad, N. Ghaddar, and K. Ghali. The effect of human breathing on the effectiveness of intermittent personalized ventilation

coupled with mixing ventilation. *Building and Environment*, 174:106755, 2020.

[20] X. Zheng, H. Montazeri, and B. Blocken. CFD simulations of wind flow and mean surface pressure for buildings with balconies: Comparison of RANS and LES. *Building and Environment*, 173:106747, 2020.

[21] H. Wang and Z. Zhai. Application of coarse-grid computational fluid dynamics on indoor environment modeling: Optimizing the trade-off between grid resolution and simulation accuracy. *HVAC&R Research*, 18(5):915–933, 2012.

[22] T. Kempe and A. Hantsch. Large-eddy simulation of indoor air flow using an efficient finite-volume method. *Building and Environment*, 115:291–305, 2017.

[23] R. Zhang and P. A. Mirzaei. CFD-CFD coupling: A novel method to develop a fast urban microclimate model. *Journal of Building Physics*, 44(5):385–408, 2021.

[24] H. Chen, X. Zhou, Z. Feng, and S. J. Cao. Application of polyhedral meshing strategy in indoor environment simulation: Model accuracy and computing time. *Indoor and Built Environment*, 0(0):1–13, 2021.

[25] F. Kuznik, C. Obrecht, G. Rusaouen, and J. J. Roux. LBM based flow simulation using GPU computing processor. *Computers & Mathematics with Applications*, 59(7):2380–2392, 2010.

[26] B. Elhadidi and H. E. Khalifa. Comparison of coarse grid lattice Boltzmann and Navier Stokes for real time flow simulations in rooms. *Building Simulation*, 6:183–194, 2013.

[27] M. A. I. Khan, N. Delbosc, C. J. Noakes, and J. Summers. Real-time flow simulation of indoor environments using lattice Boltzmann method. *Building Simulation*, 8:405–414, 2015.

[28] S. Chen and G. D. Doolen. Lattice Boltzmann method for fluid flows. *Annual Review of Fluid Mechanics*, 30:329–364, 1998.

[29] F. Marlow, J. Jacob, and P. Sagaut. A multidisciplinary model coupling Lattice-Boltzmann-based CFD and a Social Force Model for the simulation of pollutant dispersion in evacuation situations. *Building and Environment*, 205:108212, 2021.

[30] Z. A. Li, Y. T. Mu, Z. L. Gu, and W. Q. Tao. A multiscale method for predicting the long-term emission behaviors of semivolatile organic compounds. *Building and Environment*, 186:107285, 2020.

[31] J. Stam. Stable fluids. In *Proceedings of the 26th Annual Conference on Computer Graphics and Interactive Techniques*, pages 121–128, 1999.

[32] W Zuo and Q. Chen. Real-time or faster-than-real-time simulation of airflow in buildings. *Indoor Air*, 19(1):33–44, 2009.

[33] A. J. Chorin. A numerical method for solving incompressible viscous flow problems. *Journal of Computational Physics*, 135(2):118–125, 1997.

[34] W. Liu, H. Sun, D. Lai, Y. Xue, A. Kabanshi, and S. Hu. Performance of fast fluid dynamics with a semi-Lagrangian scheme and an implicit upwind scheme in simulating indoor/outdoor airflow. *Building and Environment*, 207:108477, 2022.

[35] R. Li, Z. Liu, L. Feng, and N. Gao. Fast fluid dynamics simulation of the airflow distributions in urban residential areas. *Energy and Buildings*, 255:111635, 2022.

[36] S. Yang, M. P. Wan, W. Chen, B. F. Ng, and D. Zhai. An adaptive robust model predictive control for indoor climate optimization and uncertainties handling in buildings. *Building and Environment*, 163:106326, 2019.

[37] J. Zhuang, Y. Chen, and X. Chen. A new simplified modeling method for model predictive control in a medium-sized commercial building: A case study. *Building and Environment*, 127:1–12, 2018.

[38] T. Zerihun Desta, K. Janssens, A. Van Brecht, J. Meyers, M. Baelmans, and D. Berckmans. CFD for model-based controller development. *Building and Environment*, 39(6):621–633, 2004.

[39] X. Zhou, H. Li, Y. C. Soh, and C. Jiang. Development of a novel strategy of CFD-based model predictive control. *Procedia Engineering*, 214:69–75, 2017.

[40] A. Afram, F. Janabi-Sharifi, A. S. Fung, and K. Raahemifar. Artificial neural network (ANN) based model predictive control (MPC) and optimization of HVAC systems: A state of the art review and case study of a residential HVAC system. *Energy and Buildings*, 141:96–113, 2017.

[41] L. Phan and C.-X. Lin. Reduced order modeling of a data center model with multi-Parameters. *Energy and Buildings*, 136:86–99, 2017.

[42] J. Athavale, M. Yoda, and Y. Joshi. Comparison of data driven modeling approaches for temperature prediction in data centers. *International Journal of Heat and Mass Transfer*, 135:1039–1052, 2019.

[43] W. Liu, R. Duan, C. Chen, C. H. Lin, and Q. Chen. Inverse design of the thermal environment in an airliner cabin by use of the CFD-based adjoint method. *Energy and Buildings*, 104:147–155, 2015.

[44] X. Wang, J. Zhao, F. Wang, B. Song, and Q. Zhang. Air supply parameter optimization of a custom nonuniform temperature field based on the POD method. *Building and Environment*, 206:108328, 2021.

[45] R. Ghosh and Y. Joshi. Dynamic reduced order thermal modeling of data center air temperatures. *ASME 2011 Pacific Rim Technical Conference and Exhibition on Packaging and Integration of Electronic and Photonic Systems, InterPACK 2011*, 2:423–432, 2011.

[46] G. Calzolari and W. Liu. Deep learning to replace, improve, or aid CFD analysis in built environment applications: A review. *Building and Environment*, 206:108315, 2021.

[47] P. Westermann and R. Evins. Surrogate modelling for sustainable building design â A review. *Energy and Buildings*, 198:170–186, 2019.

[48] A. E. Ruano, S. Pesteh, S. Silva, H. Duarte, G. Mestre, P. M. Ferreira, H. R. Khosravani, and R. Horta. The IMBPC HVAC system: A complete MBPC solution for existing HVAC systems. *Energy and Buildings*, 120:145 – 158, 2016.

[49] H. Huang, L. Chen, and E. Hu. A neural network-based multi-zone modelling approach for predictive control system design in commercial buildings. *Energy and Buildings*, 97:86–97, 2015.

[50] Q. Chen and N. Li. Fast simulation and high-fidelity reduced-order model of the multi-zone radiant floor system for efficient application to model predictive control. *Energy and Buildings*, 248:111210, 2021.

[51] W. Kim, Y. Jeon, and Y. Kim. Simulation-based optimization of an integrated daylighting and HVAC system using the design of experiments method. *Applied Energy*, 162:666–674, 2016.

[52] X. Wei, A. Kusiak, M. Li, F. Tang, and Y. Zeng. Multi-objective optimization of the HVAC (heating, ventilation, and air conditioning) system performance. *Energy*, 83:294–306, 2015.

[53] E. Asadi, M. G. Da Silva, C. H. Antunes, L. Dias, and L. Glicksman. Multi-objective optimization for building retrofit: A model using genetic algorithm and artificial neural network and an application. *Energy and Buildings*, 81:444–456, 2014.

[54] H. Sözer and S. S. Aldin. Predicting the indoor thermal data for heating season based on short-term measurements to calibrate the simulation set-points. *Energy and Buildings*, 202, 2019.

[55] D. Koschwitz, E. Spinnräker, J. Frisch, and C. van Treeck. Long-term urban heating load predictions based on optimized retrofit orders: A cross-scenario analysis. *Energy and Buildings*, 208:109637, 2020.

[56] H. Park and D. Y. Park. Comparative analysis on predictability of natural ventilation rate based on machine learning algorithms. *Building and Environment*, 195:107744, 2021.

[57] Q. Fang, Z. Li, Y. Wang, M. Song, and J. Wang. A neural-network enhanced modeling method for real-time evaluation of the temperature distribution in a data center. *Neural Computing and Applications*, 31(12):8379–8391, 2019.

[58] A. Warey, S. Kaushik, B. Khalighi, M. Cruse, and G. Venkatesan. Data-driven prediction of vehicle cabin thermal comfort: using machine learning and high-fidelity simulation results. *International Journal of Heat and Mass Transfer*, 148:119083, 2020.

[59] T. H. Zhang and X. Y. You. Applying neural networks to solve the inverse problem of indoor environment. *Indoor and Built Environment*, 23(8):1187–1195, 2014.

[60] X. Tian, Y. Cheng, and Z. Lin. Modelling indoor environment indicators using artificial neural network in the stratified environments. *Building and Environment*, 208:108581, 2021.

[61] C. Lamberti, G.and Gorlé. A multi-fidelity machine learning framework to predict wind loads on buildings. *Journal of Wind Engineering and Industrial Aerodynamics*, 214:104647, 2021.

[62] N. Li, L. Yang, X. Li, X. Li, J. Tu, and S. C. P. Cheung. Multi-objective optimization for designing of high-speed train cabin ventilation system using particle swarm optimization and multi-fidelity Kriging. *Building and Environment*, 155:161–174, 2019.

[63] X. Zhang, T. Xie, F.and Ji, Z. Zhu, and Y. Zheng. Multi-fidelity deep neural network surrogate model for aerodynamic shape optimization. *Computer Methods in Applied Mechanics and Engineering*, 373:113485, 2021.

[64] Z. Zhang, W. Zhang, Z. J. Zhai, and Q. Y. Chen. Evaluation of various turbulence models in predicting airflow and turbulence in enclosed environments by CFD: Part-2: Comparison with experimental data from literature. *HVAC&R Research*, 13(6):871–886, 2007.

[65] A. Limane, H. Fellouah, and N. Galanis. Thermo-ventilation study by OpenFOAM of the airflow in a cavity with heated floor. *Building Simulation*, 8(3):271–283, 2015.

[66] G. Yang, Y. Huang, J. Wu, L. Zhang, G. Chen, R. Lv, and A. Cai. Experimental study and numerical models assessment of turbulent mixed convection heat transfer in a vertical open cavity. *Building and Environment*, 115:91–103, 2017.

[67] J. Y. Wu, R. R. Lv, Y. Y. Huang, and G. Yang. Flow Structure Transition and Hysteresis of Turbulent Mixed Convection Induced by a Transverse Buoyant Jet. *International Journal of Heat and Mass Transfer*, 177, 2021.

[68] B. E. Yuce and E. Pulat. Forced, natural and mixed convection benchmark studies for indoor thermal environments. *International Communications in Heat and Mass Transfer*, 92:1–14, 2018.

[69] J. Salat, S. Xin, P. Joubert, A. Sergent, F. Penot, and P. Le Quéré. Experimental and numerical investigation of turbulent natural convection in a large air-filled cavity. *International Journal of Heat and Fluid Flow*, 25(5):824–832, 2004.

[70] D. Blay, S. Mergui, J. L. Tuhault, and F. Penot. Experimental turbulent mixed convection created by confined buoyant wall jets. In *Proceedings of the First European Heat Transfer Conference, UK*, pages 821–828, 1992.

[71] X. Álvarez, A. Gorobets, F. X. Trias, R. Borrell, and G. Oyarzun. HPC^2 âa fully-portable, algebra-based framework for heterogeneous computing. application to cfd. *Computers and Fluids*, 173:285–292, 2018.

[72] N. Morozova, F. X. Trias, R. Capdevila, C. D. Pérez-Segarra, and A. Oliva. On the feasibility of affordable high-fidelity CFD simulations for indoor environment design and control. *Building and Environment*, 184:107144, 2020.

[73] Termo Fluids S.L. Termofluids. `http://www.termofluids.com/`, 2022.

[74] A. Gorobets, F. X. Trias, M. Soria, and A. Oliva. A scalable parallel Poisson solver for three-dimensional problems with one periodic direction. *Computers & Fluids*, 39(3):525–538, 2010.

[75] I. Rodriguez, R. Borell, O. Lehmkuhl, C. D. Pérez-Segarra, and A. Oliva. Direct numerical simulation of the flow over a sphere at Re = 3700. *Journal of Fluid Mechanics*, 679:263–287, 2011.

[76] I. Rodriguez, O. Lehmkuhl, J. Chiva, R. Borell, and A. Oliva. On the flow past a circular cylinder from critical to super-critical reynolds numbers: Wake topology and vortex shedding. *International Journal of Heat and Fluid Flow*, 55:91–103, 2015.

[77] E. Gutiérrez, N. Balcázar, E. Bartrons, and J. Rigola. Numerical study of taylor bubbles rising in a stagnant liquid using a level-set/moving-mesh method. *Chemical Engineering Science*, 164:158–177, 2017.

[78] P. A. Galione, O. Lehmkuhl, J. Rigola, and A. Oliva. Fixed-grid numerical modeling of melting and solidification using variable thermo-physical properties â application to the melting of n-octadecane inside a spherical capsule. *International Journal of Heat and Mass Transfer*, 86:721–743, 2015.

[79] R. Borrell, J. Chiva, O. Lehmkuhl, G. Oyarzun, I. RodrÃguez, and A. Oliva. Optimising the termofluids cfd code for petascale simulations. *International Journal of Computational Fluid Dynamics*, 30(6):425–430, 2016.

[80] A. V. Gorobets, F. X. Trias, and A. Oliva. A parallel mpi+openmp+opencl algorithm for hybrid supercomputations of incompressible flows. *Computers and Fluids*, 88:764–772, 2013.

[81] F. X. Trias, M. Soria, A. Oliva, and C. D. Pérez-Segarra. Direct numerical simulations of two- and three-dimensional turbulent natural convection flows in a differentially heated cavity of aspect ratio 4. *Journal of Fluid Mechanics*, 586:259–293, 2007.

[82] J. E. Jaramillo, F.X. Trias, A. Gorobets, C. D. Pérez-Segarra, and A. Oliva. Dns and rans modelling of a turbulent plane impinging jet. *International Journal of Heat and Mass Transfer*, 55(4):789–801, 2012.

[83] F.X. Trias, F. Dabbagh, A. Gorobets, and C. Oliet. On a proper tensor-diffusivity model for large-eddy simulation of buoyancy-driven turbulence. *Flow, Turbulence and Combustion*, 105(2):393–414, 2020.

[84] F.X. Trias, D. Folch, A. Gorobets, and A. Oliva. Building proper invariants for eddy-viscosity subgrid-scale models. *Physics of Fluids*, 27(6), 2015.

[85] F.X. Trias, D. Folch, A. Gorobets, and A. Oliva. Spectrally-consistent regularization of navierâstokes equations. *Journal of Scientific Computing*, 79(2):992–1014, 2019.

[86] F.X. Trias, A. Gorobets, C.D. PÃ©rez-Segarra, and A. Oliva. Numerical simulation of turbulence at lower costs: Regularization modeling. *Computers and Fluids*, 80(1):251–259, 2013.

[87] The OpenFOAM Foundation. OpenFOAM. `https://www.openfoam.org/`, 2022.

2

On the feasibility of affordable high-fidelity CFD simulations for indoor environment design and control

Main content of this chapter has been published in:

N. Morozova, F.X. Trias, R. Capdevila, C. D. Pérez-Segarra and A. Oliva. On the feasibility of affordable high-fidelity CFD simulations for indoor environment design and control. *Building and Environment*, **184**:107144, 2020.

Abstract: Computational fluid dynamics (CFD) is a reliable tool for indoor environmental applications. However, accurate CFD simulations require large computational resources, whereas significant cost reduction can lead to unreliable results. The high cost prevents CFD from becoming the primary tool for indoor environmental simulations. Nonetheless, the growth in computational power and advances in numerical algorithms provide an opportunity to use accurate and yet affordable CFD. The objective of this study is to analyze the feasibility of fast, affordable, and high-fidelity CFD simulations for indoor environment design and control using ordinary office computers. We analyze two representative test cases, which imitate common indoor airflow configurations, on a wide range of different turbulence models and discretizations methods to meet the requirements for the computational cost, run-time, and

accuracy. We consider statistically steady-state simulations for indoor environment design and transient simulations for control. Among studied turbulence models, the no-model and large-eddy simulation with staggered discretizations show the best performance. We conclude that high-fidelity CFD simulations on office computers are too slow to be used as a primary tool for indoor environment design and control. Taking into account different laws of computer growth prediction, we estimate the feasibility of high-fidelity CFD on office computers for these applications for the next decades.

2.1 Introduction

Heating ventilation and air conditioning (HVAC) systems account for approximately 40% of the energy consumption in buildings [1], which can be decreased by proper design and precise control of indoor air parameters. Therefore, the fast computation of indoor airflow is required for testing different design options or performing model predictive control (MPC) using real-time weather and occupant's behavior data. Nowadays, air distribution in buildings is usually evaluated by multizone models [2], zonal models [3], and computational fluid dynamics (CFD). Multizone models are the most popular choice due to the low computational cost, but they have limited applicability because each room is represented by only one node. Zonal models are considered intermediate between multizone and CFD; however, they usually suffer from case dependency. In CFD, the physical domain is divided into a finite number of control volumes to solve the Navier-Stokes equations numerically. The solution provides a complete set of air parameters for each control volume.

Its high computational cost prevents CFD from becoming the primary design tool, and it is mainly used for particular high-end buildings. To become a primary design tool, CFD is required to provide sufficient accuracy in capturing flow properties, be fast, and fit into an office computer. The indoor airflow is usually a multi-scale problem requiring fine computational grids [4]. Moreover, the majority of indoor airflows are turbulent. The effect of turbulence can be accurately resolved using direct numerical simulation (DNS) or modeled using large-eddy simulation (LES) or Reynolds average Navier-Stokes (RANS) approaches. LES models are computationally more expensive than RANS, and both methods have a lower computational cost than DNS.

CFD has been successfully used for detailed simulations of building airflows by many researchers [5–9]. Nevertheless, all of these studies show the need for a compromise between computational cost and accuracy. Van Hooff *et al.* [5] performed CFD simulations of a generic isolated building. They used a computational grid of 5×10^6 control volumes to achieve reliable results, which required to use 14 CPU cores on a high-performance computer. Other studies also indicate the high computational cost of CFD. For example, Chen *et al.* [7] showed that an accurate simulation of a kitchen room would require at least 10^6 control volumes. Chen *et al.* [6] used a grid of 4×10^6 control volumes for an accurate simulation of an office room with a ceiling fan. Zheng *et al.* [9] studied the wind flow for buildings with balconies using a fine mesh of 2×10^7 cells. An ordinary office computer does not have sufficient memory and CPU power to complete such large simulations in a reasonable amount of time for indoor environment design and control. Moreover, the widely used RANS turbulence models do not always produce satisfactory results, making the use of more accurate (and more expensive) turbulence models indispensable [5,9].

Accurate CFD simulations require large computational resources, while using ordinary office computers can result in unreasonably long run-times. Grid coarsening and RANS turbulence modeling are common ways to reduce the cost of CFD, but they can lead to overly inaccurate results. Therefore, the task of performing affordable yet accurate CFD is not straightforward.

Over the last decade, several attempts to reduce the computational cost of CFD for indoor environmental applications have been made. Wang & Zhai [10] examined the credibility of coarse-grid CFD for HVAC applications and optimized the space discretization to reduce the total truncation error. Kempe & Hantsch [11] applied the immersed boundary method to an LES simulation of a room with a heat source and achieved real-time LES simulations with 32 CPU cores. However, they did not provide an extensive error analysis to evaluate the accuracy of the simulations. Moreover, they did not study the transient flows and did not consider different turbulence models. As an alternative to CFD, the lattice Boltzmann method (LBM) [12–14] and fast fluid dynamics (FFD) [15,16] were applied for indoor environmental simulations. LBM time step is limited by the advection term, which makes it slower than CFD with similar grid resolutions [13]. Zuo & Chen [16] adapted FFD for airflow in buildings and introduced turbulence modeling. FFD has lower computing cost but also lower accuracy than CFD [16].

Another important application is indoor environment control. MPC elaborates a model of the system evolution and executes control actions based on it [17]. Usually, low order models such as multizone are used in MPC [18,19]. So far, CFD has not been integrated into MPC directly due to the huge computational cost and nonlinearity of the governing equations. However, several preliminary attempts have been made to simplify CFD to fit MPC requirements [20,21]. The growth in computational power provides an opportunity to test the feasibility of CFD for MPC. Typically, building MPC systems have a control horizon of 4-5 hours [22], which is relatively short for building dynamics scale; thus, transient simulations are required. Moreover, CFD simulations for MPC should be faster than real-time and computationally affordable.

The objective of this work is to study the feasibility of affordable high-fidelity CFD for indoor environmental applications. We consider two representative cases, namely, a tall differentially-heated cavity and a ventilated cavity with a heated floor. We test both cases on a wide range of staggered and collocated grids with different LES, RANS, and DNS approaches. Performed CFD simulations are analyzed in terms of computational cost and accuracy in order to meet the requirements for indoor environmental applications. The work is primarily focused on steady CFD for design and transient CFD for MPC in buildings, using affordable office computers.

The content of this chapter is organized as follows: Section 2.2 describes the details of the test cases and the governing equations, Section 2.3 describes the numerical methods, Sections 2.4, 2.5 and 2.6 show obtained results and their analysis, Section 2.7 discusses results and their applications, and Section 2.8 contains concluding remarks.

2.2 Governing equations and physical problems

2.2.1 Governing equations

The incompressible Navier-Stokes equations for a Newtonian fluid with constant physical properties are considered. The Boussinesq approximation is adopted to account for the density variations due to temperature difference. Thermal radiation is neglected. Under these assumptions, the governing equations are

$$\nabla \cdot \mathbf{u} = 0, \tag{2.1}$$

$$\frac{\partial \mathbf{u}}{\partial t} + (\mathbf{u} \cdot \nabla)\mathbf{u} = \nu \nabla^2 \mathbf{u} - \nabla p + \beta \mathbf{g} \Delta T, \tag{2.2}$$

$$\frac{\partial T}{\partial t} + (\mathbf{u} \cdot \nabla) T = \alpha \nabla^2 T, \tag{2.3}$$

where $\mathbf{u} = (u, v, w)$ is the velocity vector in Cartesian coordinates $\mathbf{x} = (x, y, z)$, p the kinematic pressure, T the temperature, ν the kinematic viscosity, ρ the density, $\mathbf{g}$ the gravitational acceleration, β the thermal expansion coefficient and α the thermal diffusivity.

Hereafter, all the results are presented in dimensionless form. The reference values of time velocity temperature and length are specified for each problem separately.

2.2.2 Test case 1: Differentially heated cavity

The first test case is a three-dimensional tall cavity driven by buoyancy forces. The objective of this configuration is to mimic a highly stratified turbulent indoor environment with natural convection. This airflow can be found in a tall building atrium, or a staircase. Natural convection is important for the thermal comfort, thus, its correct prediction is crucial for building applications. The cavity has a height aspect ratio of $A_h = H/W = 3.84$ and a depth aspect ratio of $A_d = D/W = 0.86$ (Figure 4.1, left). The Prandtl number corresponds to air and is equal to $Pr = \nu/\alpha = 0.71$ and the Rayleigh number is $Ra_H = \rho g \beta \Delta T H^3/(\nu\alpha) = 1.2 \times 10^{11}$. This configuration resembles the experimental set-up performed by Saury *et al.* [23]: the two opposite vertical walls of the cavity in the x direction are maintained at uniform temperatures $T_h = 0.5$ at $x = 0$ and $T_c = -0.5$ at $x = W$. The temperature at the rest of the walls is given by the "Fully Realistic" boundary conditions proposed in [24]. They are time independent analytical functions that fit the experimental data obtained by Salat *et al.* [25].

In the experiment by Saury *et al.* [23] the cavity is 3.84 m high, 1 m wide, 0.86 m deep and is exposed to a temperature difference of $\Delta T = 20°C$. The air properties are the following: $\nu = 1.51 \times 10^{-5} m^2/s$, $\alpha = 2.13 \times 10^{-5} m^2/s$, $\rho = 1.2 kg/m^3$, $g = 9.81 m/s^2$ and $\beta = 2.90 \times 10^{-3} m^3/(kg°C)$.

For this test case the reference length is H and the reference velocity, time and temperature used for the dimensionless form are, respectively, $Ra_H^{1/2}(\alpha/H)$, $Ra_H^{-1/2}(H^2/\alpha)$ and ΔT. Initial temperature conditions repeat the temperature profile of the front/rear wall boundaries. The initial velocity is set to zero.

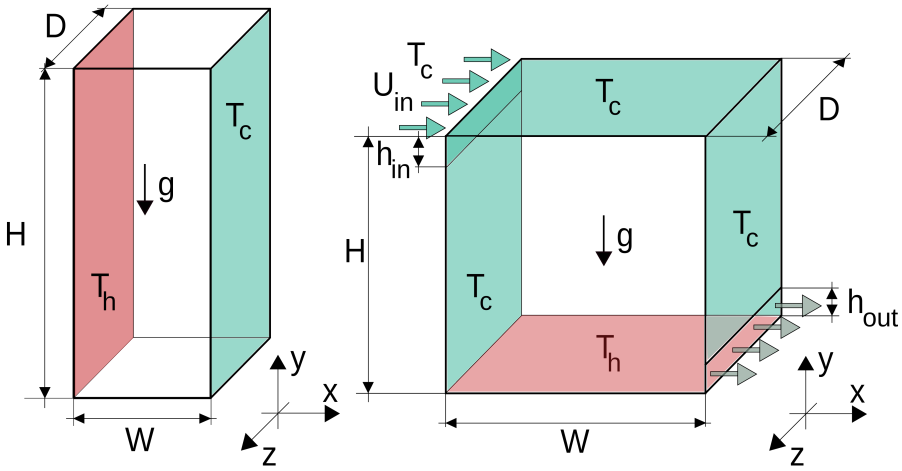

Figure 2.1: Left: geometry of the differentially heated cavity case. Right: geometry of the mixed convection case.

As detailed in Table 2.1, we used twelve different Cartesian structured grids for the numerical tests. Grid M1.0 was used in the reference DNS simulation, which was previously published in Álvarez *et al.* [26]. All the grids are, uniform in the vertical (y) and spanwise (z) directions, and refined near the lateral walls (x) using the hyperbolic tangential function:

$$x = \frac{W}{2}\left(1 + \frac{\tanh\gamma_x(2(i-1)/N_x - 1)}{\tanh\gamma_x}\right), \tag{2.4}$$

where the concentration factor is $\gamma_x = 2$ and N_x is the number of grid points in the horizontal direction. All steady simulations run for 600 non-dimensional time units, which was found to be a long enough time-integration period to record the flow statistics for further averaging. All transient simulations were carried out for 10 non-dimensional time units to capture the initial flow development.

2.2.3 Test case 2: Mixed convection in a ventilated cavity

The second test case is a three-dimensional ventilated cavity with a heated floor. This configuration was first studied experimentally by Blay *et al.* [27] and later numerically by Ezzouhri *et al.* [28]. The geometry of the studied cavity is shown in Figure 4.1 (right). The height aspect ratio of the cavity is $A_h = H/W = 1$ and the depth aspect ratio is $A_d = D/W = 0.3/1.04$. Cold air at $T_c = -0.5$ enters the cavity through the long thin inlet at the top of the left wall. The inlet velocity profile in the vertical (y) direction corresponds to a parabolic Poiseuille flow with a bulk velocity $U_{in} = 1$. The inlet slot has an aspect ratio $A_{in} = h_{in}/H = 0.018/1.04$. The

Table 2.1: Computational grids used in the simulations of the differentially heated cavity case (test case 1).

Case	N_x	N_y	N_z	N_{total}
M1.0 (DNS)	450	900	256	1.04×10^8
M1.1	8	30	4	9.60×10^2
M1.2	10	40	6	2.40×10^3
M1.3	12	50	8	4.80×10^3
M1.4	14	60	10	8.40×10^3
M1.5	18	80	12	1.73×10^4
M1.6	24	100	16	3.84×10^4
M1.7	30	120	20	7.20×10^4
M1.8	40	150	24	1.44×10^5
M1.9	50	180	30	2.70×10^5
M1.10	70	240	40	6.72×10^5
M1.11	80	320	50	1.28×10^6
M1.12	100	400	60	2.40×10^6

air is discharged through the outlet with an aspect ratio $A_{out} = h_{out}/H = 0.024/1.04$ at the bottom of the right wall of the cavity. The bottom wall is maintained at a hot temperature of $T_h = 0.5$, while the three other sidewalls are kept at the cold temperature of $T_c = -0.5$. Periodic boundary conditions are used in the spanwise (z) direction.

The cavity is filled with air $(Pr = 0.71)$ at Rayleigh number based on the cavity height $Ra_H = 2.4 \times 10^9$. Froude number based on the inlet height is equal to $Fr_{h_{in}} = U_{in}/\sqrt{\rho g \beta \Delta T h_{in}} = 5.24$, Reynolds number based on the inlet height is $Re_{h_{in}} = U_{in}h_{in}/\nu = 684$. At the outlet, convective boundary conditions $(\partial\phi/\partial t + U_{in}\partial\phi/\partial x = 0)$ are imposed for the velocity and temperature. No-slip boundary conditions are applied on the walls. The initial velocity field is set to zero and the initial temperature is set equal to the temperature at the cold wall.

The experimental setup by Blay *et al.* [27] has height and width of 1.04 m and depth of 0.3 m. The inlet slot has a height of 0.018 m and the outlet slot - 0.024 m. The temperature difference is $\Delta T = 20°C$ and the inlet bulk velocity is $U_{in} = 0.57 m/s$. The air properties are the following: $\nu = 1.5 \times 10^{-5} m^2/s$, $\alpha = 2.1 \times 10^{-5} m^2/s$, $\rho = 1.2 kg/m^3$ and $g = 9.81 m/s^2$.

In this test case, the reference values used for non-dimensionalizing are the cavity height H, the time $t_{ref} = H/U_{ref}$, the velocity $U_{ref} = U_{in}$ and the temperature difference ΔT. This flow configuration is a mixed convection phenomenon. It resembles an airflow in a room with mixing ventilation and thermal exhausts. The aspect ratios of the inlet and the outlet are very similar to the real-size rooms.

Table 2.2: Computational grids used in the simulations of the mixed convection case (test case 2).

Case	N_x	$N_{out} + N_{bulk} + N_{in} = N_y$	N_z	N_{total}
M2.0 (DNS)	512	$57 + 398 + 57 = 512$	128	3.36×10^7
M2.1	10	$2 + 10 + 3 = 15$	4	6.00×10^2
M2.2	15	$2 + 20 + 3 = 25$	4	1.50×10^3
M2.3	20	$2 + 25 + 3 = 30$	4	2.40×10^3
M2.4	30	$4 + 32 + 4 = 40$	4	4.80×10^3
M2.5	40	$4 + 32 + 4 = 40$	6	9.60×10^3
M2.6	40	$6 + 48 + 6 = 60$	8	1.92×10^4
M2.7	50	$6 + 48 + 6 = 60$	12	3.60×10^4
M2.8	60	$7 + 60 + 8 = 75$	16	7.20×10^4
M2.9	80	$10 + 70 + 10 = 90$	20	1.44×10^5
M2.10	100	$15 + 90 + 15 = 120$	24	2.88×10^5
M2.11	120	$20 + 120 + 20 = 160$	30	5.76×10^5
M2.12	160	$20 + 140 + 20 = 180$	40	1.15×10^6

Cartesian structured grids detailed in Table 2.2 were used for this test case. All grids are uniform in the spanwise (z) direction. In the horizontal (x) direction grids are refined near the walls using the hyperbolic tangent function given in equation (2.4) with a concentration factor $\gamma_x = 1.5$. In the vertical (y) direction the grids are uniform in the zones of inlet (N_{in}) and outlet (N_{out}) and refined near the lateral walls in the bulk part $(\gamma_y = 2)$. All simulations run for 500 and 10 non-dimensional time units, respectively for steady and transient cases.

2.3 Numerical methods

We use three different software to perform the simulations:

- OpenFOAM v1706 [29] for unsteady RANS (URANS) approach using finite-volume discretization on collocated grids with fully implicit Euler time integration scheme;
- TermoFluids [30], an in-house CFD code for LES and no-model approaches using symmetry-preserving finite-volume discretization on collocated grids [31] with a one-parameter fully explicit second-order temporary discretization scheme [32];

- STG [33, 34], an in-house CFD code for LES, DNS and no-model simulations using symmetry-preserving finite volume discretization on staggered grids [35] with a one-parameter fully explicit second-order temporary discretization scheme [32].

The choice of the turbulence models is based on the findings of Morozova *et al.* [36] and Zhai *et al.* [37] for steady simulations and on findings of Morozova *et al.* [38] for transient simulations.

2.3.1 Unsteady Reynolds-averaged Navier-Stokes approach

The RANS approach is based on the time-averaged filtering of the governing equations (4.1) - (4.3). RANS equations calculate only averaged flow; thus, they are not suitable to describe the transient flow evolution. For this reason, the URANS approach is adopted. URANS equations are obtained when the temporal derivative of velocity is averaged over a chosen finite time. More details on the URANS can be found in [39]. The computational time of the URANS approach is smaller than LES or DNS; hence it is widely used for industrial applications. However, URANS does not always provide sufficient accuracy for the simulations. Nevertheless, it is interesting to test URANS models, as they offer computational time reduction.

In this study three different RANS turbulence models are tested: $k-\epsilon$ [40], RNG $k-\epsilon$ [41] and SST $k-\omega$ [42]. During the numerical experiments, the SST $k-\omega$ model showed the best transient predictions among all the URANS models, but the $k-\epsilon$ model has given better results for the steady flow. The RNG $k-\epsilon$ and $k-\epsilon$ models showed similar performance in terms of accuracy, but the $k-\epsilon$ model had a lower computational cost. Thus, the $k-\epsilon$ and SST $k-\omega$ models are chosen for further analysis. Results of the simulations with the RNG $k-\epsilon$ model are published online in the data archive [43].

2.3.2 Large-eddy simulation approach

A different approach to turbulence modeling is LES. Namely, the large-scale turbulent motions are resolved, whereas the effects of the smallest-scale motions are modeled using a subgrid-scale (SGS) model. In this work, three different SGS models are tested: the WALE model [44], the VMS-WALE [45], the QR [46] and the S3PQ model [47]. In terms of computational cost, LES lies between URANS and DNS. Since the large-scale unsteady motions are represented explicitly, LES can be expected to be more accurate and reliable than URANS for flows in which large-scale unsteadiness is significant, including unsteady separation and vortex shedding [48]. In this work, we carry out the spatial discretization in LES simulations using symmetry preserving discretization on structured collocated [31] and staggered [35] Cartesian grids.

In a staggered grid discretization arrangement, the scalar variables are stored at the cell centers of the control volumes, whereas the vector variables are stored at the cell faces. In a collocated grid discretization, on the other hand, all variables are stored at the cell centers. A staggered grid discretization helps avoid odd-even decoupling between the pressure and velocity (a discretization error that leads to unphysical pressure fields). However, the implementation of the staggered arrangement on the unstructured grids could be extremely complex [31]. Thus, the majority of the common CFD codes use collocated grids with special numerical treatments, which, however, cause considerable numerical dissipation [49]. Nonetheless, many HVAC problems do not require an unstructured grid; therefore, they could be easily used with a staggered grid discretization. This could improve simulation accuracy and reduce numerical dissipation [31,35] since staggered methods do not require any special numerical treatment. Discretization methods can have an important effect on the simulation stability and the accuracy of the results, especially for the coarsest grids. This reduction of the artificial numerical dissipation is not relevant for RANS models because the dissipation introduced by the model itself is much larger [49]; therefore, staggered grid discretization is only applied to LES and no-model approaches.

LES models tested on collocated grids are WALE, VMS-WALE, and QR. For both test cases, WALE and QR show similar computational costs, but the VMS-WALE is more expensive due to the additional filtering operations. However, the QR model under-predicted overall heat transfer. For these reasons, we choose the WALE model for further tests. Results of the simulations for the VMS-WALE and QR models are published in the data archive [43]. WALE, QR, and S3PQ turbulence models are tested on structured staggered grids. All three LES models showed similar results, but the WALE had the highest computational cost, and the QR showed the least accurate results. The S3PQ model is chosen for further simulations. Results for the WALE and QR models are published in the online data archive [43].

2.3.3 No-model approach

The no-model approach is similar to DNS, which consists of solving the Navier-Stokes equations, resolving all the scales of motion [48]. Conceptually DNS is the simplest approach, and it is unrivaled in accuracy. However, the cost is extremely high; and the computer requirements increase so rapidly with Reynolds number that the applicability of the approach is very limited even for the research. The no-model approach, like DNS, does not use any model for turbulence. Nonetheless, the computational grid used for no-model simulations is not fine enough to resolve all the turbulent flow scales. Despite the unresolved flow scales, the no-model approach is capable of producing reasonable results. Moreover, the absence of a turbulence model reduces the computational cost.

2.4 Results of the steady-state analysis

The ability for real-time simulations is always a compromise between available computing power and required accuracy. The focus of this paper is on the possibility of real-time CFD on office computers. We performed all the simulations on a machine with an AMD Opteron 2350 processor with a $24 Gb/s$ memory bandwidth. Then we re-scaled computational time to Intel Core i9-9900K processor with $41.6 Gb/s$ memory bandwidth, which is a modern but affordable processor. CFD codes are usually memory-bound and tend to exhibit irregular access patterns to data [50]. The High-Performance Conjugate Gradient benchmark, proposed by Dongarra *et al.* [50] shows, that the computational performance of CFD applications is mostly limited by a processor's bandwidth. Thus, assuming the ideal behavior of the solvers, we re-scaled all the simulations using linear dependencies of the processor's memory bandwidth and the number of nodes. The indicator to evaluate the performance of the solvers is the time ratio between the computational time, t_{sim}, and physically simulated time, $t_{phy} = t \cdot t_{ref}$. A simulation is faster than real-time when $R < 1$.

$$R = \frac{t_{sim}}{t_{phy}}, \tag{2.5}$$

To evaluate the overall quality of the simulations, we choose five global flow quantities for comparison: Nusselt number, stratification, kinetic energy, enstrophy, and the temperature of the cavity. They represent basic airflow properties and are relevant to the thermal comfort [51]. Nusselt number, stratification, and temperature represent the thermal properties of the flow. Nusselt is a measure of heat transfer. It is computed using the temperature gradient at the wall. Stratification corresponds to a vertical temperature gradient, and the average temperature is the operative room temperature. Kinetic energy measures the level of motion. Enstrophy corresponds to turbulence intensity. Both kinetic energy and enstrophy are used to measure draught and local discomfort.

$$Nu = -\frac{1}{A}\int_A \frac{\partial T}{\partial x} dA \quad \text{at} \quad x = 0 \tag{2.6}$$

$$S = \frac{\partial T}{\partial y} \quad \text{at} \quad x = \frac{W}{2}, \quad y = \frac{H}{2}, \quad z = \frac{D}{2} \tag{2.7}$$

$$E = \frac{1}{V}\int_V \frac{\mathbf{u}^2}{2} dV \tag{2.8}$$

$$\Omega = \frac{1}{V}\int_V \boldsymbol{\omega}^2 dV \tag{2.9}$$

$$T_V = \frac{1}{V}\int_V T dV, \tag{2.10}$$

where A is the surface of the hot wall, V is the volume of the cavity and $\boldsymbol{\omega} = \nabla \times \mathbf{u}$ is the vorticity. All these quantities are time-dependent, and for the steady-state evaluation they are averaged over time. Standard bracket "<>" notation is used for time-averaged values.

The design of HVAC systems is normally divided into two stages: early conceptual design and final detailed design. In the former, highly accurate simulations are not required. At this stage of a project, only conceptual decisions are made. More important for conceptual design is the ability to have fast calculations. For this design stage, a 15% relative error is assumed acceptable. On the other hand, final stage design applications require accurate and detailed simulation results. Therefore, a relative error of the global quantities should remain below 5%, as it is suggested in [52]. A building project in many cases requires several representative daily simulations [53]. We assume the simulation speed for HVAC design should be at least twice faster than real-time $(R \leqslant 0.5)$ so that an engineer can start a daily simulation at the end of the working day and obtain the results the next morning.

Figures 2.2 - 2.6 show global airflow quantities plotted with different grid resolutions and turbulence models against the computational time ratio in a semi-logarithmic scale. Each point of the graph corresponds to a mesh from Tables 2.1 and 2.2, respectively. On the left side of the graphs, there are less computationally expensive and less accurate coarse grids with a small ratio R. The mesh resolution is increasing while moving from the left to the right side of the graphs. The thick horizontal black line is the reference value, obtained in the DNS simulations. Gray areas around the reference line show the 5% and 15% error margins, respectively.

2.4.1 Test case 1 - differentially heated cavity. Results of the steady simulations

For this test case we investigate four global quantities: the average Nusselt number, the average stratification, the average kinetic energy and the average enstrophy. We compare them against the DNS data, published in [26].

All the turbulence models except URANS $k-\epsilon$ predict the average Nusselt number (Figure 2.2, top) rather well. All approaches show small values of $<Nu>$ on coarse grids, but from mesh M1.5 onward, results start falling into the 15% error range. URANS simulations have the least accurate predictions, although their computational cost is the smallest. LES (with both discretization approaches) and no-model on collocated grids show the best results and perform faster than real-time simulations with less than 15% relative error. Average stratification (Figure 2.2, bottom) shows good accuracy for most of the approaches. The errors are mostly originating from the fact that it is not an integral quantity. Both no-model techniques predict stratification accurately. URANS $k-\epsilon$ model is giving an accurate prediction, while SST $k-\omega$ is experiencing errors. Both LES simulations perform faster than real-time with about 15% relative error.

Average kinetic energy (Figure 2.3) is well predicted only by the LES-S3PQ model on staggered grids. Relatively small values of kinetic energy make its correct prediction more difficult. LES-WALE and both no-model approaches have converged to the DNS solution only for the finest meshes (M1.11 and M1.12 from Table 2.1), and URANS failed to predict average kinetic energy correctly for all the mesh resolutions. None of the methods achieves faster than real-time performance with required accuracy.

Average enstrophy (Figure 2.4) is a characteristic of turbulence cascade, so it is the most difficult quantity to predict accurately. No-model and LES methods provide sufficiently accurate results, however, they are not faster than real-time. Both URANS models, on the other hand, fail to give accurate values of the enstrophy. A significant difference in the accuracy of the results is due to the nature of turbulence modeling. Unlike the other approaches, URANS does not solve the turbulent fluctuations in time, which is the reason for its low accuracy.

From the simulation results could be concluded that, despite the lowest computational cost, URANS simulations have the least accurate predictions of the averaged global quantities of the differentially-heated cavity test case. Both LES models show similar levels of accuracy. No-model simulations on collocated grids show large errors on coarse grids. On the other hand, no-model approach on staggered grids has more stable behavior than the collocated discretization. On fine grids, no-model and LES approaches provide similar results. In general, the LES-S3PQ model on staggered grids shows the best trade-off between computational cost and accuracy for the steady-state analysis of the differentially-heated cavity test case. It reaches the desired accuracy of 15% and 5% with time ratios of $R \approx 25$ and $R \approx 60$, respectively. The

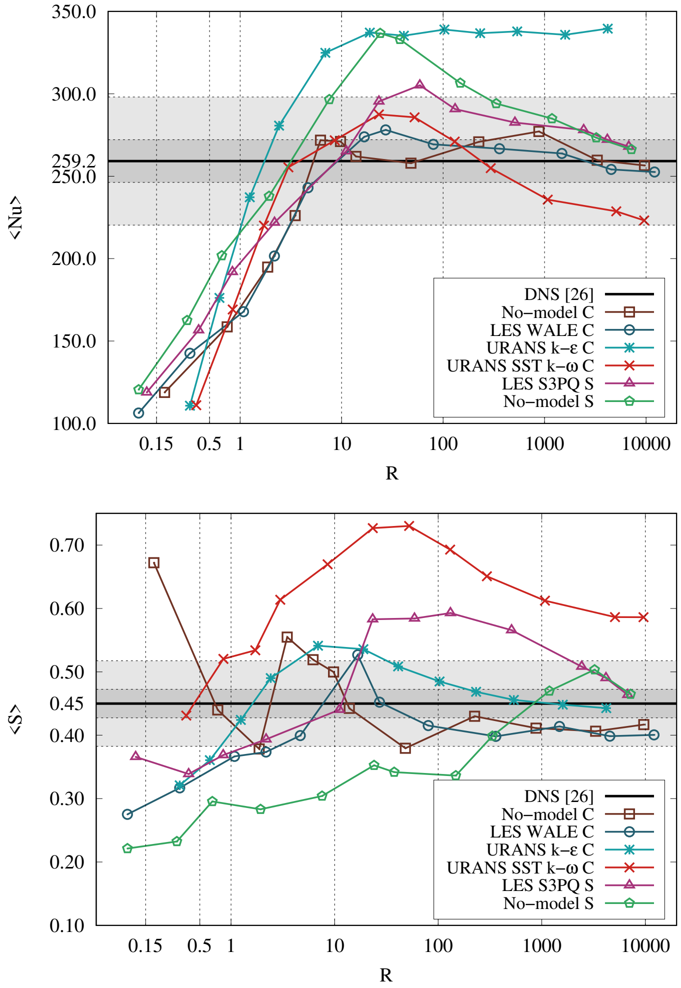

Figure 2.2: Test case 1. Steady-state analysis. Average Nusselt number (top) and average stratification (bottom) on different grid resolutions and turbulence models against time ratio. Each point in the graph corresponds to a mesh from Table 2.1. "C" stands for collocated grid discretization and "S" - for staggered.

least accurate prediction is provided by the URANS SST $k - \omega$ model. Nusselt number appears to be the easiest quantity to predict, while enstrophy is the most difficult one.

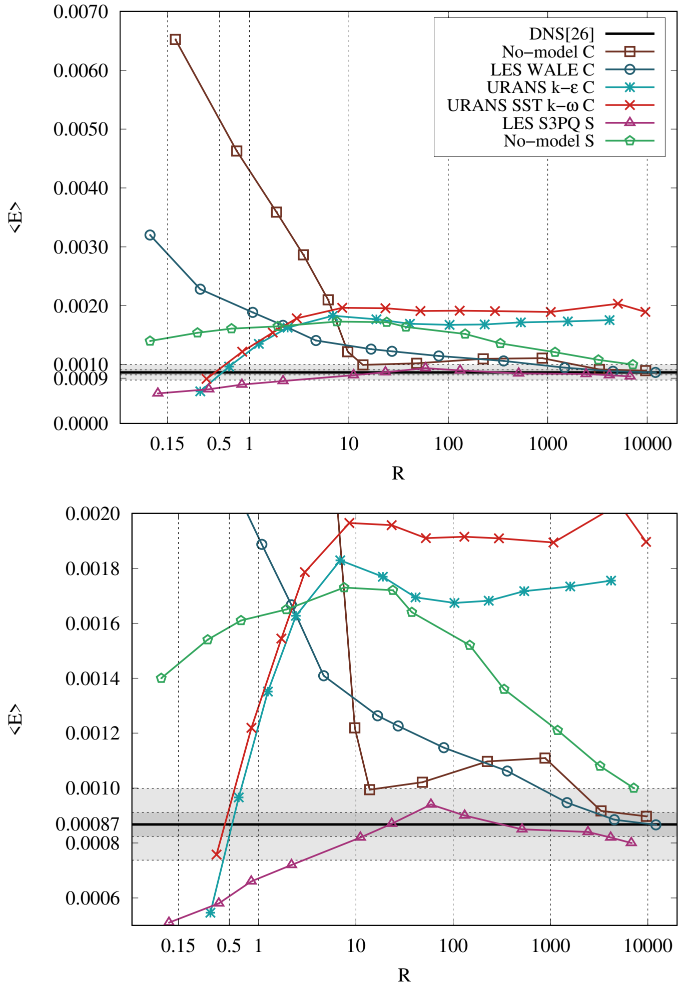

Figure 2.3: Test case 1. Steady-state analysis. Top: Average kinetic energy on different grid resolutions and turbulence models against time ratio. Bottom: Zoomed image of the graph at the top. Each point in the graph corresponds to a mesh from Table 2.1. "C" stands for collocated grid discretization and "S" - for staggered.

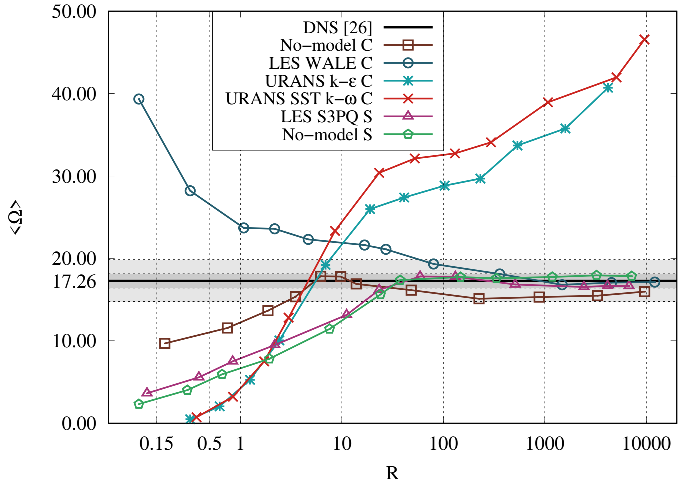

Figure 2.4: Test case 1. Steady-state analysis. Average enstrophy on different grid resolutions and turbulence models against time ratio. "C" stands for collocated grid discretization and "S" - for staggered.

2.4.2 Test case 2 - mixed convection. Results of the steady simulations

For this test case, we use three global quantities: the average temperature, the average kinetic energy, and the average enstrophy. We compare them against the DNS data (published in the data archive in [54]), obtained using the in-house STG code described in section 2.3.2. In this case, we use a fourth-order symmetry preserving discretization scheme [35].

Averaged temperature (Figure 2.5) is well predicted by all of the approaches. Even the coarsest meshes fall within a 15% error range and perform faster than real-time simulations. The temperature field appears to be relatively easy to predict since it is an integral quantity, which mostly depends on the energy balance.

Average kinetic energy (Figure 2.6, top) is more difficult to calculate correctly. Even though none of the models show very large errors, they are far from the DNS solution. The specific geometry of the test case makes the accurate resolution of the jet possible only with sufficiently fine spatial grid near the inlet area. Nonetheless, all the approaches show positive convergence tendency towards the reference value of kinetic energy. Enstrophy (Figure 2.6, bottom) is reasonably well predicted by the LES and no-model approaches, however, the computational speed is slower than real-time. URANS models show incorrect results, which could be explained by the nature of the turbulence modeling in URANS.

This test case is more difficult to be solved accurately due to the small aspect ratios of the inlet and outlet openings. Figure 2.7 features a snapshot from a video [54] of the DNS

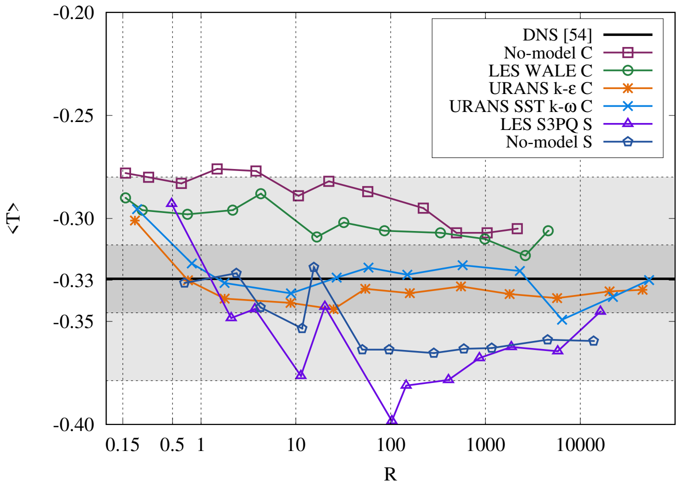

Figure 2.5: Test case 2. Steady-state analysis. Average temperature with different grid resolutions and turbulence models against time ratio. Each point in the graph corresponds to a mesh from Table 2.2. "C" stands for collocated grid discretization and "S" - for staggered.

simulations with different mesh resolutions. The quantity plotted in the snapshot is the velocity magnitude. It is seen in the figure how the mesh resolution affects the prediction of the jet shape. Results for the finest mesh show a well-defined jet, which separates from the ceiling near the right wall. As the mesh resolution decreases, the jet appears to look more distorted and the separation point moves away from the right wall.

As seen in the Figures 2.5-2.6, the no-model and LES approaches give similar results, but the no-model on staggered grids shows the best performance for the steady-state analysis. It reaches the desired accuracy of 15% and 5% with the time ratios of $R \approx 4$ and $R \approx 13810$, respectively. The least accurate predictions are provided by the URANS models. The average cavity temperature appears to be the easiest quantity to predict, while enstrophy is the most difficult one.

2.5 Results of the transient analysis

This section presents the analysis of the transient simulations of the same test cases. The purpose of the analysis is to study the feasibility of CFD for MPC of indoor air parameters. In MPC for buildings the prediction is usually made for the next 4-5 hours with the time step of 1-3 hours [22]. Therefore, for the worst-case scenario the CFD for MPC should be at least 6 times faster than real-time ($R \leq 1/6 \lesssim 0.15$). Transient simulations are re-scaled in the way

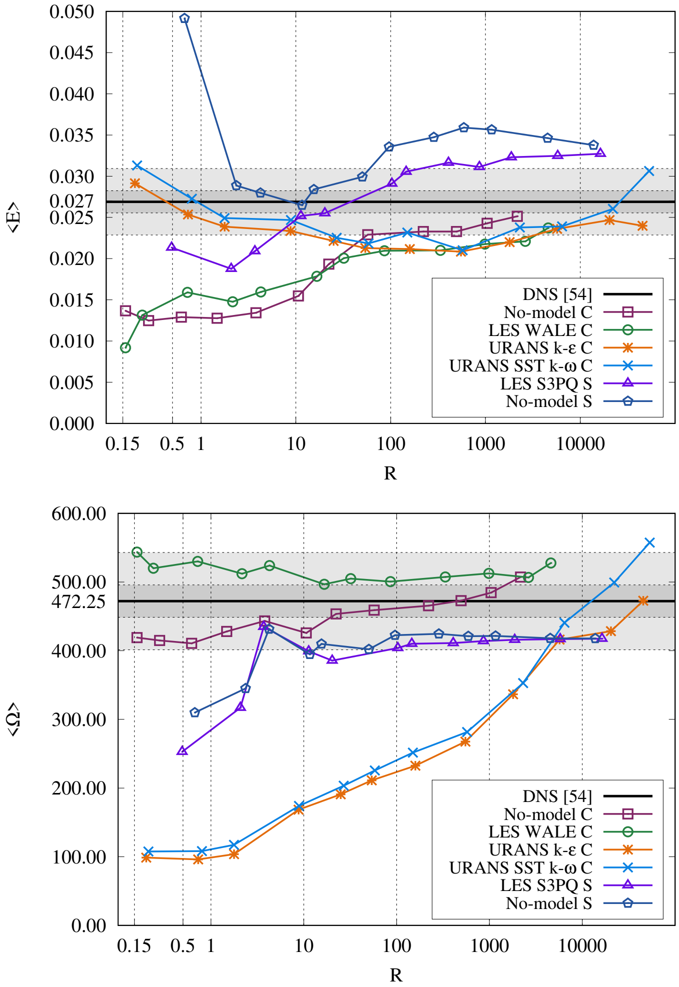

Figure 2.6: Test case 2. Steady-state analysis. Average kinetic energy (top) and average enstrophy (bottom) with different grid resolutions and turbulence models against time ratio. Each point in the graph corresponds to a mesh from Table 2.2. "C" stands for collocated grid discretization and "S" - for staggered.

described in Section 2.4. The same global quantities are considered in the transient analysis. The quality of transient simulations is studied by measuring the dynamic trend using root mean square error (RMSE) of the instantaneous values with respect to the DNS solution. The

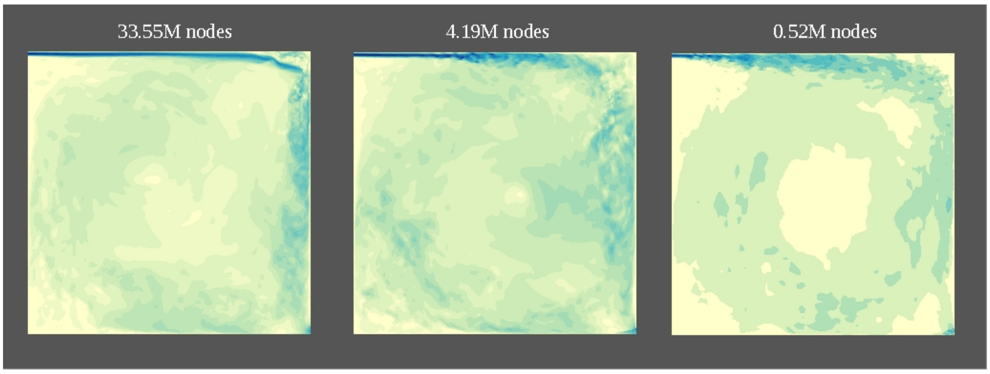

.

Figure 2.7: Snapshot from a video of the DNS simulations of the mixed convection case (test case 2). The plotted quantity is the velocity magnitude. The full video is available at [54]

values of the error are calculated as follows:

$$RMSE(\phi) = \frac{\sqrt{\int_{t_{ini}}^{t_{end}} (\phi - \phi_{DNS})^2 dt}}{\sqrt{\int_{t_{ini}}^{t_{end}} \phi_{DNS}^2 dt}}, \tag{2.11}$$

where t_{ini} and t_{end} are the beginning and the end of the time integration period respectively, ϕ is the variable of interest, ϕ_{DNS} its value obtained via the DNS simulation. In the next subsections, the results of the two test cases are discussed in detail using the methodology presented above.

2.5.1 Test case 1 - differentially heated cavity. Results of the transient simulations

For the differentially heated cavity case, three global quantities are considered: Nusselt number on the hot wall, kinetic energy, and enstrophy. Stratification was discarded because of its high fluctuations. Simulation results are compared to DNS results previously published in [26]. Time evolution of these quantities is shown in Figures 2.8-2.10 (top). Time evolution is plotted for mesh M1.8 (Table 2.1), as it is the coarsest mesh that provided the desired accuracy. In Figures 2.8-2.10 (bottom) the RMSE of these quantities are plotted against the computational time ratio R in logarithmic scale. Each point of the graph represents a mesh from Table 2.1. The dashed line separates the area within 15% error from the value of perfect correlation ($RMSE(\phi) = 0$).

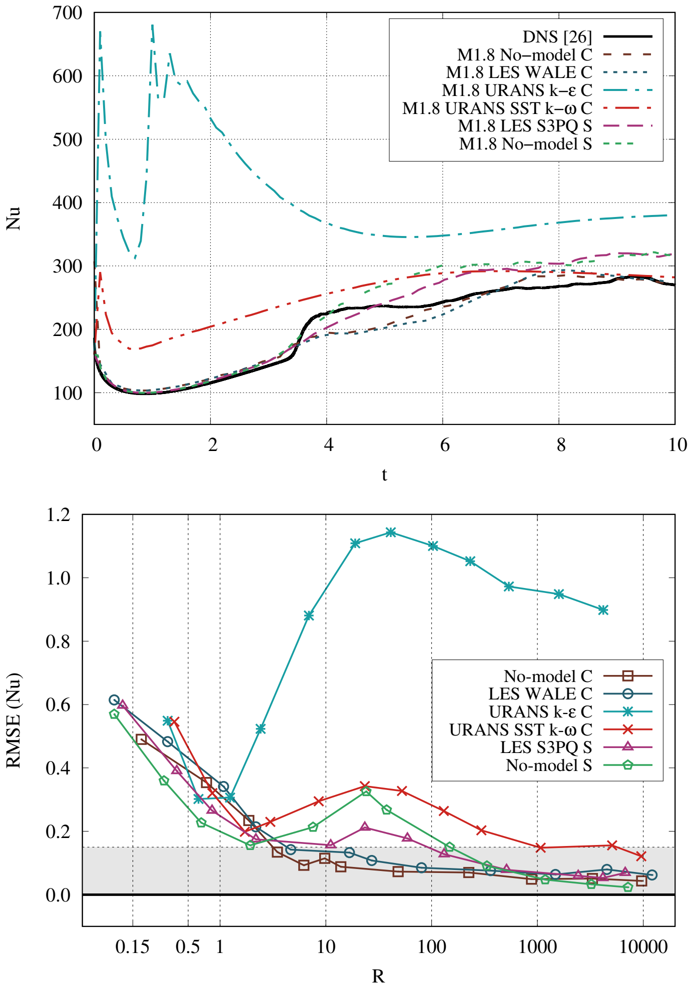

Figure 2.8: Test case 1. Top: Time evolution of the Nusselt number on the hot wall. Bottom: RMSE of the Nusselt number with different grids and turbulence models against time ratio. Each point in the bottom graph corresponds to a mesh from Table 2.1. "C" stands for collocated grid discretization and "S" - for staggered.

Nusselt number (Figure 2.8) is the fastest quantity to converge towards a steady-state. LES and no-model behave similarly to the reference. URANS $SSTk - \omega$ model also has acceptable dynamic trend. However, URANS $k - \epsilon$ model shows a negative correlation since its transient behavior is completely different from that of DNS.

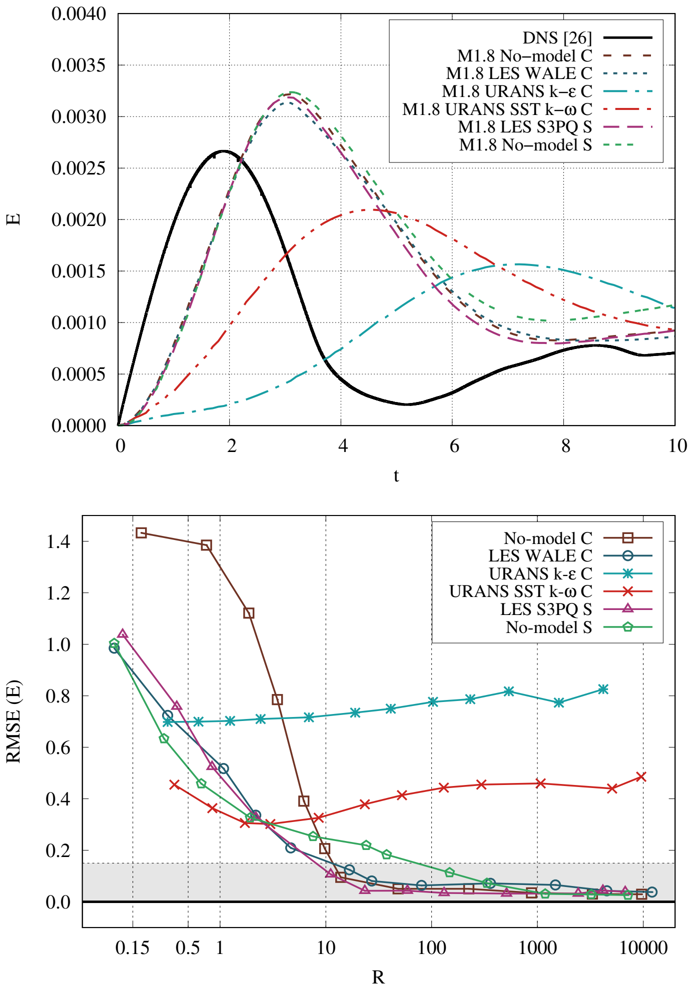

Figure 2.9: Test case 1. Top: Time evolution of the kinetic energy. Bottom: RMSE of the kinetic energy with different grids and turbulence models against time ratio. Each point in the bottom graph corresponds to a mesh from Table 2.1. “C” stands for collocated grid discretization and “S” - for staggered.

Reference kinetic energy (Figure 2.9) shows a good correlation tendency on LES and no-model approaches (both staggered and collocated discretizations). On the other hand, both URANS models again exhibit a negative tendency because of the late peak. Enstrophy (Figure 2.10) is showing behavior similar to kinetic energy. URANS results exhibit the peak later than the reference, and this gives low correlation values. LES and no-model approaches show good transient correlation.

For test case 1, the LES and no-model approaches give the best transient correlations, but the LES-S3PQ model on staggered grids has the lowest computational cost. Results for staggered and collocated approaches are very similar, but the staggered discretization has a better correlation at low mesh resolutions. LES and no-model approaches enter 15% error range at mesh resolution M1.8 of the Table 2.1 with the time ratio $R \approx 130$. The least accurate predictions are provided by the URANS models.

2.5.2 Test case 2 - mixed convection. Results of the transient simulations

For the transient analysis, three global quantities are considered: kinetic energy, enstrophy, and cavity temperature. Time evolution of these quantities is presented in Figures 2.11-2.13 (top) and their associated RMSE is plotted against time ratio R in Figures 2.11-2.13 (bottom). Again, the DNS simulation is used as a reference [54]. Time evolution is plotted for the mesh M2.12 (Table 2.2), as no other coarser mesh has reached the desired accuracy.

The mean cavity temperature (Figure 2.11) is predicted correctly even by very coarse meshes. Both LES and no-model approaches show the smooth convergence aligned with the DNS profile. Although URANS profiles look different from the reference, their prediction error is still within the acceptable margin. LES-S3PQ model on staggered grids has shown the best transient correlation.

The time evolution of kinetic energy for the mixed convection is more difficult to predict than temperature (Figure 2.12). The best prediction is given by LES-S3PQ and no-model methods on staggered grids. Collocated LES and no-model simulation show slower time convergence, and URANS convergence is too fast. For the kinetic energy of the mixed convection case, all six tested approaches show an acceptable transient correlation. Enstrophy (Figure 2.13) is a highly fluctuating quantity, and it is difficult to predict its transient evolution. The behavior of time evolution of the enstrophy is well predicted by LES and no-model simulations, meanwhile, the predictions of URANS are very inaccurate. URANS time evolution is smooth, while other approaches show multiple small peaks. This is demonstrated by the low values of the correlation coefficient for URANS models.

Even though this test case is less turbulent than the previous one, the complexity of the physics of the problem requires high mesh resolution, which explains the low accuracy of the obtained results. As could be concluded from the results, only the finest mesh M2.12 nears the required accuracy for the transient simulations. The no-model approach on staggered grids gives the lowest computational cost of $R \approx 13810$ at this mesh resolution.

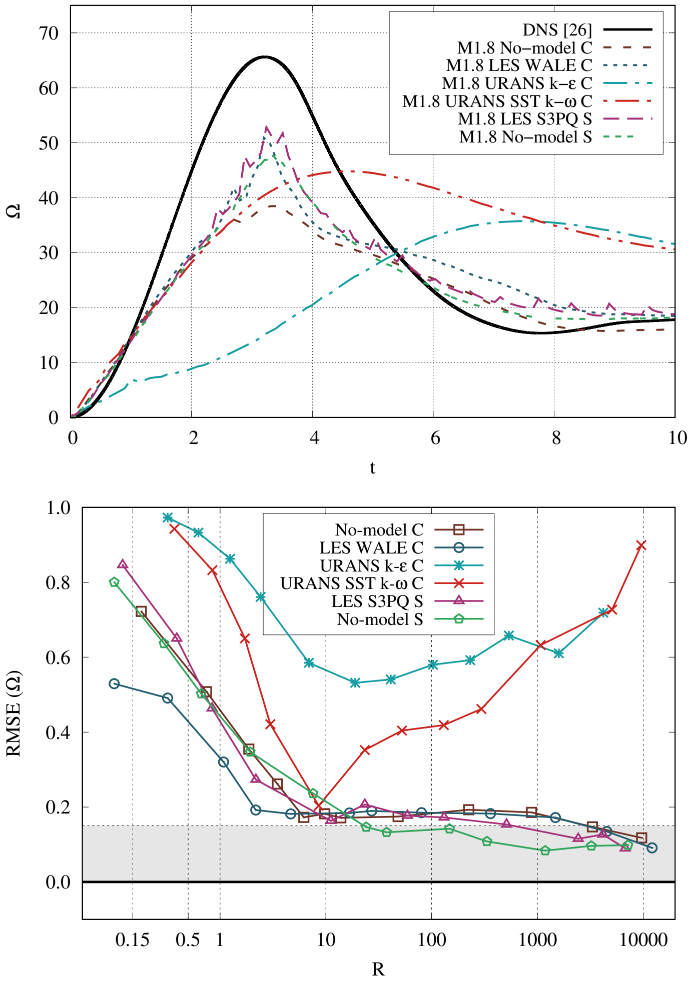

Figure 2.10: Test case 1. Top: Time evolution of the enstrophy. Bottom: RMSE of the enstrophy awith different grids and turbulence models against time ratio. Each point in the bottom graph corresponds to a mesh from Table 2.1. "C" stands for collocated grid discretization and "S" - for staggered.

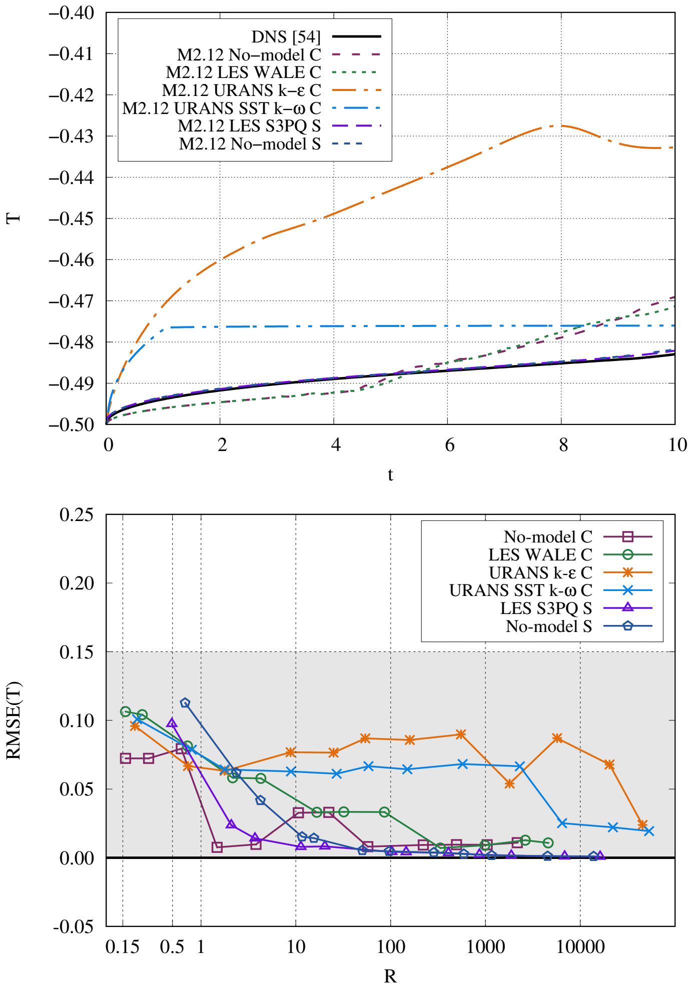

Figure 2.11: Test case 2. Top: Time evolution of the average cavity temperature. Bottom: RMSE of the average cavity temperature with different grids and turbulence models against time ratio. Each point in the bottom graph corresponds to a mesh from Table 2.2. ”C” stands for collocated grid discretization and ”S” - for staggered.

2.6 Summary of the obtained results

Results for both transient and steady simulations, for both test cases, are summarized in the Table 2.3. The Table shows computational time ratios for both test cases with all approaches

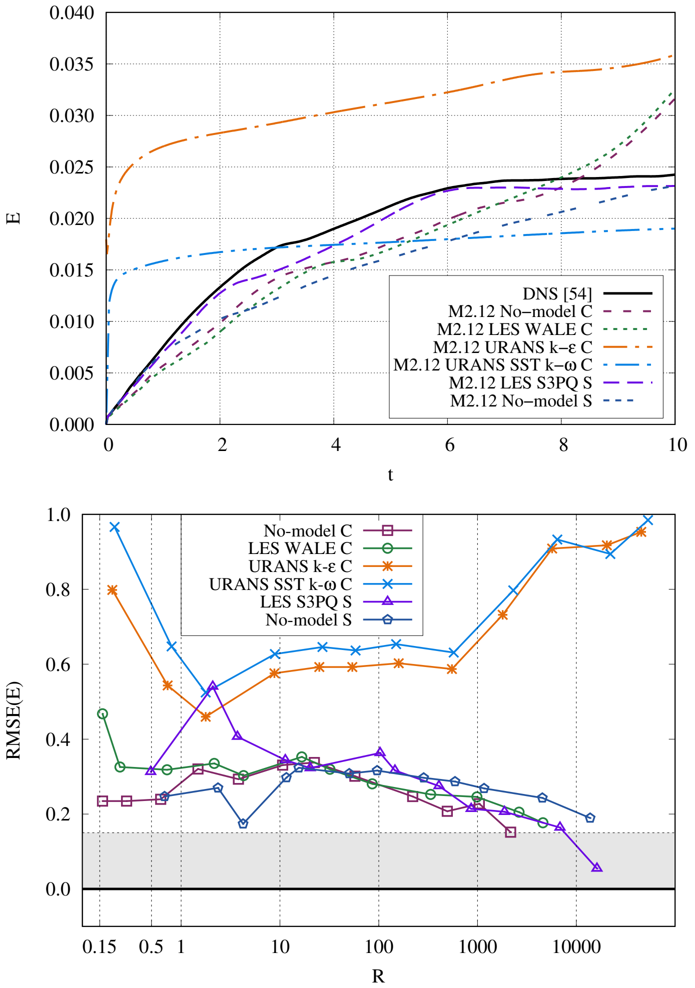

Figure 2.12: Test case 2. Top: Time evolution of the kinetic energy. Bottom: RMSE of the kinetic energy against time ratio. Labeling is the same as in figure 2.11.

used. The time ratios displayed in the table correspond to the coarsest meshes at which the desired accuracy for all the global quantities of interest is achieved. Since several assumptions are made while computing time ratios, their intervals are given instead of the exact values.

As seen in Table 2.3, required accuracy was not achieved by real-time or faster than real-time simulations, performed by any of the tested approaches for both transient and steady

Table 2.3: Computational time ratios R, obtained for the differentially heated cavity (test case 1) and the mixed convection (test case 2) for several indoor environmental applications and different turbulence models. "C" stands for collocated grid discretization and "S" - for staggered. The shadows of blue from light to dark show computational time ratios from low to high, respectively. The red cross stands for the insufficient accuracy.

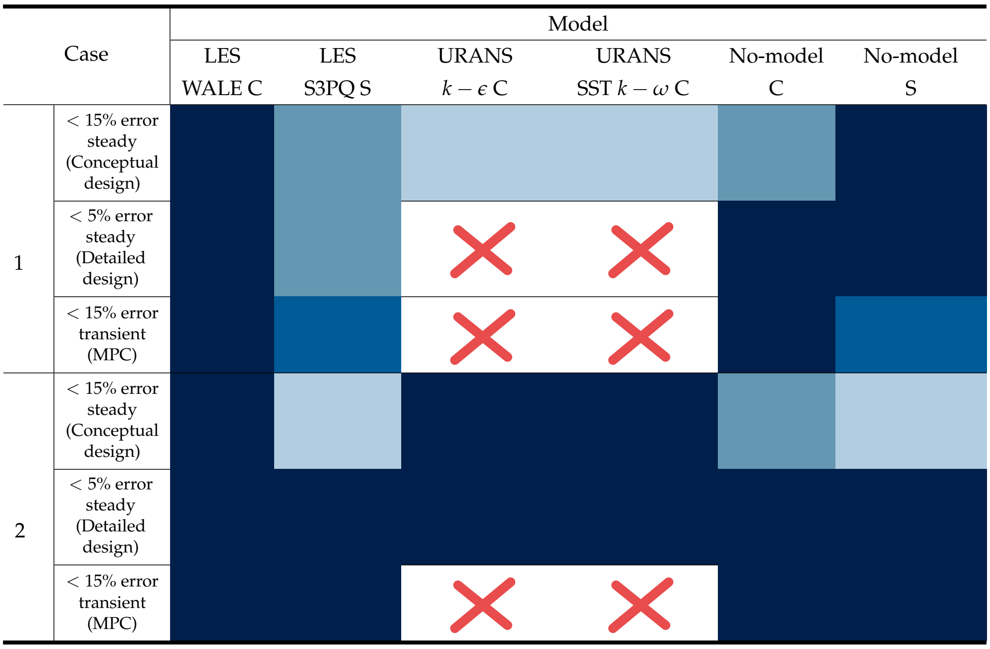

Case		Model					
		LES WALE C	LES S3PQ S	URANS $k-\epsilon$ C	URANS SST $k-\omega$ C	No-model C	No-model S
1	$<15\%$ error steady (Conceptual design)	█	▒	░	░	▒	█
	$<5\%$ error steady (Detailed design)	█	▒	✗	✗	█	█
	$<15\%$ error transient (MPC)	█	▓	✗	✗	█	▓
2	$<15\%$ error steady (Conceptual design)	█	░	█	█	▒	░
	$<5\%$ error steady (Detailed design)	█	█	█	█	█	█
	$<15\%$ error transient (MPC)	█	█	✗	✗	█	█

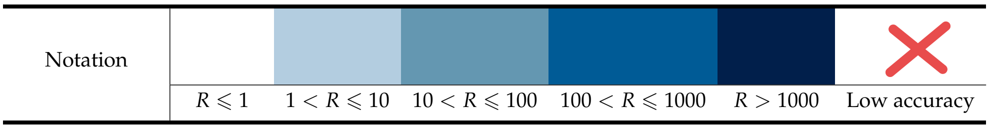

Notation		░	▒	▓	█	✗
	$R \leqslant 1$	$1 < R \leqslant 10$	$10 < R \leqslant 100$	$100 < R \leqslant 1000$	$R > 1000$	Low accuracy

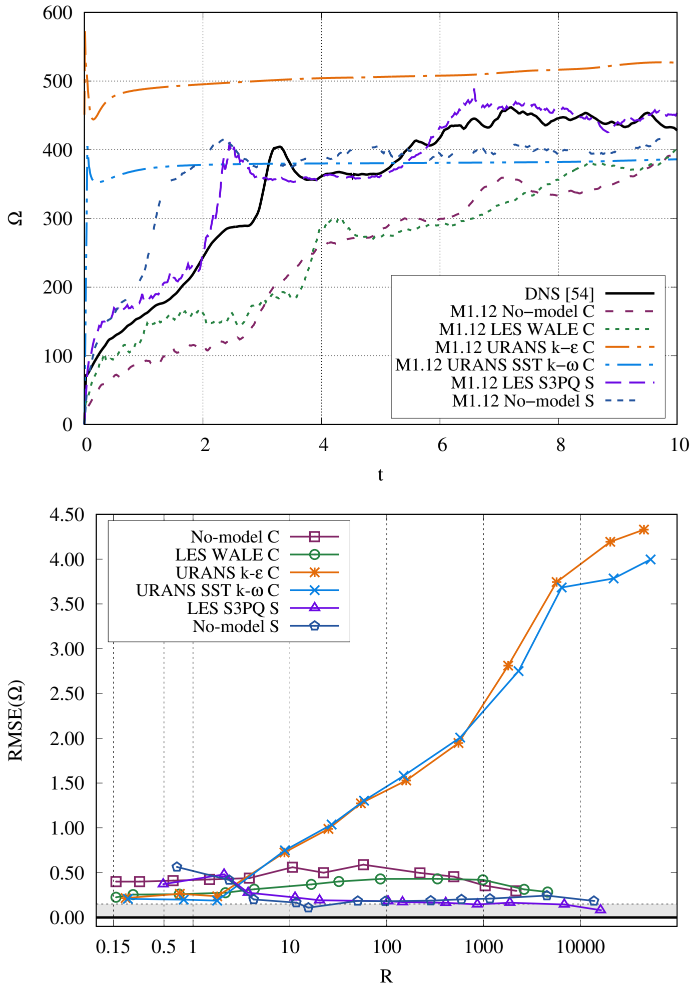

Figure 2.13: Test case 2. Top: Time evolution of the enstrophy. Bottom: RMSE of the enstrophy against time ratio. Labeling is the same as in figure 2.11.

simulations. Kinetic energy and enstrophy appear to be especially difficult to predict. Even though URANS simulations are the least computationally expensive, their accuracy is often insufficient. Moreover, URANS tends to converge to a solution different from the one provided by the DNS reference. This could be explained by the nature of the URANS models, as they are not suitable for the natural convection and mass separation flows because they have been developed mostly for aerodynamic applications, where boundary layers are usually attached or partially attached [48]. The no-model and LES simulations provide similar results, but the computational cost of the no-model approach is approximately 30% lower. Staggered symmetry-preserving discretization considerably improves the accuracy of the results for coarse and extremely coarse grids with the no-model approach. For the LES simulations, the effect of staggered discretization on the results is less notable.

2.7 Discussion

In this section, we present the interpretation of the obtained results by moving from the analyzed test cases to their real-life analogs (a generic closed system and a generic open system). We discuss the computational requirements for the indoor environmental simulations and the feasibility of these simulations.

2.7.1 Extrapolation to real-size problems

To perform the simulations, we adopted the conditions used in the experiments of Saury *et al.* [23] and Blay *et al.* [27] detailed in Section 2.2. However, these experimental domain sizes and temperature differences are not realistic for indoor environmental problems. The purpose of this section is to extrapolate the findings (in terms of simulation time and feasibility) to more realistic problems.

As an example of a closed system, we consider a building atrium exposed to an arbitrary summer temperature of $T_h = 27°C$ on one side and maintained at the constant temperature of an air-conditioned building of $T_c = 23°C$ ($\Delta T = 4°C$). Maintaining constant dimensionless Pr and Ra_H numbers of the differentially heated cavity, and constant air properties, the simulated domain size becomes equal to $1.71 \times 6.57 \times 1.47$ meters. The physical time of the simulation is proportional to the square of the domain size; thus, the time ratios for this case decrease by a factor of 2.93, compared to the simulated case.

According to the results presented in Figures 2.2 - 2.4 and 2.8 - 2.10 for the differentially-heated cavity test case, the minimal time ratios for conceptual design, detailed design and MPC are $R \approx 25$, $R \approx 60$ and $R \approx 130$, respectively. These are the minimal time ratios which reached the desired accuracy for all the global quantities (LES-S3PQ turbulence model on staggered grids). Using the aforementioned re-scaling factor, they become equal to $R \approx 10$, $R \approx 20$ and $R \approx 45$, respectively.

A similar procedure could be done for the second test case. We assume a room with the temperature difference of $\Delta T = 4°C$, constant inlet bulk velocity, and constant air properties. Maintaining constant dimensionless Pr, Ra_H and $Fr_{h_{in}}$ numbers, the new domain size becomes $1.78 \times 1.78 \times 0.51$ meters. Therefore, the physical time of the simulation is multiplied by a factor of 1.71 (proportional to the domain size). Thus the time ratios for conceptual design, detailed design and MPC are re-scaled from $R \approx 4$, $R \approx 13810$ and $R \approx 13810$ (no-model approach on staggered grids) to $R \approx 3$, $R \approx 8000$ and $R \approx 8000$, respectively.

Re-scaled domain sizes for both test cases are not far from the realistic ones, as a result, we conclude that the computational time of the test cases is of the same order of magnitude as of the real HVAC setups. Therefore, they could be used as an estimation for a generic closed system and generic open system, respectively.

2.7.2 Availability of steady-state simulations for design applications

We assume reasonable speed for both conceptual and detailed design applications as two times faster than real-time ($R \leqslant 0.5$). We accept the values of 15% relative error for the conceptual design and 5% for the detailed design. The minimal time ratios which reached the desired accuracy for all the global quantities, are $R \approx 10$ and $R \approx 20$ for the early and detailed design stages of the real-size closed system. On the other hand, the time ratios for a generic open system are $R \approx 3$ and $R \approx 8000$, respectively.

The obtained time ratios of the simulations are significantly higher than the required. The computational cost cannot be further reduced without sacrificing the essential accuracy. Results indicate that fast reliable CFD simulations on office computers are currently not available neither for detailed design nor conceptual design stages. Of course, a high-performance supercomputer can handle these simulations with required time ratio and accuracy. However, large computational resources are usually available only for particular high-end building designs, and not for routine use. Thus, it is interesting to analyze when fast and accurate CFD will be feasible on ordinary office computers.

The most well-known law of computational growth is Moore's law [55]. It states that the number of transistors in a dense integrated circuit would double in about every 18 months. We use it as an rough optimistic prediction. On the other hand, as we mentioned earlier, CFD applications are memory-bound. In other words, their performance depends mostly on the memory bandwidth of the processor. Thus, it is interesting to see how it grows. Yet, there is no law, which could predict the bandwidth growth rate. As an estimation, we derive the growth rate from the increase of the DDR SDRAM capacity between the years 1998 and 2020. Within these 22 years, the DDR SDRAM memory bandwidth has grown approximately 39 times bigger. As a rough pessimistic prediction, we estimate that the memory bandwidth will continue growing at the same rate in the future.

Figure 2.14 shows the estimated decreasing simulation time ratio due to the growing computational power over the years for different applications and different growth estimations for a generic closed system (top) and a generic open system (bottom). We extrapolate the possible future values of the time ratio using different prediction laws: solid line - the memory bandwidth growth rate, dashed line - Moore's law, the shadowed area between the lines - intermediate possibilities.

Results in Figure 2.14 significantly vary between optimistic and pessimistic predictions. According to optimistic prediction, the early design stage simulations will be possible in about 5 years. For the detailed design stage, the optimistic predictions go up to 10 years for a generic closed system and 20 years for a generic open system. Yet, pessimistic predictions have a very different waiting horizon. CFD for the early design stage simulations will be possible in 10-15 years. The guess for the detailed design stage is at least 25 years for a closed system and 60 years for an open one.

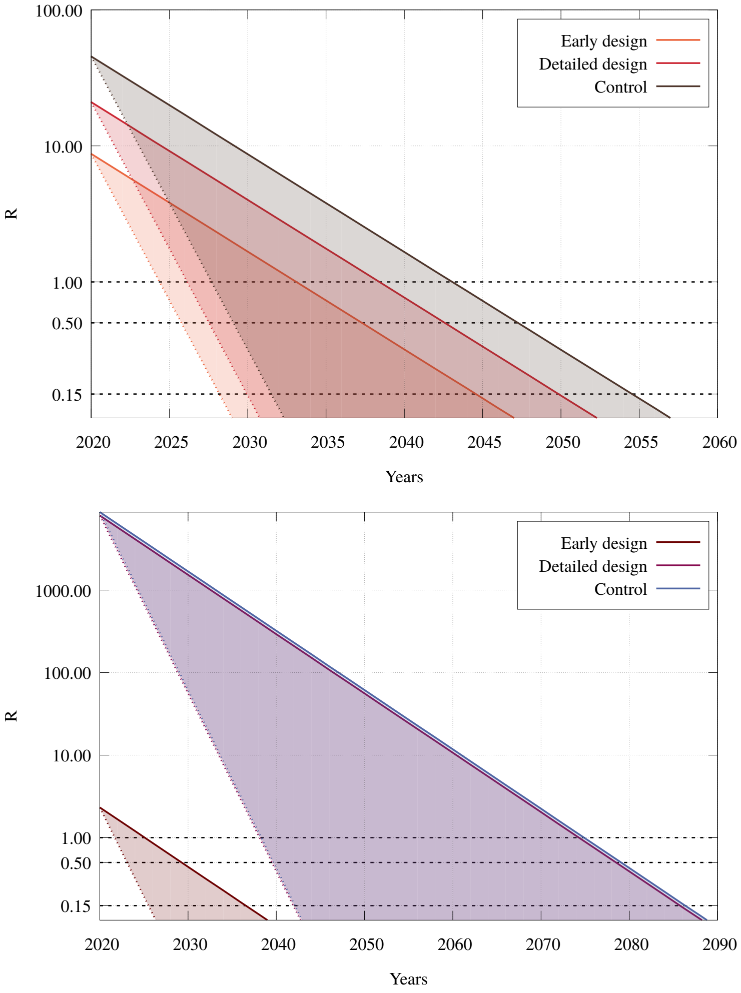

Figure 2.14: Potential of accessing affordable high-fidelity CFD over the next years. Top: estimation for a generic closed system. Bottom: estimation for a generic open system. The solid line is the memory bandwidth growth rate, and the dashed line is Moore's law growth rate, the shadowed area between the lines - intermediate possibilities.

2.7.3 Availability of transient simulations for MPC applications

As mentioned earlier, CFD for MPC should be at least 6 times faster than real-time ($R \lesssim 0.15$). The required simulation accuracy highly depends on the controlled building function. It could be assumed that a 15% error in the prediction of the transient evolution of global quantities is sufficient for civil building applications. The time ratio for a generic closed system is $R \approx 45$, which is the best trade-off between computational cost and accuracy. For open systems like the test case 2 (Figures 2.11 - 2.13), the obtained time ratio ($R \approx 8000$) is bigger due to the required high mesh resolution in the jet area.

With the current computational resources, it is not possible to incorporate CFD into the MPC system of a building. However, taking into account the aforementioned predictions of Moore's law [55] and the bandwidth growth rate, we estimate the time in which transient CFD applications would be available for MPC (Figure 2.14). The required mesh resolution and the computational resources for different test cases vary significantly. For a closed system based on the differentially heated cavity test case, a good temporal resolution with the required time ratio ($R \lesssim 0.15$) could be achieved within the next 10 years (optimistic prediction). However, an open system based on the mixed convection case needs a higher spatial resolution to perform correct transient simulations, which give us an optimistic prediction of at least 25 years. The pessimistic prediction is showing a very different expected availability - around 35 years for a closed system and around 70 years for an open system with a jet.

The difference between optimistic and pessimistic scenarios is drastic. However, now we can not completely adopt either of them. Probably, at a certain point in the future, a significant technological transformation might occur, which would match the bandwidth growth rate with Moore's law. Alternatively, with the growth of computational performance, more and more applications will become memory-bound, which would shift the further acceleration towards a pessimistic scenario.

2.8 Conclusions

This work studied the feasibility of affordable, fast, and high-fidelity CFD simulations for indoor environmental applications, considering two representative test cases and a wide range of numerical setups. We considered three possible building applications: conceptual design, detailed design, and MPC.

We tested LES, URANS, and no-model approaches with both staggered and collocated discretizations on a set of structured Cartesian non-uniform grids. LES and no-model approach showed considerably higher accuracy than URANS. Even though URANS simulations were the least computationally expensive, their accuracy was often insufficient. The no-model approach produces similar to LES results, but with the lower computational cost. Staggered symmetry-preserving discretization considerably improves the accuracy of coarse and extremely coarse grids.

Based on the obtained run-times of the simulations and the building applications requirements, we conclude that, fast high-fidelity CFD simulations on the office computers are not feasible neither for design nor for control of indoor environments. Obtained run-times are too long to make CFD a primary tool for HVAC applications. We estimated the growth of computational resources in the future to determine when CFD would be available for routine use on office computers. The optimistic prediction estimates that CFD would be feasible for conceptual design in 5 years, for the detailed design in 10-20 years, and in 10-25 years for MPC. The pessimistic prediction anticipates at least 15 years for the conceptual design, 25 years for the detailed design, and 35 years for control.

References

[1] X. Cao, X. Dai, and J. Liu. Building energy-consumption status worldwide and the state-of-the-art technologies for zero-energy buildings during the past decade. *Energy and Buildings*, 128:198–213, 2016.

[2] J. Axley. Multizone airflow modeling in buildings: History and theory. *HVAC&R Research*, 13(6):907–928, 2007.

[3] A. C. Megri and H. Fariborz. Zonal modeling for simulating indoor environment of buildings: Review, recent developments, and applications. *HVAC&R Research*, 13(6):887–905, 2007.

[4] Y. Li and P. V. Nielsen. Commemorating 20 years of Indoor Air: CFD and ventilation research. *Indoor Air*, 21(6):442–453, 2011.

[5] T. van Hooff, B. Blocken, and Y. Tominaga. On the accuracy of CFD simulations of cross-ventilation flows for a generic isolated building: Comparison of RANS, LES and experiments. *Building and Environment*, 114:148–165, 2017.

[6] W. Chen, S. Liu, Y. Gao, H. Zhang, E. Arens, L. Zhao, and J. Liu. Experimental and numerical investigations of indoor air movement distribution with an office ceiling fan. *Building and Environment*, 130:14–26, 2018.

[7] Z. Chen, J. Xin, and P. Liu. Air quality and thermal comfort analysis of kitchen environment with CFD simulation and experimental calibration. *Building and Environment*, 172:106691, 2020.

[8] E. Katramiz, D. Al Assaad, N. Ghaddar, and K. Ghali. The effect of human breathing on the effectiveness of intermittent personalized ventilation coupled with mixing ventilation. *Building and Environment*, 174:106755, 2020.

[9] X. Zheng, H. Montazeri, and B. Blocken. CFD simulations of wind flow and mean surface pressure for buildings with balconies: Comparison of RANS and LES. *Building and Environment*, 173:106747, 2020.

[10] H. Wang and Z. Zhai. Application of coarse-grid computational fluid dynamics on indoor environment modeling: Optimizing the trade-off between grid resolution and simulation accuracy. *HVAC&R Research*, 18(5):915–933, 2012.

[11] T. Kempe and A. Hantsch. Large-eddy simulation of indoor air flow using an efficient finite-volume method. *Building and Environment*, 115:291–305, 2017.

[12] F. Kuznik, C. Obrecht, G. Rusaouen, and J. J. Roux. LBM based flow simulation using GPU computing processor. *Computers & Mathematics with Applications*, 59(7):2380–2392, 2010.

[13] B. Elhadidi and H. E. Khalifa. Comparison of coarse grid lattice Boltzmann and Navier Stokes for real time flow simulations in rooms. *Building Simulation*, 6:183–194, 2013.

[14] M. A. I. Khan, N. Delbosc, C. J. Noakes, and J. Summers. Real-time flow simulation of indoor environments using lattice Boltzmann method. *Building Simulation*, 8:405–414, 2015.

[15] J. Stam. Stable fluids. In *Proceedings of the 26th Annual Conference on Computer Graphics and Interactive Techniques*, pages 121–128, 1999.

[16] W Zuo and Q. Chen. Real-time or faster-than-real-time simulation of airflow in buildings. *Indoor Air*, 19(1):33–44, 2009.

[17] F. Oldewurtel, A. Parisio, C. N. Jones, D. Gyalistras, M. Gwerder, V. Stauch, B. Lehmann, and M. Morari. Use of model predictive control and weather forecasts for energy efficient building climate control. *Energy and Buildings*, 45:15–27, 2012.

[18] S. Yang, M. P. Wan, W. Chen, B. F. Ng, and D. Zhai. An adaptive robust model predictive control for indoor climate optimization and uncertainties handling in buildings. *Building and Environment*, 163:106326, 2019.

[19] J. Zhuang, Y. Chen, and X. Chen. A new simplified modeling method for model predictive control in a medium-sized commercial building: A case study. *Building and Environment*, 127:1–12, 2018.

[20] T. Zerihun Desta, K. Janssens, A. Van Brecht, J. Meyers, M. Baelmans, and D. Berckmans. CFD for model-based controller development. *Building and Environment*, 39(6):621–633, 2004.

[21] X. Zhou, H. Li, Y. C. Soh, and C. Jiang. Development of a novel strategy of CFD-based model predictive control. *Procedia Engineering*, 214:69–75, 2017.

[22] A. Afram and F. Janabi-Sharifi. Theory and applications of HVAC control systems - A review of model predictive control (MPC). *Building and Environment*, 72:343–355, 2014.

[23] D. Saury, N. Rouger, F. Djanna, and F. Penot. Natural convection in an air-filled cavity: Experimental results at large Rayleigh numbers. *International Communications in Heat and Mass Transfer*, 38(6):679–687, 2011.

[24] A. Sergent, P. Joubert, S. Xin, and P. Le Quéré. Resolving the stratification discrepancy of turbulent natural convection in differentially heated air-filled cavities Part II: End walls effects using large eddy simulation. *International Journal of Heat and Fluid Flow*, 39:15–27, 2013.

[25] J. Salat, S. Xin, P. Joubert, A. Sergent, F. Penot, and P. Le Quéré. Experimental and numerical investigation of turbulent natural convection in a large air-filled cavity. *International Journal of Heat and Fluid Flow*, 25(5):824–832, 2004.

[26] X. Álvarez, A. Gorobets, F. X. Trias, R. Borrell, and G. Oyarzun. HPC^2 âa fully-portable, algebra-based framework for heterogeneous computing. application to cfd. *Computers and Fluids*, 173:285–292, 2018.

[27] D. Blay, S. Mergui, J. L. Tuhault, and F. Penot. Experimental turbulent mixed convection created by confined buoyant wall jets. In *Proceedings of the First European Heat Transfer Conference, UK*, pages 821–828, 1992.

[28] R. Ezzouhri, P. Joubert, F. Penot, and S. Mergui. Large eddy simulation of turbulent mixed convection in a 3D ventilated cavity: Comparison with existing data. *International Journal of Thermal Sciences*, 48(11):2017–2024, 2009.

[29] The OpenFOAM Foundation. OpenFOAM. `https://www.openfoam.org/`, 2022.

[30] Termo Fluids S.L. Termofluids. `http://www.termofluids.com/`, 2022.

[31] F. X. Trias, O. Lehmkuhl, A. Oliva, C. D. Pérez-Segarra, and R. W. C. P. Verstappen. Symmetry-preserving discretization of Navier-Stokes equations on collocated unstructured grids. *Journal of Computational Physics*, 258:246–267, 2014.

[32] F. X. Trias and O. Lehmkuhl. A self-adaptive strategy for the time integration of Navier-Stokes equations. *Numerical Heat Transfer, Part B: Fundamentals*, 60(2):116–134, 2011.

[33] A. Gorobets, F. X. Trias, M. Soria, and A. Oliva. A scalable parallel Poisson solver for three-dimensional problems with one periodic direction. *Computers & Fluids*, 39(3):525–538, 2010.

[34] F. X. Trias, M. Soria, A. Oliva, and C. D. Pérez-Segarra. Direct numerical simulations of two- and three-dimensional turbulent natural convection flows in a differentially heated cavity of aspect ratio 4. *Journal of Fluid Mechanics*, 586:259–293, 2007.

[35] R. W. C. P. Verstappen and A. E. P. Veldman. Symmetry-preserving discretization of turbulent flow. *Journal of Computational Physics*, 187(1):343–368, 2003.

[36] N. Morozova, R. Capdevila, F. X. Trias, and A. Oliva. Towards real-time CFD simulation of indoor environment. In *Proceedings of 10th International Conference on Computational Fluid Dynamics*, July 9-13, 2018.

[37] Z. Zhang, W. Zhang, Z. J. Zhai, and Q. Y. Chen. Evaluation of various turbulence models in predicting airflow and turbulence in enclosed environments by CFD: Part-2: Comparison with experimental data from literature. *HVAC&R Research*, 13(6):871–886, 2007.

[38] N. Morozova, R. Capdevila, F. X. Trias, and A. Oliva. On the feasibility of CFD for transient airflow simulations in buildings. In *Proceedings of Building Simulation 2019: 16th Conference of IBPSA*, September 2-4, 2019.

[39] B. Mikuž and I. Tiselj. URANS prediction of flow fluctuations in rod bundle with split-type spacer grid. *International Journal of Heat and Fluid Flow*, 64:10–22, 2017.

[40] B. E. Launder and D. B. Spalding. The numerical computation of turbulent flows. *Computer Methods in Applied Mechanics and Engineering*, 3(2):269–289, 1974.

[41] V. Yakhot and S. A. Orszag. Renormalization-group analysis of turbulence. *Physical Review Letters*, 57(14):1722–1724, 1986.

[42] F. R. Menter. Two-equation eddy-viscosity turbulence models for engineering applications. *AIAA Journal*, 32(8):1598–1605, 1994.

[43] N. Morozova, F. X. Trias, R. Capdevila, C. D. Pérez-Segarra, and A. Oliva. Supplementary material for the journal paper ”On the feasibility of CFD simulations for indoor environment design and control”. `http://www.cttc.upc.edu/downloads/DHC-MC-diffTurbModels/`, 2020.

[44] F. Nicoud and F. Ducros. Subgrid-scale stress modelling based on the square of the velocity gradient tensor. *Flow, Turbulence and Combustion*, 62:183–200, 1999.

[45] L. Bricteux, M. Duponcheel, and G. Winckelmans. A multiscale subgrid model for both free vortex flows and wall-bounded flows. *Physics of Fluids*, 21, 2009.

[46] R. W. C. P. Verstappen. When does eddy viscosity damp subfilter scales sufficiently? *Journal of Scientific Computing*, 49(1):94–110, 2011.

[47] F. X. Trias, D. Folch, A. Gorobets, and A. Oliva. Building proper invariants for eddy-viscosity subgrid-scale models. *Physics of Fluids*, 27(6), 2015.

[48] S.B. Pope. *Turbulent flows*. Cambridge University Press, 2000.

[49] E. M. J. Komen, E. M. A. Frederix, T. H.J. Coppen, V. D'Alessandro, and J. G. M. Kuerten. Analysis of the numerical dissipation rate of different RungeâKutta and velocity interpolation methods in an unstructured collocated finite volume method in OpenFOAM®. *Computer Physics Communications*, 253:107145, 2020.

[50] J. Dongarra, M. A. Heroux, and Luszczek P. High-performance conjugate-gradient benchmark: A new metric for ranking high-performance computing systems. *The International Journal of High Performance Computing Applications*, 30(1):3–10, 2015.

[51] Ergonomics of the thermal environment â Analytical determination and interpretation of thermal comfort using calculation of the PMV and PPD indices and local thermal comfort criteria. Standard, International Organization for Standardization, Geneva, CH, 2005.

[52] F. Ferracuti, A. Fonti, L. Ciabattoni, S. Pizzuti, A. Arteconi, L. Helsen, and G. Comodi. Data-driven models for short-term thermal behaviour prediction in real buildings. *Applied Energy*, 204:1375–1387, 2017.

[53] O. Neu, S. Oxizidis, D. Flynn, F. Pallonetto, and D. Finn. High resolution space - time data: Methodology for residential building simulation modelling. In *Proceedings of 13th Conference of International Building Performance Simulation Association*, pages 2428–2435, August 26-28 2013.

[54] N. Morozova, F. X. Trias, R. Capdevila, and A. Oliva. Results from a turbulent air-filled $(Pr = 0.71)$ mixed convection at $Ra = 2.4 \times 10^9$ and $Fr = 5.24$ (both based on the inlet height). `http://www.cttc.upc.edu/downloads/MC_RA2_4e9_FR5_24/`, 2020.

[55] G. E. Moore. Cramming more components onto integrated circuits. *Proceedings of the IEEE*, 86(1):82–85, 1998.

3

A CFD-based surrogate model for predicting flow parameters in a ventilated room using sensor readings

Main content of this chapter has been published in:

N. Morozova, F.X. Trias, R. Capdevila, E. Schillaci and A. Oliva. A CFD-based surrogate model for predicting flow parameters in a ventilated room using sensor readings. *Energy and Buildings* **266**:112146, 2022.

Abstract: In this work, we develop a computational fluid dynamics (CFD)-based surrogate model, which predicts flow parameters under different geometrical configurations and boundary conditions in a benchmark case of a mechanically ventilated room with mixed convection. The model inputs are the temperature and velocity values in different locations, which act as a surrogate of the sensor readings. The model's output is a set of comfort-related flow parameters, such as the average Nusselt number on the hot wall, jet separation point, average kinetic energy, average enstrophy, and average temperature. We tested four different machine learning methods, among which we chose the gradient boosting regression due to its accurate performance. We also adapted the developed model for indoor environment control applications by determining the optimal combinations of sensor positions which minimize the prediction error. This model does not require the repetition of CFD simulations in order to be applied since the structure of the input data imitates sensor readings. Furthermore, the low computational cost of model execution and good accuracy makes it an effective alternative to CFD for applications where rapid predictions of complex flow configurations are required, such as model predictive control.

3.1 Introduction

The quality of the indoor environment is an important issue in our daily life, as we spend most of our time indoors. The quality of the indoor environment mostly depends on proper design and precise control of ventilation systems, which require knowledge of indoor air dynamics. Building air dynamics is usually a nonlinear, transient process, which depends on many factors such as weather, building geometry, occupants' behavior, etc. Thus, indoor air distribution usually involves various complex physical phenomena, such as natural and forced convection. As a result, the task of precise prediction of indoor air parameters is not straightforward.

Computational fluid dynamics (CFD) is a very powerful tool for evaluating indoor air distribution. In CFD, the physical domain is divided into a finite number of control volumes to solve the Navier-Stokes equations numerically. The solution provides a complete set of air parameters for each control volume. However, despite the sustained growth in computational power and advances in numerical algorithms, accurate CFD simulations are still prohibitively expensive [1] for most of the practical building applications and are mainly used for research and particular high-end buildings. The usual alternatives to CFD are the multizone [2] and zonal models [3], which can provide very rapid predictions but offer limited information due to the assumptions required. Moreover, the growth of computational resources in the foreseeable future would not be enough to make CFD available for routine use in building applications [1]. As a result, new numerical models capable of providing accuracy comparable with high-fidelity CFD but at considerably lower computational cost are needed.

Over the last years, several attempts to develop an alternative to zonal and multizone reduced-order models for building simulations have been made. For example, Li *et al.* [4] investigated a multiple model approach for predictive control of indoor thermal environment using proper orthogonal decomposition (POD). Phan *et al.* [5] developed a reduced-order model of a data center with multi-parameters using the POD method. Wang *et al.* [6] used CFD-based POD model to optimize air supply schemes in indoor environments. These models successfully reduce the simulation time while maintaining an acceptable level of accuracy. However, these works focus on temperature and thermal load predictions and do not consider motion-related flow parameters, which are usually more complex as they are described by nonlinear processes. Zuo & Chen [7] applied fast fluid dynamics (FFD) [8] method for indoor environmental simulations. They have successfully reduced the computing cost compared to CFD but at the expense of a considerably lower accuracy.

Data-driven models (DDMs) are steadily gaining popularity in building modeling applications due to their accurate approximations of nonlinear processes. They are used as surrogate models for building design, sensitivity and uncertainty analysis, thermal load predictions, and model predictive control (MPC) [9]. For instance, DDM-MPC for heating, ventilation, and air conditioning (HVAC) systems were developed for a university building [10], an airport [11], and a residential building [12,13]. DDMs for thermal load prediction were developed for a single building [14] and for a non-residential district [15]. On the other hand, Park & Park [16] performed a comparative analysis on the predictability of natural ventilation rates. However, these models are not based on CFD simulations and rely on reduced-order models, experimental results, or historical data to generate the database for their DDMs.

Using CFD simulations for surrogate modeling usually results in the high computational cost of dataset generation, yet a considerable number of researchers use this approach [17]. For example, Athavale *et al.* [18], and Fang *et al.* [19] compared different CFD-based DDSM approaches for temperature prediction in data centers and concluded that results produced by these models are in good agreement with the reference CFD data. Warey *et al.* [20] created an accurate model of vehicle cabin thermal comfort prediction using machine learning (ML) algorithms and high-fidelity CFD simulation results. The models mentioned above are of practical significance. Nevertheless, they are developed for specific applications and cannot be directly used to predict flow parameters in a more generic indoor environment. Zhou & Ooka [21] studied the influence of data preprocessing on DDM performance for reproducing CFD simulations of indoor airflow distribution and concluded that without data preprocessing, DDMs are likely to result in poor predictions. However, the objective of their work was not to reduce the simulation cost by using surrogate modeling. On the other hand, Lamberti & Gorlé [22] tackled the problem of the high computational cost of CFD database generation by combining low and high fidelity CFD simulations in an ML model to predict wind loads on buildings. Tian *et al.* [23] used ML to model indoor environment indicators in the stratified environments. All the researchers mentioned above note that DDMs produce accurate predictions at a low computational cost and could be an alternative to classical modeling techniques.

DDMs are based on using data analysis to find relations between system state variables without explicit knowledge of the physical behavior of the system. They can be developed relatively easily since they do not require an understanding of system physics. A comprehensive set of the high-quality input-output dataset is needed to train these models for all possible working conditions. The accuracy of DDMs decreases when training data deviates from testing data. Therefore, it is critical to use training data covering all the operating conditions, which could be challenging. However, difficulties in obtaining high-fidelity training data are compensated by the high accuracy and the low computational cost of the resulting model [12]. Therefore, DDMs could be used for complex indoor environments with stratification, natural, and forced convection, where multizone and zonal reduced-order models cannot be relied on, and computationally expensive CFD simulations are required.

In this work, we develop a data-driven surrogate model (DDSM), which is based on the data from CFD simulations. The model predicts comfort-related airflow parameters in a ventilated room with a heated floor, which is a classical benchmark test case used by many researchers in the field of indoor environmental simulations [24–27] for testing of novel simulation methods. We have chosen this test configuration because of the challenges it presents (the mixture of natural and forced convection) and because of the availability of both experimental [28] and direct numerical simulation (DNS) CFD [1] data for validation. Our work aims to develop a model which acts as a proof of concept. The main focus of our research is on investigating the capabilities and limitations of this model as a fast and robust alternative to CFD, taking into account specific requirements for indoor environmental applications. We begin with testing different ML methods to choose the approach that best fits our model specifics. After selecting the appropriate ML method, we optimize our DDSM to accommodate the requirements of indoor environment design and control applications. The optimization consists of two steps. First, we change the structure of the input data so that it takes the values of temperature and velocity in the locations, which in a practical case could be replaced by sensor readings. Then we test different combinations of input probe positions in order to find the optimal sensor placement.

The content of this paper is organized as follows: Section 3.2 describes the governing equations, details of the test case, and the database generation; Section 3.3 describes the numerical details of the CFD simulations and ML methods used in this study; Section 3.4 shows the results of the comparison of different DDSMs and the analysis of the optimal thermostat placement; Section 3.5 provides a discussion on model advantages and disadvantages; and Section 3.6 contains concluding remarks.

3.2 Physical problem and dataset generation

This section describes the physical details of the simulated test case, the governing equations of the flow, and the details of the generated dataset.

3.2.1 Governing equations

We use the incompressible Navier-Stokes equations for a Newtonian fluid with constant physical properties. We adopt the Boussinesq approximation to account for the density variations due to temperature differences. Thermal radiation is neglected. Under these assumptions, the governing equations are

$$\nabla \cdot \mathbf{u} = 0, \tag{3.1}$$

$$\frac{\partial \mathbf{u}}{\partial t} + (\mathbf{u} \cdot \nabla)\mathbf{u} = \nu \nabla^2 \mathbf{u} - \nabla p + \beta \mathbf{g} \Delta T, \tag{3.2}$$

$$\frac{\partial T}{\partial t} + (\mathbf{u} \cdot \nabla) T = \alpha \nabla^2 T, \tag{3.3}$$

where $\mathbf{u} = (u, v, w)$ is the velocity vector in Cartesian coordinates $\mathbf{x} = (x, y, z)$, p the kinematic pressure, T the temperature, ν the kinematic viscosity, $\mathbf{g}$ the gravitational acceleration, β the thermal expansion coefficient and α the thermal diffusivity.

Hereafter, all the results are presented in dimensionless form. The reference values of time, velocity, temperature, and length are $t_{ref} = H/U_{ref}$, $U_{ref} = U_{in}$, ΔT, and H, respectively, where H is the cavity height, U_{in} is the inlet bulk velocity, $\Delta T = T_h - T_c$ is the temperature difference, T_h is the temperature of the hot wall, and T_c is the temperature of the cold wall.

3.2.2 Physical problem

The physical setup used in this work is a classical benchmark case of a three-dimensional ventilated cavity with a heated floor. This configuration was first studied experimentally by Blay *et al.* [28]. In our previous work [1] we conducted high-fidelity DNS simulations of this benchmark case in order to validate our CFD results. This flow configuration presents a mixed convection phenomenon, challenging due to the interaction of both natural and forced convection. It resembles an airflow in a middle section of a room with mixing ventilation and thermal exhausts. The geometry of the studied cavity is shown in Figure 3.1 (left). Cold air at $T_c = -0.5$ enters the cavity through the long thin inlet at the top of the left wall. The inlet velocity profile in the vertical (y) direction corresponds to a parabolic Poiseuille flow. The inlet slot has an aspect ratio $A_{in} = h_{in}/H = 0.018/1.04$. The air is discharged through the outlet slot with the aspect ratio $A_{out} = h_{out}/H = 0.024/1.04$ at the bottom of the right wall of the cavity. The bottom wall is maintained at a hot temperature of T_h, while the three other sidewalls are kept at the cold temperature of T_c.

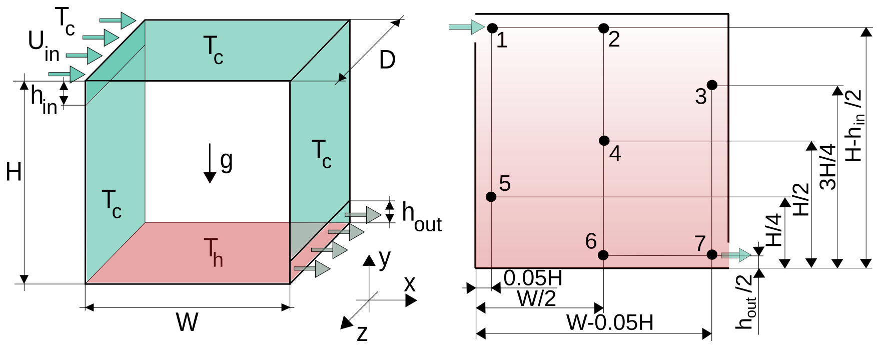

Figure 3.1: Left: geometry of the studied test case. Right: locations of the input data probes at the mid-depth cavity plane ($z = D/2$).

The cavity is filled with air ($Pr = \nu/\alpha = 0.71$). The depth aspect ratio of the cavity is $A_d = D/H = 0.3/1.04$. At the outlet, convective boundary conditions ($\partial\phi/\partial t + U_{in}\partial\phi/\partial x = 0$) are imposed for the velocity and temperature. No-slip boundary conditions are applied on the walls. The initial velocity field is set to zero and the initial temperature is set equal to the temperature at the cold wall. Periodic boundary conditions are used in the spanwise (z) direction.

3.2.3 Dataset generation

We build the input-output dataset by changing the width aspect ratio of the cavity ($A_w = W/H$), the Rayleigh number based on the cavity height $Ra_H = g\beta\Delta T H^3/(\nu\alpha)$, and the Froude number based on the ratio between the bulk inlet and buoyant velocity ($Fr = U_{in}/U_{buo} = Re_H/\sqrt{Ra_H}$, $Re_H = U_{in}H/\nu$ is the Reynolds number based on the cavity height). Test case configurations used in the generation of the dataset are shown in Table 4.1.

Chosen combinations of $A_w - Ra_H - Fr$ are realistic and relevant for indoor environmental applications. For example, assuming that the cavity height is 2.5 meters, the highest Rayleigh number (9.6×10^9) corresponds to a temperature difference of approximately $6°C$. On the other hand, the maximum Reynolds number based on the cavity height used in this work is 9.79×10^5. Considering the same height of 2.5 meters, it corresponds to an inlet velocity of $\approx 0.94 m/s$.

Table 3.1: Combinations of the test case configurations for generating the CFD dataset. "CG" stands for coarse-grid "FG" for fine-grid CFD simulations. Each combination for A_w and Ra_H is tested for all of the 20 Fr numbers listed in the table.

A_w	Ra_H			
	1.5×10^8	6×10^8	2.4×10^9	9.6×10^9
0.25	FG	FG	FG	CG
0.50	FG	FG	FG	CG
1.00	FG	FG	FG	CG
2.00	FG	FG	FG	-
4.00	CG	CG	CG	-
$Fr = 0.15, 0.20, 0.25, ..., 0.55, 0.60, 0.70, ..., 1.50, 1.60$				
Total number of coarse-grid (CG) simulations				120
Total number of fine-grid (FG) simulations				240
Total number of simulations				360

3.2.4 Input and output parameters

As input parameters of our DDSM, we initially consider Froude number (Fr), Rayleigh number (Ra_H), cavity width aspect ratio (A_w), temperature (T) and velocity magnitude (U) probes at seven different locations on the mid-depth cavity plane ($z = D/2$). In total, we use 17 ($Fr + Ra_H + A_w + 7T + 7U$) input parameters. The positions of the probes are shown in the figure 3.1 (right). The positions of the probes are chosen according to the results of our previous work [29]. Most probes are located near the walls of the cavity in order to mimic the positions of real temperature and velocity sensors. The input dataset with all of the seven probes is used to compare the performance of different ML methods. For the problem of finding the optimal sensor location, the number of input features is reduced, which is explained in detail in Section 3.4.

As the outputs of the model, we choose five global flow parameters: average Nusselt number on the hot wall - $<Nu>$, average kinetic energy - $<E>$, average enstrophy - $<\Omega>$, average temperature of the cavity - $<T_V>$, and the jet separation point - x_{sep}. They represent basic airflow properties and are relevant for thermal comfort [30]. The average Nusselt number is a measure of heat transfer. It is computed using the temperature gradient at the bottom wall surface:

$$<Nu>= -\frac{1}{WD}\int_{x=0}^{W}\int_{z=0}^{D}\frac{\partial <T>}{\partial y}dx\,dz \quad \text{at} \quad y=0, \tag{3.4}$$

where, the standard bracket "<>" notation is used for time-averaged values. The average temperature is the operative room temperature. It represents the thermal properties of the flow and is averaged over time and cavity volume:

$$<T_V>= \frac{1}{WHD} \int_{x=0}^{W} \int_{y=0}^{H} \int_{z=0}^{D} <T> dx\,dy\,dz. \tag{3.5}$$

Kinetic energy is a measure of the level of motion, whereas enstrophy is a measure of turbulence intensity. Both kinetic energy and enstrophy are directly related to draught and local discomfort. They are averaged over time and cavity volume and calculated as follows:

$$<E>= \frac{1}{WHD} \int_{x=0}^{W} \int_{y=0}^{H} \int_{z=0}^{D} \frac{<\mathbf{u}^2>}{2} dx\,dy\,dz \tag{3.6}$$

$$<\Omega>= \frac{1}{WHD} \int_{x=0}^{W} \int_{y=0}^{H} \int_{z=0}^{D} <\boldsymbol{\omega}^2> dx\,dy\,dz, \tag{3.7}$$

where $\boldsymbol{\omega} = \nabla \times \mathbf{u}$ is the vorticity. Jet separation point is an important parameter to measure velocity comfort in a room. It is determined as a point at the top cavity wall, where the wall-shear stress $<\tau_W>$ is equal to zero:

$$x_{sep} = x, \text{ at } <\tau_W>= \int \frac{\partial <u>}{\partial y} dz = 0, y = H. \tag{3.8}$$

3.3 Numerical methods

3.3.1 CFD simulations

To generate input and output data for the model, we use large-eddy simulations (LES) on staggered grids with second-order symmetry-preserving spatial discretization [31] and a one-parameter fully explicit second-order temporal discretization scheme [32]. To perform the simulations, we use an in-house CFD code developed by Gorobets *et al.* [33] with the LES-S3PQ turbulence model [34]. The choice of the turbulence model, type of spatial and temporal discretizations, and CFD software are based on the findings of our previous work [1]. There we performed an extensive validation and mesh sensitivity analysis of the same test case ($Ra_H = 2.4 \times 10^9$, $Fr = 0.81$, and $A_w = 1$) comparing different LES and Reynolds average Navier-Stokes (RANS) turbulence models, spatial grid resolutions and discretization techniques. The Cartesian staggered grid with $N_x = 120$, $N_y = N_{outlet} + N_{bulk} + N_{inlet} = 20 + 120 + 20 = 160$, $N_z = 30$ or 5.76×10^5 total control volumes showed the best trade-off between computational cost and accuracy for the aforementioned test configuration. This grid resolution is used as reference for the fine grids in this study. On the other hand, the coarse grid resolution is based on the grid with $N_x = 60$, $N_y = N_{outlet} + N_{bulk} + N_{inlet} = 7 + 60 + 8 = 75$, $N_z = 16$, which is the coarsest grid that showed reasonable accuracy in our previous study [1].

The task of choosing optimal grid discretization for the CFD simulations is a complex procedure, especially if one plans to simultaneously perform many simulations. On one hand, the nature of LES turbulence modeling requires sufficient spatial discretization [35] in order to obtain accurate simulation results. On the other hand, the high computational cost of the simulations requires the optimization of the grid size by tuning it to the physics and geometry of each individual test case. Moreover, it is not feasible to conduct mesh sensitivity analysis and validation for hundreds of CFD simulations. As a solution to this problem, we have developed an algorithm for the automatic mesh generation based on the variable physical parameters of the experiment (Fr, Ra_H, A_w), previously conducted validations [1], and desired level of mesh refinement.

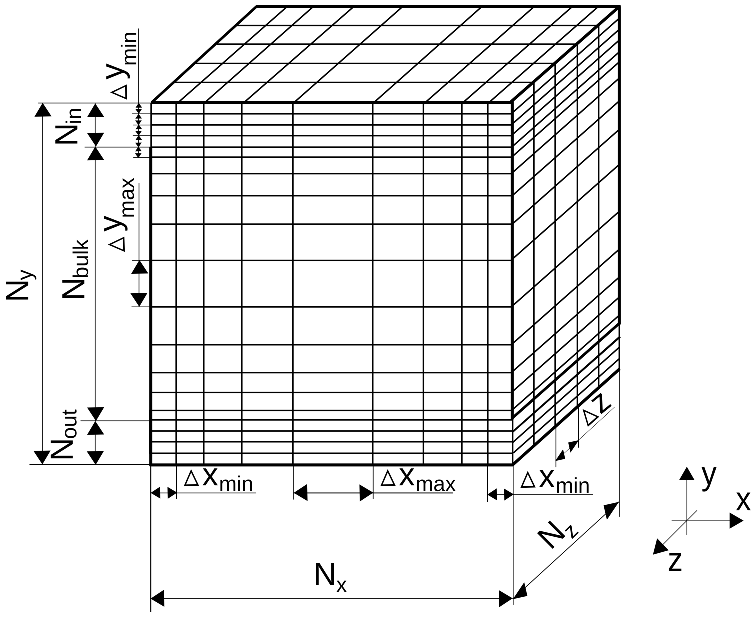

Figure 3.2: Schematic image of the computational grid used in the study.

All of the computational grids are structured and Cartesian.The schematic image of a computational grid used in this study is shown in Figure 3.2. The biggest cells are located in the center of the domain, their maximum size in the vertical (y) and horizontal (x) directions $(\Delta x_{max} = \Delta y_{max})$ is determined using the Grötzbach estimate [36] defined as follows:

$$\eta_{Grö} \leq \frac{\pi Pr^{1/2}}{(Nu-1)Ra_H{}^{1/4}} \quad \text{for} \quad Pr \leq 1 \tag{3.9}$$

$$\Delta y_{max} \approx C_r \eta_{Grö}, \tag{3.10}$$

where the average Nusselt number Nu is approximated using the expression $Nu \approx 0.373(FrRa_H)^{0.2}$. The expression is derived using results of our previous works [29,37].

The smallest cells are located at the walls, their minimum cell size in the vertical direction - Δy_{min} is determined by the flow in the inlet area and calculated as:

$$\Delta y_{min} \approx C_r \frac{h_{in}}{2} Re_\tau^{-1}, \tag{3.11}$$

where $Re_\tau = \sqrt{3/2Re_{h_{in}}}$ is the friction Reynolds number for the laminar flow, and $Re_{h_{in}} = U_{in}h_{in}/\nu$ is the Reynolds based on the inlet height. C_r is the coefficient of the refinement. Equations (3.9)-(3.11) estimate the size of the computational grid required for the DNS simulations; thus, the value of $C_r = 1$ corresponds to the DNS level of refinement. The use of LES turbulence modeling allows the use of coarser grids, thus values of $C_r > 1$ are adopted in this study.

In the horizontal (x) direction grids are refined near the walls using the hyperbolic tangent function:

$$x = \frac{W}{2}\left(1 + \frac{\tanh\{\gamma_x(2(i-1)/N_x - 1)\}}{\tanh\gamma_x}\right), \tag{3.12}$$

where, γ_x is the concentration factor, N_x is the number of grid points, and $i \in [1, 2, ..., N_x]$ is the index of the grid point in the horizontal direction respectively. Their values follow by imposing $\Delta x_{min} = 4\Delta y_{min}$ and $\Delta x_{max} = \Delta y_{max}$, where Δx_{min} is the first off-wall control volume, Δx_{max} is the control volume in the center of the cavity, and $\Delta x_{min}/\Delta y_{min} = 4$ is the ratio, used to balance the trade-off between the computational cost and accuracy.

In the vertical (y) direction the grids are uniform in the zones of the inlet $(N_{in} = h_{in}/\Delta y_{min})$ and the outlet $(N_{out} = N_{in})$ and refined in the bulk region using a hyperbolic tangent function similarly to equation (3.12). Both γ_y and N_{bulk} are found iteratively using the ratio between the minimum, Δy_{min} and the maximum, Δy_{max} cell size. The grids are uniform in the spanwise (z) direction and the number of grid points is calculated as $N_z = 1.1D/\Delta y_{max}$, where 1.1 is the ratio suggested by [38].

However, the level of grid refinement should be high enough, in order to ensure grid independence. Unfortunately, for the sake of covering the maximum amount of the possible working conditions using limited computational resources, some of the CFD simulations were performed using coarse computational. Table 4.1 shows the level of grid refinement for each batch of the test cases. For the fine grids, we used $C_r = 3$ (27 times coarser than DNS), and for the coarse grid simulations, we used $C_r = 6$ (216 times coarser than DNS). According to our previous studies [1], where we performed and validated CFD simulations of the same test case, the computational grid with $C_r = 3$ is sufficiently fine to achieve accurate results.

All simulations run for 500 non-dimensional time units (H/U_{in}), a long enough time-integration period to record the flow statistics for further averaging. In total, we carry out 360 CFD simulations (see Table 4.1), 20% of which are reserved for testing, and 80% are used in the model training. Test set is chosen randomly from the whole dataset before the beginning of the model training process.

3.3.2 Data-driven models

This section gives a brief description of the machine learning approaches used in this study together with the description of the training and testing process. We used four different DDSMs, namely artificial neural network (ANN), support vector regression (SVR), gradient boosting regression (GBR), and Gaussian process regression (GPR).

Table 3.2: Summary of the tested machine learning approaches and their hyperparameters.

Model name	Tested hyperparameters	Values	Final set
ANN	Hidden layers	1, 2	1
	Hidden layer neurons	2, 4, ..., 20	16
	Activation function	Linear, ReLU	ReLU
SVR	Kernel	Linear Polynomial Radial basis (RB)	RB
	Regularization strength	10, 50, ..., 500	100
	Epsilon-tube width	0.01, 0.02, ..., 0.1	0.05
GBR	Learning rate	0.01, 0.02, ..., 0.1	0.02
	Estimators	10, 50, ..., 500	100
	Max tree depth	2, 3, ..., 8	3
	Minimal samples split	2, 3, ..., 8	4
	Minimal samples leaf	2, 3, ..., 8	2
GPR	Kernel	Linear Dot product Radial basis (RB)	RB

ANN is a machine learning framework where the input is mapped to the output using a set of interconnected nodes or neurons. Neural networks can implicitly detect complex non-linear relationships between dependent and independent variables and support multiple training algorithms. However, their disadvantages include its “black boxâ nature and proneness to overfitting. Usually, ANN consists of one input layer, one or several hidden layers, and one output layer. The number of neurons in the input and output layer represents the number of model parameters and output values. In contrast, the number of neurons in the hidden layer can be arbitrary. Training neural networks involve determining the appropriate combination of the number of hidden layers, the number of neurons in them, and the associated weight coefficients that minimize the prediction error. The ANN that showed the minimal prediction error is composed of one hidden layer with 16 neurons and a rectified linear unit (ReLU) neuron activation function. All of the tested hyperparameter combinations are summarized in Table 3.2. In our work, we use the open-source ANN library Keras [39].

SVR [40] is a machine learning framework that encodes non-linear relationships between the inputs and outputs by mapping the data in a high dimensional feature space, where the number of dimensions corresponds to the number of inputs. SVR is a robust model which can effectively work with a small number of training samples. However, SVR is not suitable for large datasets and does not perform well on noisy datasets. Training SVR is essentially performing linear regression in that high dimensional feature space. The mapping function is also called the "kernel" function. During the optimization of our SVR model, we tested different kernels, regularization strength values, and the sizes of epsilon-tube. Regularization strength is a parameter which discourages the creation of complex predictive models and controls overfitting. The size of epsilon-tube determines the width of the tube around the estimated function. Points that fall inside this tube are considered as correct predictions and are not penalized by the algorithm. The optimal hyperparameter configuration for our SVR model is the radial basis kernel function with the values of regularization strength and epsilon-tube size equal to 100 and 0.05, respectively. Other tested configurations are summarized in Table 3.2.

GBR [41] is a technique that combines weak prediction models (usually decision trees) into a single strong learner in an iterative fashion. The algorithm adds one tree at each stage, optimizing a cost function by moving in the negative gradient direction. GBR usually shows high accuracy prediction and fast training. Nevertheless, this model, similarly to ANN, is prone to overfitting. In our GBR model, we use regularization, characterized by the learning rate. The decision trees in GBR are characterized by the maximum tree depth, a minimal amount of samples to split a brunch, and a minimal amount of samples to form a leaf. Another critical parameter of GBR is the number of estimators, which is the number of boosting stages to perform. We tested different values of the aforementioned parameters (see Table 3.2). We chose GBR with the learning rate of 0.02, 100 estimators, maximum tree depth of 3, minimal samples split of 4, and minimal samples leaf of 2. This combination of parameters showed the highest accuracy for our model.

GPR [42] is a kernel-based machine learning technique for non-linear regression problems, similar to SVR. A Gaussian Process (GP) is a set of random variables, such that any finite subset of these variables has a joint Gaussian distribution. GPR is a flexible approach capable of adapting to a wide range of problems by customizing kernel functions. Yet, GPR usually loses efficiency in high dimensional spaces with many input parameters and cannot handle large datasets. As a distribution, a GP is characterized by its kernel function and covariance function. Due to the Bayesian context of its formulation and interpretation, GPR has a probabilistic nature and gives prediction intervals instead of specific prediction points. In our work, we use radial basis kernel function with length scale equal to 0.2 and length scale bounds of $(10^{-3}, 10^{3})$ and the Gaussian squared-exponential covariance function, since they showed the highest prediction accuracy on our data. However, we also tested dot product kernel and linear kernel functions.

For the SVR, GBR, and GPR frameworks, we use the open-source library Scikit-learn [43].

The nature of these three models (SVR, GBR, and GPR) only supports single output problems. In order to predict all five output parameters in a single model, we use a multi-output regressor, which fits one regressor per target.

3.3.3 Data preprocessing and metrics

One of the most critical aspects of creating DDSMs is data preprocessing. The available dataset should be adequately scaled to make sure all the features have the same order of magnitude. In our work, we normalize all the input and output data to fit the range of $[-1, 1]$. Similar input parameters are grouped in order to apply the same normalization scale; for example, all the values of the velocity magnitudes from all the sensors and all the scenarios are normalized simultaneously. The same procedure is done for all of the temperature sensor readings. However, each of the output parameters is scaled separately, as well as the Fr, Ra_H and A_w from the input dataset.

We use 80% of the available data for model training and 20% for testing. Moreover, to improve the prediction results and avoid model overfitting (lack of generalization) we use cross-validation. In this study, we adopt a leave-one-out (LOO) cross-validation method. LOO is a specific case of the standard k-fold cross-validation [44]. For the LOO cross-validation at each training run, the learning set is created by taking all the samples except one, the validation set being the sample left out. Thus, for N samples, we have N different training sets and N different validation sets. This cross-validation procedure maximises the amount of data used for training since only one sample is removed from the training set. Moreover, LOO cross-validation is less biased because of the small difference in size between the training set used in each fold and the entire dataset. It is a suitable technique for small datasets.

In order to quantify the accuracy of the model, we use mean relative prediction error (MRE), which is designed as follows:

$$MRE(\phi) = \frac{1}{N}\sum_{i=1}^{N} \frac{|\phi_{CFD} - \phi_{DDSM}|}{|\phi_{CFD}|}, \tag{3.13}$$

where N is the number of samples in the test dataset, ϕ_{CFD} represents any one of the 5 comfort-related parameters calculated from the CFD simulations, and ϕ_{DDSM} represents a prediction from one of the DDSMs of any one of the 5 comfort-related parameters. We assume that less than 5% MRE is acceptable for this model.

3.4 Results

3.4.1 Comparison of different DDSM approaches

Table 3.3 shows a comparative analysis of results for all the models developed in this study. The table presents MREs (equation (4.21)) for each of the model output parameters (equations (3.4)-(3.8)). The result are obtained using 17 ($Fr + Ra_H + A_w + 7T + 7U$) input parameters from 360 CFD simulations, among which 288 were used for training and 72 - for testing.

Table 3.3: Mean relative prediction error (MRE) of the studied flow parameters for different models on the test dataset.

Model	MRE					
	$< Nu >$	$< E >$	$< \Omega >$	$< T_V >$	x_{sep}	Mean
ANN	0.012	0.022	0.184	0.164	0.219	0.120
SVR	0.010	0.004	0.032	0.034	0.079	0.032
GBR	0.018	0.025	0.028	0.017	0.064	0.030
GPR	0.034	0.032	0.095	0.016	0.065	0.048

Nusselt number on the hot wall $< Nu >$ and average kinetic energy $< E >$ are the flow parameters, which are accurately predicted by all of the tested models. The MRE for these two flow parameters does not exceed 5% (0.05) and is minimal for the SVR approach. However, average enstrophy $< \Omega >$ is more difficult to be captured correctly, and ANN shows MRE as high as 18%. A similar picture could be observed for the average cavity temperature $< T_V >$ and flow separation point x_{sep}, which is accurately predicted by all modeling frameworks except ANN. The smallest MRE for average enstrophy, average cavity temperature, and flow separation point is given by the GBR, which also has the smallest mean MRE. SVR and GPR are performing similarly to the GBR. However, ANN is not capable of producing accurate predictions for some of the output parameters.

The amount of data required for the DDSMs development is always a compromise between the computational cost and accuracy. Moreover, the creation of the dataset is usually the most time-consuming part of the model generation. CFD simulations have high computational cost, therefore it is useful to determine the optimum size of the training dataset to minimize the time and computational resources required to develop the model without compromising the model's accuracy.

Figure 3.3 shows the relationships between the number of samples in the dataset and the accuracy of the prediction. The models are constructed using between 10 and 360 samples. There is a smooth decrease in the MRE with the increase of the number of samples in the dataset. However, most of the models converge to a steady prediction error at around 150 samples. Further increase in the dataset size provides a negligibly small decrease of the prediction error. Nonetheless, SVR requires at least 200 samples to accurately predict the Nusselt number. Moreover, unlike other models, ANN does not always provide a smooth error decrease with the increase of the dataset size.

SVR, GBR, and GPR are performing similarly and show similar levels of prediction errors. Nonetheless, ANN performs differently from three other DDSMs; it generally exhibits lower accuracy, which is not improved by increasing the dataset size. The nature of ANNs could explain this discrepancy. Neural networks have probabilistic nature, as they fit parameters to transform the input and indirectly direct the activations of the following neurons. On the other hand, SVR and GBR are deterministic and explicitly fit parameters to direct the information

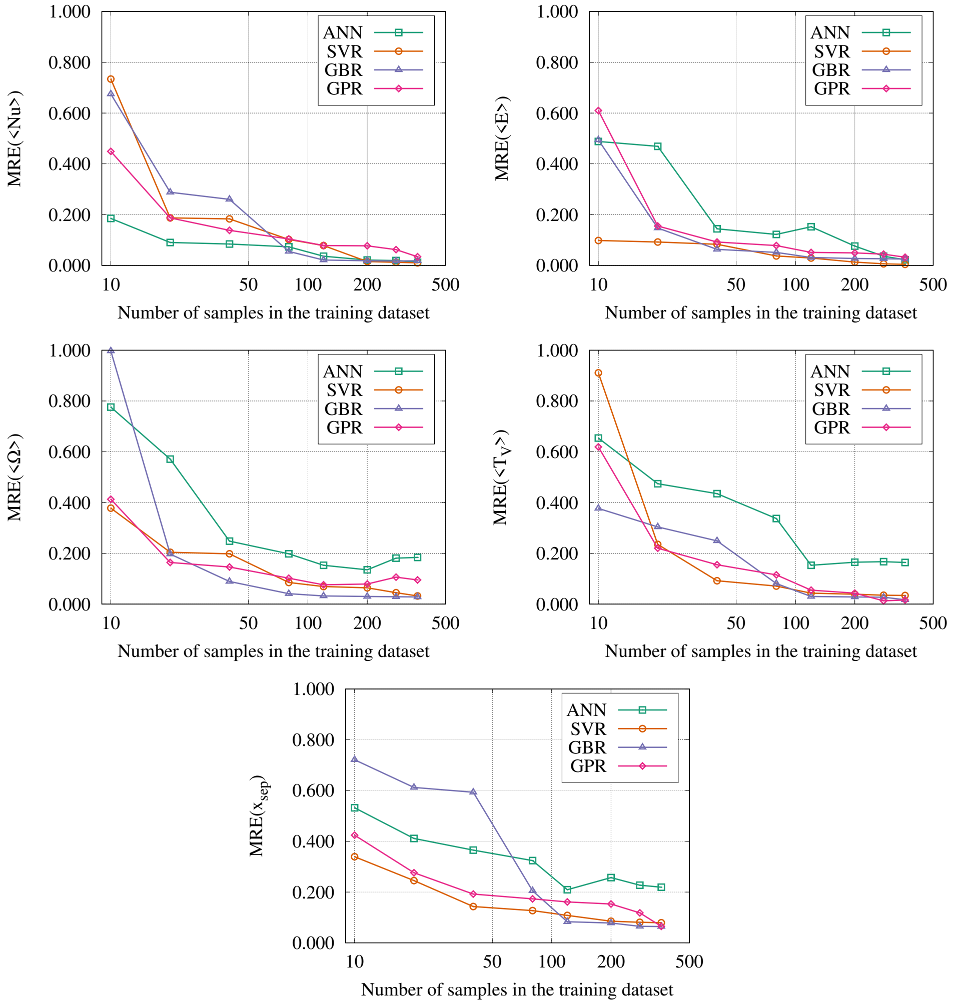

Figure 3.3: Mean relative error (MRE) of the studied flow parameters for different number of samples in the training dataset and different ML models. Top left: Nusselt number on the hot wall, $< Nu >$. Top right: average kinetic energy, $< E >$. Middle left: average enstrophy, $< \Omega >$. Middle right: average cavity temperature, $< T_V >$. Bottom: flow separation point, x_{sep}.

flow [45]. Deterministic models usually handle small-sized datasets more accurately, while neural networks are more oriented towards complex problems involving a significant amount of data. It, therefore, appears that the GBR framework is the most suitable data-driven model for this kind of problem, as it shows an overall lowest level of errors. GBR framework is adopted for further analysis.

3.4.2 Optimal sensor position for the prediction of flow parameters

In this section, we adapt the previously developed model for the requirements of MPC. Predictive building models usually use sensor readings, weather data, heating and cooling loads, and geometrical parameters of the building as input data [46]. Therefore, in order to make our predictive model suitable for MPC applications, the input data should be structured in a way that once the model is trained, it would not require any additional simulations for the model usage. With this idea in mind, we decided to reduce the number of input parameters of the model and also relocate the positions of the temperature and velocity probes, so they could imitate the actual thermal sensor locations. The model is then trained and tested using different combinations of input parameters in order to determine the optimal sensor position for the prediction of flow parameters.

Temperature and velocity sensors are usually located alongside the walls and ceiling of the rooms. In the previous subsection, we used the probes located as shown in the Figure 4.1 (right). Not all of these probes could be replaced by the sensor readings. For example, probe 4 is located in the center of the cavity, where it is impractical to install a sensor. Likewise, probe 6 is located on the floor. In a practical case, indoor spaces are hardly ever equipped with more than two sensors per room. Thus, to optimize the prediction model's performance, the number of probes is reduced to two. Their locations are limited by the zones near the ceiling and the sidewalls (Figure 3.4), which are the zones where temperature and velocity sensors could be installed. We did not consider placing more than two sensors since the model could reach sufficient accuracy with the data available. Perhaps, the increased amount of sensors could help reduce the number of samples in the training dataset; however, it is out of the scope of the present study. Moreover, in a realistic situation, apart from the cavity width aspect ratio, the values of the Froude and Rayleigh numbers are not available; hence they are discarded from the current study. As a result, the total number of the input parameters is equal to 5 ($A_w + 2T + 2V$).

Therefore, in order to find the optimal positions of the probes, we try 361 different combinations of positions (19 per wall) for each scenario, detailed in the Figure 3.4. In configuration 1, one sensor is located at the ceiling and another at the left wall; in configuration 2, one sensor is again located at the ceiling and another at the right wall. In configuration 3, there is one sensor on each lateral wall. Thick black lines in the Figure 3.4 show all the possible combinations of sensors for each studied configuration, while only two positions at the time are used in the model. The position of the sensor location is considered optimal when the MRE of the predicted flow parameters is minimal. Figures 3.5-3.9 show mean relative prediction errors of each output parameter ($<Nu>, <E>, <\Omega>, <T_V>, x_{sep}$) for different sensor positions for each of the studied sensor combinations from Figure 3.4. The MRE for each flow parameter is averaged over the whole test set. Positions of the ceiling sensors are relative to the cavity width aspect ratio.

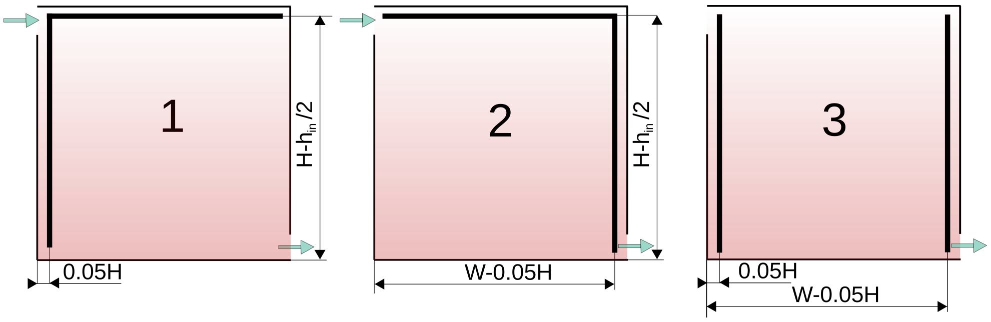

Figure 3.4: Studied combinations of temperature and velocity sensor locations. Thick black lines represent the possible positions of the probes.

Figure 3.5 shows the mean relative prediction error of the Nusselt number for different combinations of sensor positions. The shadows of the green show the values from the lowest MRE (dark green) to the highest (light yellow), respectively. For the configuration 1, the most accurate Nusselt number prediction is achieved when the sensors are located at the top of the left wall and near the corners of the ceiling. These are the zones where most of the changes occur, located near the inlet and the jet separation area. For sensor configuration 2 (ceiling and the right wall), the smallest relative errors occur when the ceiling sensor is near one of the sidewalls and at the bottom of the right wall, which is close to the flow outlet. A similar tendency is observed for the third configuration, where sensors near the top of the left and the right wall give the most accurate predictions. Even though, the maximum MRE for the $<Nu>$ is as high as 80%, the minimum errors for all of the sensor configurations are around 1%.

As could be seen in Figure 3.6, the error distribution for kinetic energy is drastically different from the Nusselt number. The minimal relative errors are located at the central areas (dark blue zones) for all sensor configurations. Moreover, the results for configurations 1 and 2 are almost identical. The best result is achieved when a ceiling sensor is placed at the right corner and the wall sensor is placed at the mid-height. For configuration 3, the error is minimal when the left wall sensor is located at the mid-height and the right wall - at the top of the wall. However, the maximum MRE does not exceed 9% for any of the studied arrangements.

Figure 3.7 shows the MRE for average enstrophy. For configurations 1 and 2 (see Figure 3.4), the error distribution is almost identical. The lowest errors are achieved when the ceiling sensor is placed at the corners or the center of the cavity. The wall sensor for these configurations should also be located at the top, bottom, or the wall center. On the other hand, configuration 3 shows the best results when at least one of the sensors is located in the center of the wall. However, there is a minimal zone of sensor positions, where the $MRE(<\Omega>)$ is very high, and for most of the domain, the error does not exceed 10%.

The mean relative error for the averaged cavity temperature is shown in Figure 3.8. The maximum $MRE(<T_V>)$ is reached when one sensor is placed at the central part of a ceiling and the other - at the central part of a wall (configurations 1 and 2). In this area, the error

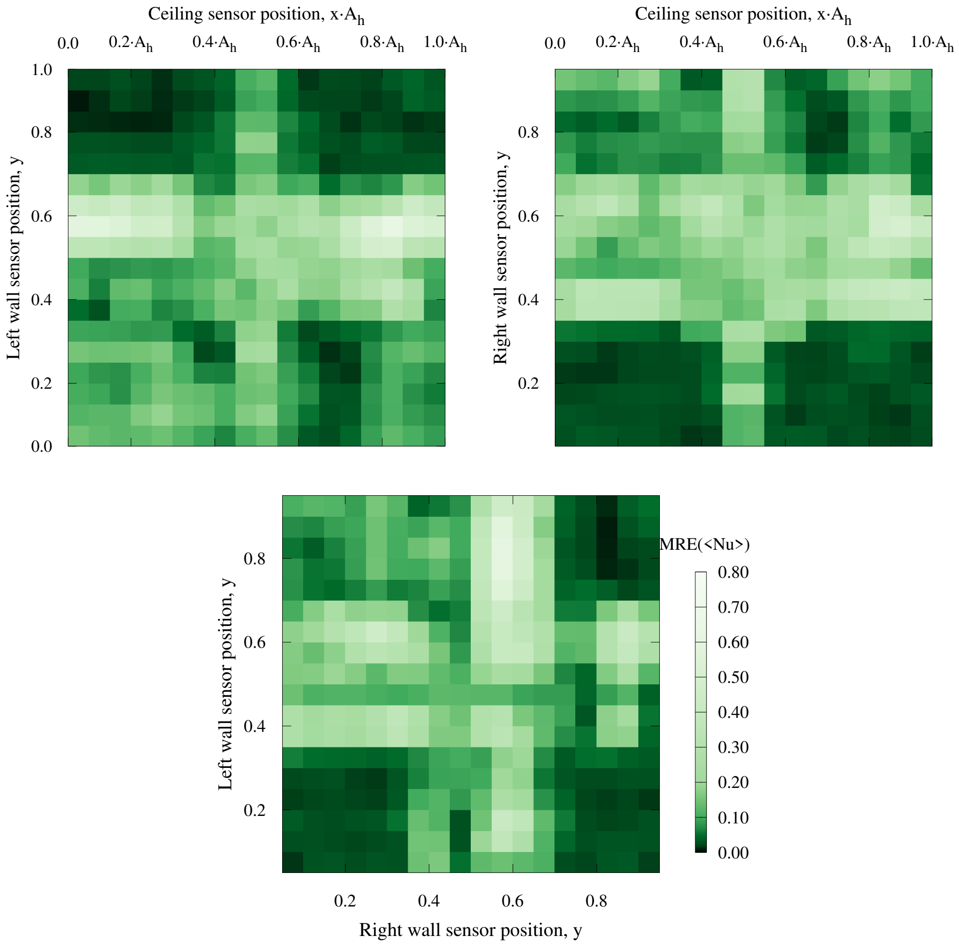

Figure 3.5: Mean relative error of the averaged Nusselt number $MRE(< Nu >)$ for different sensor positions. Top left - sensors at the ceiling and the left wall (configuration 1 in Figure 3.4). Top right - sensors at the ceiling and the right wall (configuration 2 in Figure 3.4). Bottom - sensors at the left and right wall (configuration 3 in Figure 3.4), where the right wall is assigned to the x axis.

level is reaching 70%; nevertheless, the remaining sensor positions have the MRE below 5%. Configuration 3, where both sensors are placed at the sidewalls, is the most favorable for the accurate temperature prediction. Almost any combination of the sensor positions is showing

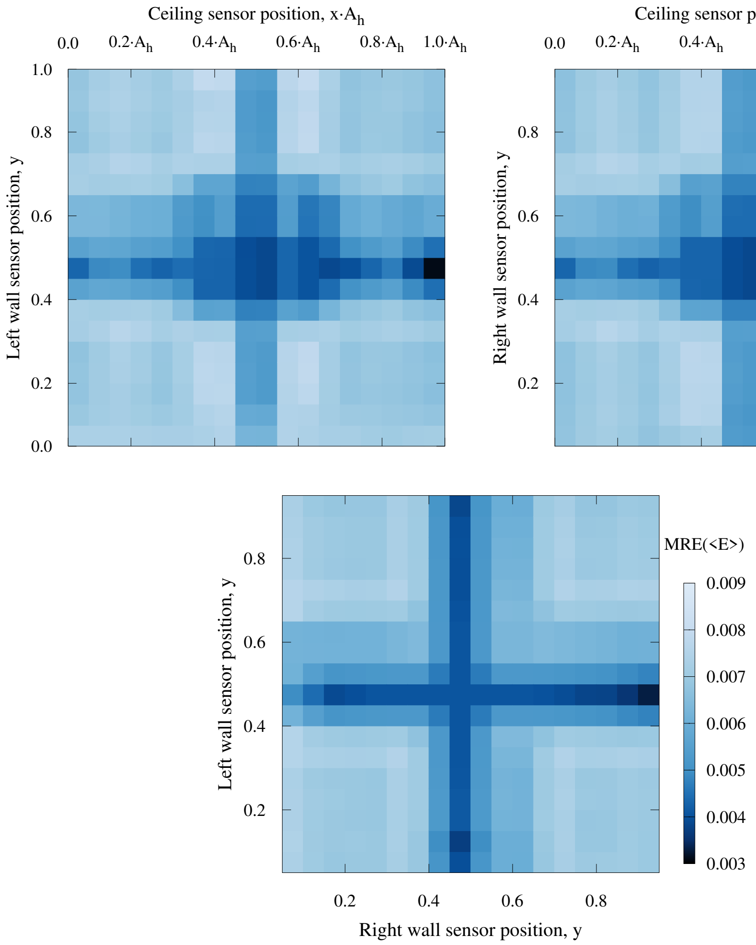

Figure 3.6: Mean relative error of the averaged kinetic energy $MRE(<E>)$for different sensor positions. Top left - sensors at the ceiling and the left wall (configuration 1 in Figure 3.4). Top right - sensors at the ceiling and the right wall (configuration 2 in Figure 3.4). Bottom - sensors at the left and right wall (configuration 3 in Figure 3.4), where the right wall is assigned to the x axis.

good accuracy.

Flow separation point, x_{sep}, shown in Figure 3.9 is easily predicted by all of the approaches, the maximum MRE does not exceed 6%. However, the error is minimal when sensors are

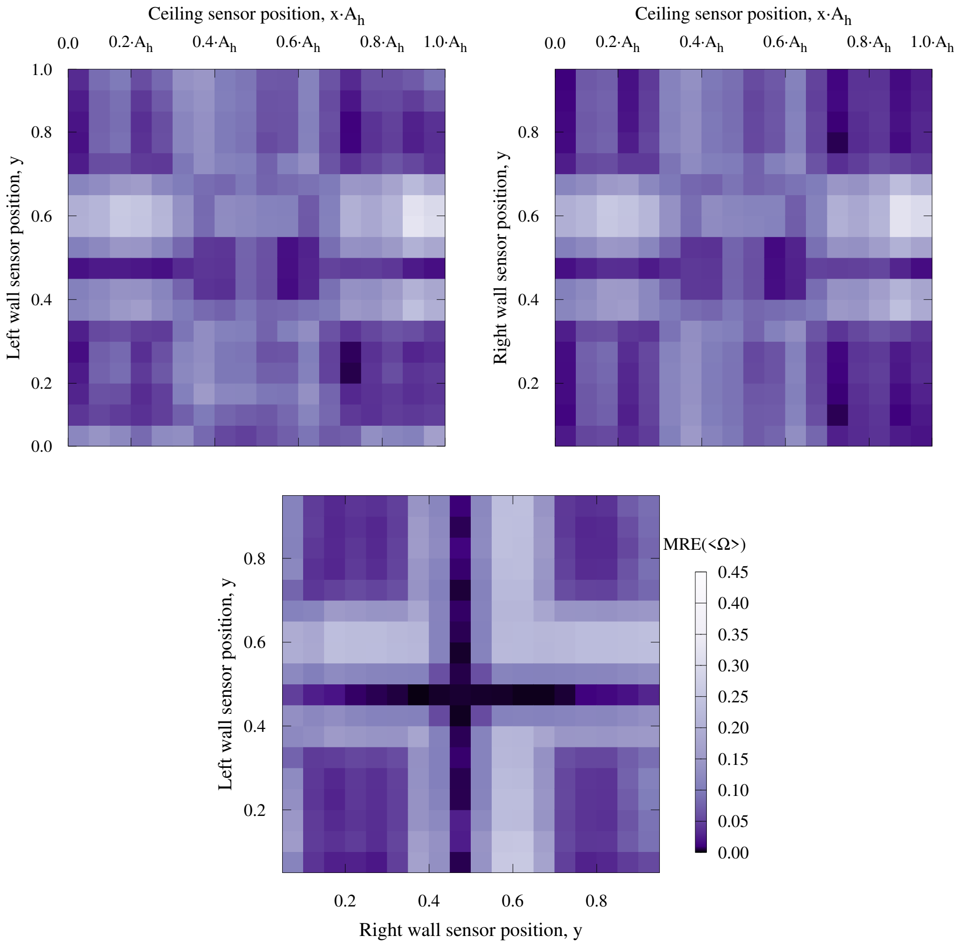

Figure 3.7: Mean relative error of the averaged enstrophy $MRE(<\Omega>)$ for different sensor positions. Top left - sensors at the ceiling and the left wall (configuration 1 in Figure 3.4). Top right - sensors at the ceiling and the right wall (configuration 2 in Figure 3.4). Bottom - sensors at the left and right wall (configuration 3 in Figure 3.4), where the right wall is assigned to the x axis.

located near the corners of the walls or the ceiling. As can be seen from the figure, it is vital to place the sensors in the area where the velocity drop occurs in order to ensure accurate prediction of the flow separation point.

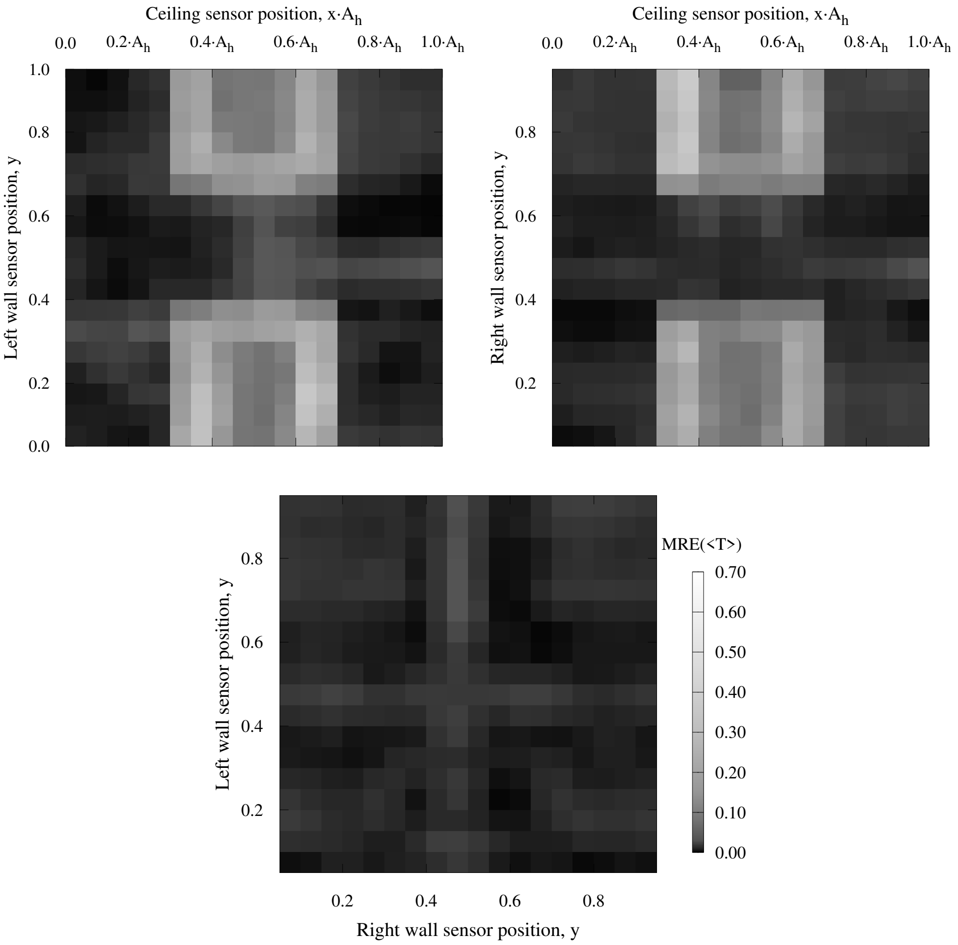

Figure 3.8: Mean relative error of the averaged cavity temperature $MRE(< T_V >)$ for different sensor positions. Top left - sensors at the ceiling and the left wall (configuration 1 in Figure 3.4). Top right - sensors at the ceiling and the right wall (configuration 2 in Figure 3.4). Bottom - sensors at the left and right wall (configuration 3 in Figure 3.4), where the right wall is assigned to the x axis.

The obtained results from Figures 3.5-3.9 show that the optimal position of the sensor varies from one flow parameter to the other; thus, it is interesting to determine the points where the model gives the accurate value of all of the parameters. In order to determine these points,

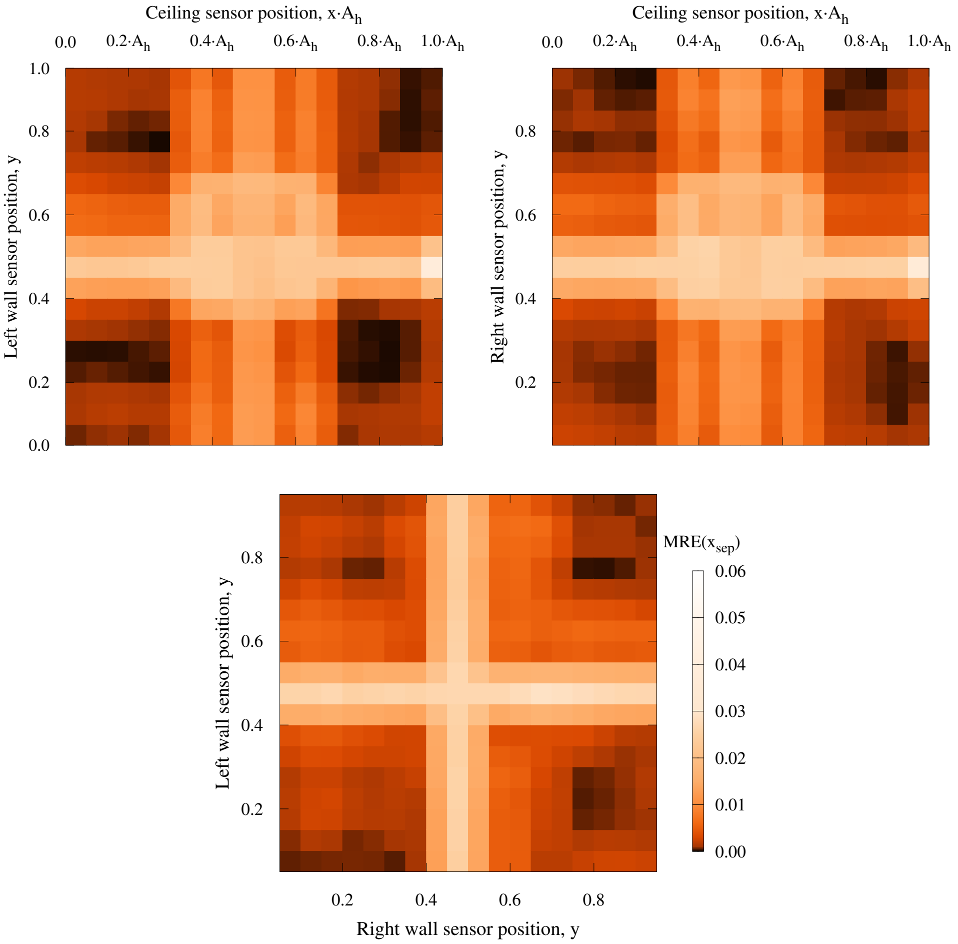

Figure 3.9: Mean relative error of the flow separation point $MRE(x_{sep})$ for different sensor positions. Top left - sensors at the ceiling and the left wall (configuration 1 in Figure 3.4). Top right - sensors at the ceiling and the right wall (configuration 2 in Figure 3.4). Bottom - sensors at the left and right wall (configuration 3 in Figure 3.4), where the right wall is assigned to the x axis.

Figure 3.10 shows the maximum MRE among all of the output parameters. The scale from dark to light represents the maximum MRE from low to high, respectively. For configuration 1 (top left figure), the lowest errors are observed when the ceiling sensor is located near the corners

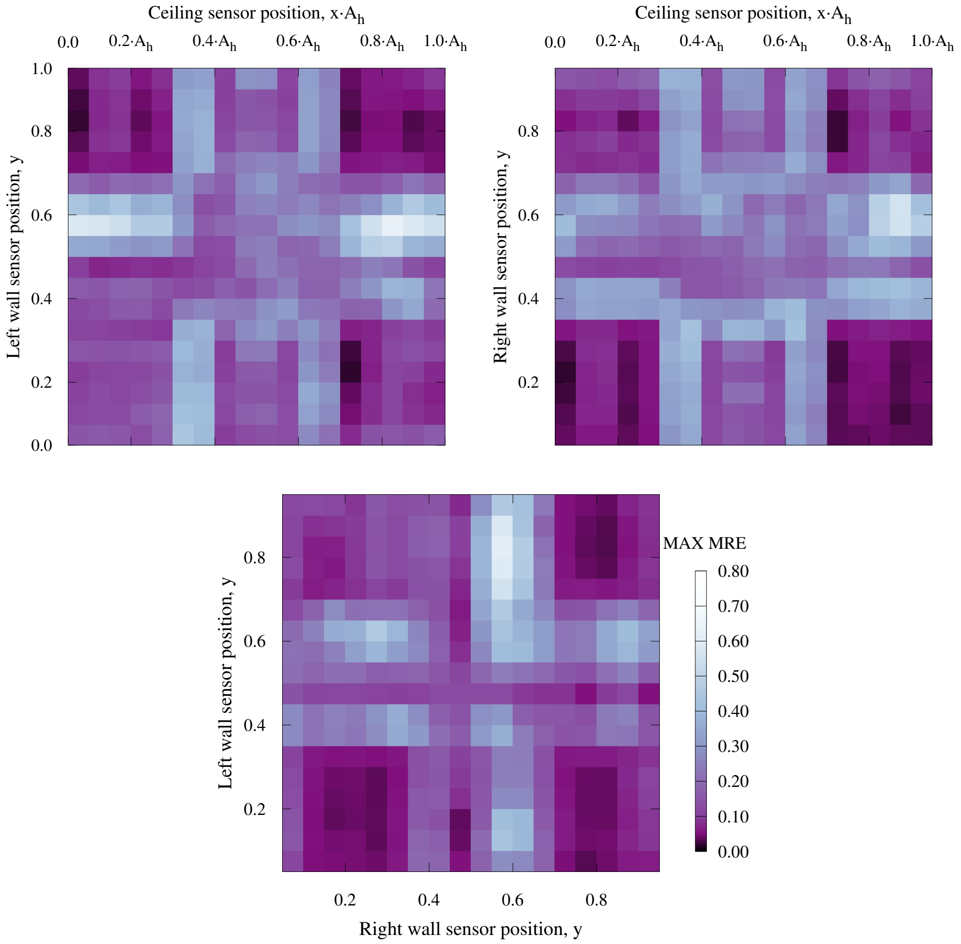

Figure 3.10: Maximum (among studied flow parameters) mean relative error for different sensor positions. Top left - sensors at the ceiling and the left wall (configuration 1 in Figure 3.4). Top right - sensors at the ceiling and the right wall (configuration 2 in Figure 3.4). Bottom - sensors at the left and right wall (configuration 3 in Figure 3.4), where the right wall is assigned to the *x* axis.

and the left wall sensor is located near the ceiling. On the other hand, configuration 2 (top right figure) shows higher accuracy when the ceiling sensor is located near the corners, and the right wall sensor is located near the floor. Configuration 3 (bottom figure) produces the lowest MRE when the right wall sensor is located near the ceiling, and the left wall sensor is located either near the ceiling or near the floor.

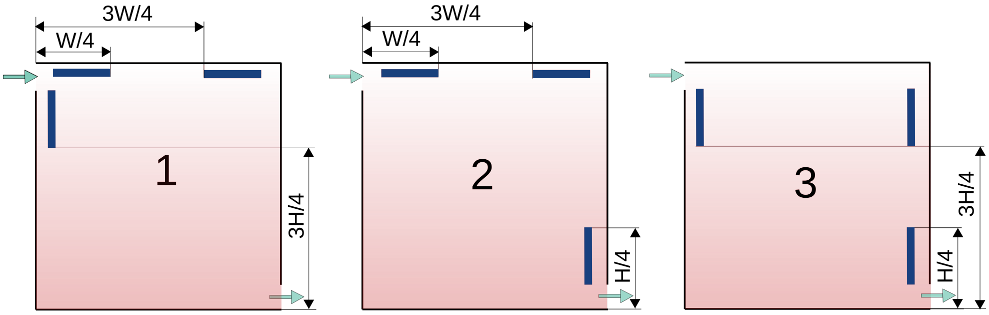

Figure 3.11: Locations of temperature and velocity sensors with the highest prediction accuracy. The thick blue lines show the best sensor positions.

It is important to note that certain sensor positions have very low sensitivity when capturing some of the flow parameters. For example, if at least one of the sensors is located in the central part of the wall, the prediction error for the Nusselt numbers increases up to 70% due to the low heat transfer in these zones. However, suppose the sensors are placed in the wall corners of the ceiling. In that case, the Nusselt number accuracy increases as a result of a more significant temperature difference in the sensor readings. On the contrary, the accuracy of the average temperature prediction benefits from sensors located in the central part of the walls because the temperature readings in these zones are closest to the mean temperature. In contrast, sensors located in the wall corners of the ceiling introduce considerable errors due to the bigger temperature difference between them. Therefore, when placing the sensors, a decision to prioritize the accuracy of the prediction of some flow parameters over the others is to be taken into account.

In this section, we showed that the developed model is capable of producing accurate results using only the data obtained from two sensor readings. Moreover, we determined which temperature and velocity sensors positions are preferable for the studied test case. The combinations of the sensors, which achieved the smallest maximum relative error, are shown in the Figure 3.11. The following section is dedicated to discussing the obtained results and the possible applications of the developed model.

3.5 Discussion

In this section, we present the interpretation of the obtained results, discuss the advantages and disadvantages of the data-driven models for indoor environmental simulations, and consider possible applications of the developed model.

The computational cost of the model development is a combination of the computational cost of CFD simulations and the model training cost. The latter is negligible - it takes approximately 2 minutes to train the model on a personal computer using four CPU cores. Moreover, after the training is completed, the prediction is produced almost instantly. Virtually all the computational effort is used to produce CFD data for the model training.

The CFD database was generated using MareNostrum 4 supercomputer at the Barcelona Supercomputing Center. We limited ourselves to 700Kh core-hours computational resources; hence, not all of the CFD simulations were performed with the same grid resolution (see Table 4.1 for details). In order to create the dataset, we were changing three physical parameters of the cases - Froude number, Rayleigh number, and the cavity width aspect ratio. The range in which these parameters were varying was chosen to represent the realistic indoor environments. However, test cases with high Rayleigh numbers and high width aspect ratios are considerably more computationally expensive than the others. We decided to compute these test cases with reduced mesh resolution in order to complete the dataset. Even though these simulations were less accurate, they still improved the accuracy of the data-driven model. The estimated cost of generating the whole dataset of 360 simulations (240 fine-grid and 120 coarse-grid) simulations is approximately 7000$ using Amazon Web Services with the Elastic Compute Cloud Spot Instances subscription [47]. This is a justifiable computational and financial cost for the DDSM development. These CFD simulations are carried out only once to form the input dataset and will not be repeated. All of the data obtained from these simulations, including the data not used in this work, has been carefully stored for future research.

The input data of the developed model is structured so that it takes the values of temperature and velocity in the locations, which could be replaced by sensor readings. This configuration of input data makes it possible to avoid costly CFD simulations at the model execution stage. Moreover, the output parameters of the model are directly related to the parameters of the thermal comfort, such as draft rating index (DR) [48] predicted mean vote (PMV) [30], and local thermal discomfort [49]. DR can be calculated using average kinetic energy $<E>$, average temperature $<T_V>$, and enstrophy $<\Omega>$. The average temperature is also used in calculations of PMV, while Nusselt number $<Nu>$ and flow separation point x_{sep} influence the local discomfort.However, the calculation of these thermal comfort coefficients is out of the scope of this work. The purpose of the developed model is a proof of concept; thus, a classical benchmark ventilated room test case was chosen in order to increase generalization capacity and avoid problem-setup specificity. Nonetheless, once the concept is proven, the model could be extended to a direct evaluation of comfort parameters in actual rooms with specific geometries.

Despite the small number of the input parameters, the model maintains the accuracy comparable to CFD, which is a significant advantage over conventional reduced-order multizone and zonal models, which are not suitable for handling complex physical phenomena. Moreover, the small computational cost makes the model attractive for applications where fast computations are required, such as MPC or early-stage conceptual building design. However, the main bottleneck of the DDSMs is their case dependency. Even though a wide range of room geometries and physical conditions was tested, the model is not universal and does not cover a full extension of possible indoor environmental configurations. The model would not be able to produce accurate results for the case significantly different from the training dataset, for example, a room with complex geometry or completely different working conditions.

Data-driven models are capable of providing rapid predictions for common room geometries. Furthermore, as they are based on high-fidelity data (CFD simulations), they consider temperature and velocity distributions inside individual rooms. Hence, DDSMs could be used for applications where a combination of fast and accurate predictions is required, for example, for model predictive control.

3.6 Conclusions

In this work, we created a CFD-based DDSM for predicting the comfort-related flow parameters in a benchmark three-dimensional ventilated cavity with a heated floor. The developed DDSM provides almost instant accurate predictions using an ordinary office computer. The input parameters of the DDSM are the values of the temperature and velocity magnitude at different probe locations within the cavity domain. The output parameters are the average Nusselt number on the hot wall, the jet separation point, the average kinetic energy, the average enstrophy, and the average temperature of the cavity.

First, we created a model that uses the readings of seven probes to test different ML frameworks. The gradient boosting regression outperformed other methods, while the artificial neural network showed the least accurate results. Next, in order to imitate the sensor readings, the number of probe locations was reduced to two, and the probes were placed near the ceiling and sidewalls of the cavity. Then the developed surrogate model was tested with the data from different combinations of sensor positions to determine the optimal areas of the sensor placement (Figure 3.11). The model can accurately predict comfort-related flow parameters using only the information from temperature and velocity sensor readings, which makes it possible to avoid repeated CFD simulations at the model execution stage by directly using onsite data.

The developed methodology is applicable to flow configurations with complex physical phenomena and commonly used indoor space geometrical configurations, like offices or classrooms. The methodology takes advantage of the detailed information about indoor airflow provided by accurate CFD simulations, which is usually not accessible by multizone and zonal reduced-order models. Moreover, in the case of public buildings, for example, offices, the type of ventilation systems and office geometry does not vary significantly inside one particular building, which makes the generation of the input data easier. As a result, a comprehensive dataset could easily be created. Therefore, the developed methodology could be used for applications where fast and accurate predictions are required, for example, for ventilation operation control.

References

[1] N. Morozova, F. X. Trias, R. Capdevila, C. D. Pérez-Segarra, and A. Oliva. On the feasibility of affordable high-fidelity CFD simulations for indoor environment design and control. *Building and Environment*, 184:107144, 2020.

[2] J. Axley. Multizone airflow modeling in buildings: History and theory. *HVAC&R Research*, 13(6):907–928, 2007.

[3] A. C. Megri and H. Fariborz. Zonal modeling for simulating indoor environment of buildings: Review, recent developments, and applications. *HVAC&R Research*, 13(6):887–905, 2007.

[4] K. Li, X. Wenping, C. Xu, and H. Mao. A multiple model approach for predictive control of indoor thermal environment with high resolution. *Journal of Building Performance Simulation*, 11(2):164–178, 2018.

[5] L. Phan and C.-X. Lin. Reduced order modeling of a data center model with multi-Parameters. *Energy and Buildings*, 136:86–99, 2017.

[6] X. Wang, J. Zhao, F. Wang, B. Song, and Q. Zhang. Air supply parameter optimization of a custom nonuniform temperature field based on the POD method. *Building and Environment*, 206:108328, 2021.

[7] W Zuo and Q. Chen. Real-time or faster-than-real-time simulation of airflow in buildings. *Indoor Air*, 19(1):33–44, 2009.

[8] J. Stam. Stable fluids. In *Proceedings of the 26th Annual Conference on Computer Graphics and Interactive Techniques*, pages 121–128, 1999.

[9] P. Westermann and R. Evins. Surrogate modelling for sustainable building design â A review. *Energy and Buildings*, 198:170–186, 2019.

[10] A. E. Ruano, S. Pesteh, S. Silva, H. Duarte, G. Mestre, P. M. Ferreira, H. R. Khosravani, and R. Horta. The IMBPC HVAC system: A complete MBPC solution for existing HVAC systems. *Energy and Buildings*, 120:145 – 158, 2016.

[11] H. Huang, L. Chen, and E. Hu. A neural network-based multi-zone modelling approach for predictive control system design in commercial buildings. *Energy and Buildings*, 97:86–97, 2015.

[12] A. Afram, F. Janabi-Sharifi, A. S. Fung, and K. Raahemifar. Artificial neural network (ANN) based model predictive control (MPC) and optimization of HVAC systems: A state of the art review and case study of a residential HVAC system. *Energy and Buildings*, 141:96–113, 2017.

[13] Q. Chen and N. Li. Fast simulation and high-fidelity reduced-order model of the multi-zone radiant floor system for efficient application to model predictive control. *Energy and Buildings*, 248:111210, 2021.

[14] H. Sözer and S. S. Aldin. Predicting the indoor thermal data for heating season based on short-term measurements to calibrate the simulation set-points. *Energy and Buildings*, 202, 2019.

[15] D. Koschwitz, E. Spinnräker, J. Frisch, and C. van Treeck. Long-term urban heating load predictions based on optimized retrofit orders: A cross-scenario analysis. *Energy and Buildings*, 208:109637, 2020.

[16] H. Park and D. Y. Park. Comparative analysis on predictability of natural ventilation rate based on machine learning algorithms. *Building and Environment*, 195:107744, 2021.

[17] G. Calzolari and W. Liu. Deep learning to replace, improve, or aid CFD analysis in built environment applications: A review. *Building and Environment*, 206:108315, 2021.

[18] J. Athavale, M. Yoda, and Y. Joshi. Comparison of data driven modeling approaches for temperature prediction in data centers. *International Journal of Heat and Mass Transfer*, 135:1039–1052, 2019.

[19] Q. Fang, Z. Li, Y. Wang, M. Song, and J. Wang. A neural-network enhanced modeling method for real-time evaluation of the temperature distribution in a data center. *Neural Computing and Applications*, 31(12):8379–8391, 2019.

[20] A. Warey, S. Kaushik, B. Khalighi, M. Cruse, and G. Venkatesan. Data-driven prediction of vehicle cabin thermal comfort: using machine learning and high-fidelity simulation results. *International Journal of Heat and Mass Transfer*, 148:119083, 2020.

[21] Q. Zhou and R. Ooka. Influence of data preprocessing on neural network performance for reproducing CFD simulations of non-isothermal indoor airflow distribution. *Energy and Buildings*, 230:110525, 2021.

[22] C. Lamberti, G.and Gorlé. A multi-fidelity machine learning framework to predict wind loads on buildings. *Journal of Wind Engineering and Industrial Aerodynamics*, 214:104647, 2021.

[23] X. Tian, Y. Cheng, and Z. Lin. Modelling indoor environment indicators using artificial neural network in the stratified environments. *Building and Environment*, 208:108581, 2021.

[24] Z. Zhang, W. Zhang, Z. J. Zhai, and Q. Y. Chen. Evaluation of various turbulence models in predicting airflow and turbulence in enclosed environments by CFD: Part-2: Comparison with experimental data from literature. *HVAC&R Research*, 13(6):871–886, 2007.

[25] A. Limane, H. Fellouah, and N. Galanis. Thermo-ventilation study by OpenFOAM of the airflow in a cavity with heated floor. *Building Simulation*, 8(3):271–283, 2015.

[26] G. Yang, Y. Huang, J. Wu, L. Zhang, G. Chen, R. Lv, and A. Cai. Experimental study and numerical models assessment of turbulent mixed convection heat transfer in a vertical open cavity. *Building and Environment*, 115:91–103, 2017.

[27] J. Y. Wu, R. R. Lv, Y. Y. Huang, and G. Yang. Flow Structure Transition and Hysteresis of Turbulent Mixed Convection Induced by a Transverse Buoyant Jet. *International Journal of Heat and Mass Transfer*, 177, 2021.

[28] D. Blay, S. Mergui, J. L. Tuhault, and F. Penot. Experimental turbulent mixed convection created by confined buoyant wall jets. In *Proceedings of the First European Heat Transfer Conference, UK*, pages 821–828, 1992.

[29] N. Morozova, F. X. Trias, R. Capdevila, and A. Oliva. Data-driven prediction of flow parameters in a ventilated cavity. In *Proceedings of Building Simulation 2021: 17th Conference of IBPSA*, September 1-3, 2021.

[30] Ergonomics of the thermal environment â Analytical determination and interpretation of thermal comfort using calculation of the PMV and PPD indices and local thermal comfort criteria. Standard, International Organization for Standardization, Geneva, CH, 2005.

[31] R. W. C. P. Verstappen and A. E. P. Veldman. Symmetry-preserving discretization of turbulent flow. *Journal of Computational Physics*, 187(1):343–368, 2003.

[32] F. X. Trias and O. Lehmkuhl. A self-adaptive strategy for the time integration of Navier-Stokes equations. *Numerical Heat Transfer, Part B: Fundamentals*, 60(2):116–134, 2011.

[33] A. Gorobets, F. X. Trias, M. Soria, and A. Oliva. A scalable parallel Poisson solver for three-dimensional problems with one periodic direction. *Computers & Fluids*, 39(3):525–538, 2010.

[34] F. X. Trias, D. Folch, A. Gorobets, and A. Oliva. Building proper invariants for eddy-viscosity subgrid-scale models. *Physics of Fluids*, 27(6), 2015.

[35] S.B. Pope. *Turbulent flows*. Cambridge University Press, 2000.

[36] G. Grötzbach. Spatial resolution requirements for direct numerical simulation of the Rayleigh-BÃ©nard convection. *Journal of Computational Physics*, 49(2):241–264, 1983.

[37] N. Morozova, F. X. Trias, R. Capdevila, and A. Oliva. Investigating the capabilities of CFD-based data-driven models for indoor environmental design and control. In *Proceedings of 14th WCCM & ECCOMAS Congress 2020*, 2021.

[38] F. Dabbagh, F. X. Trias, A. Gorobets, and A. Oliva. On the evolution of flow topology in turbulent Rayleigh-Bénard convection. *Physics of Fluids*, 28(11), 2016.

[39] F. Chollet. keras. `https://github.com/fchollet/keras`, 2015.

[40] C. Cortes and V. Vapnik. Support-vector networks. In *Machine Learning*, pages 273–297, 1995.

[41] T. Hastie, R. Tibshirani, and J. H. Friedman. *The Elements of Statistical Learning*. Springer, 2009.

[42] C. E. Rasmussen. *Gaussian Processes in Machine Learning*, pages 63–71. Springer Berlin Heidelberg, 2004.

[43] F. Pedregosa, G. Varoquaux, A. Gramfort, V. Michel, B. Thirion, O. Grisel, M. Blondel, P. Prettenhofer, R. Weiss, V. Dubourg, J. Vanderplas, A. Passos, D. Cournapeau, M. Brucher, M. Perrot, and E. Duchesnay. Scikit-learn: Machine learning in Python. *Journal of Machine Learning Research*, 12:2825–2830, 2011.

[44] M. Stone. Cross-validatory choice and assessment of statistical predictions. *Journal of the Royal Statistical Society: Series B (Methodological)*, 36(2):111–133, 1974.

[45] S. Lundberg, G. Erion, H. Chen, A. DeGrave, J. Prutkin, B. Nair, R. Katz, J. Himmelfarb, N. Bansal, and S. Lee. From local explanations to global understanding with explainable AI for trees. *Nature Machine Intelligence*, 2:56â67, 2020.

[46] Y. Yao and D. K. Shekhar. State of the art review on model predictive control (MPC) in Heating Ventilation and Air-conditioning (HVAC) field. *Building and Environment*, 200:107952, 2021.

[47] Amazon Web Services. Amazon EC2 On-Demand Pricing. `https://aws.amazon.com/ec2/spot/pricing/`, 2021.

[48] P. O. Fanger, A. K. Melikov, H. Hanzawa, and J. Ring. Air turbulence and sensation of draught. *Energy and Buildings*, 12(1):21–39, 1988.

[49] G. A. Ganesh, S. L. Sinha, T. N. Verma, and S. K. Dewangan. Investigation of indoor environment quality and factors affecting human comfort: A critical review. *Building and Environment*, 204:108146, 2021.

4

Application of multi-fidelity approach for surrogate modeling of indoor airflow parameters in a ventilated room

Main content of this chapter has been part ially published in:

N. Morozova, F.X. Trias, V. Vanovskiy, C. Oliet and E. Burnaev. A CFD-based multi-fidelity surrogate model for prediction of flow parameters in a ventilated room. *In Proceedings of 8th European Congress on Computational Methods in Applied Sciences and Engineering*, June 5-9, 2022, Oslo, Norway.

Abstract: In this work, we present a multi-fidelity machine learning surrogate model, which predicts comfort-related flow parameters in a benchmark case of a ventilated room with a heated floor. The model uses coarse- and fine-grid CFD data with the LES turbulence model. The dataset is created by changing the width aspect ratio of the rooms, inlet flow velocity, and temperature of the hot floor. The surrogate model takes the values of temperature and velocity magnitude at four different cavity locations as inputs. These probes are located such that they could be replaced by actual sensor readings in a practical case. The model's output is a set of comfort-related flow parameters, such as the average Nusselt number on the hot wall, jet separation point, average kinetic energy, average enstrophy, and average temperature. We test three multi-fidelity approaches: Gaussian process regression (GPR) trained on both

high- and low-fidelity data without distinction between them, GPR with linear correction, and multi-fidelity GPR or co-kriging. The computational cost and accuracy of these approaches are compared with GPRs based only on high- or low-fidelity data. All of the tested multi-fidelity approaches successfully reduce the computational cost of dataset generation compared to high-fidelity GPR while maintaining the required level of accuracy. The co-kriging approach demonstrates the best trade-off between computational cost and accuracy.

4.1 Introduction

Modern heating ventilation and air conditioning (HVAC) systems are required to maintain a trade-off between maximizing human thermal comfort and minimizing energy consumption in buildings. Precise control and accurate design of the indoor environment are indispensable tools for achieving this trade-off.

Traditionally indoor environments are simulated using multizone models [1], zonal models [2], and computational fluid dynamics (CFD). Indoor environmental dynamics is usually a nonlinear, transient process that involves various complex physical phenomena, such as natural and forced convection. As a result, multizone and zonal models are often unable to achieve sufficient accuracy due to the simplifications adopted. On the other hand, CFD is a powerful tool for evaluating indoor air distribution, which provides a complete set of air parameters for the whole simulated domain. However, despite the sustained growth in computational power and advances in numerical algorithms, accurate CFD simulations are still prohibitively expensive [3,4] for most of the practical building applications and are mainly used for research and design of particular high-end buildings. Moreover, the growth of computational resources in the foreseeable future would not be enough to make CFD available for routine use in building applications [5]. As a result, new numerical models capable of providing accuracy comparable with high-fidelity CFD but at considerably lower computational cost are needed. From this perspective, surrogate modeling looks like an attractive option due to its low computational cost and comparable with CFD accuracy.

A surrogate model is an engineering method used when an outcome of interest cannot be easily measured or computed, so a model of the outcome is used instead. Surrogate models mimic the behavior of the high-fidelity simulation model as closely as possible while being considerably computationally cheaper to evaluate. Surrogate models are constructed using a data-driven, bottom-up approach using data analysis to find relations between system state variables without explicit knowledge of the physical behavior of the system. In order to construct these models, a comprehensive set of input-output data of the system is needed under all possible working conditions. Thus, the ease of development of surrogate models comes at the cost of reduced generalization capability compared to the classical modeling approaches. The accuracy of surrogate models decreases when training data deviates from testing data. Hence, it is critical to train these models with the data covering all the possible scenarios, which could be challenging, especially for indoor environmental applications that operate under a wide range of weather conditions throughout the year. However, difficulties in obtaining high-fidelity training data are compensated by the high accuracy and the low computational cost of the resulting models [6].

Because of its inexpensiveness, surrogate modeling is the central focus of the current research of built environment applications. Modern surrogate models are usually based on machine learning techniques. They are extensively used in building design, thermal load predictions, and model predictive control (MPC) [7]. The surrogate MPC model, which minimizes energy consumption in a generic office room, was developed by Kim *et al.* [8]. Wei *et al.* [9] and Asadi *et al.* [10] worked on the surrogate models which maintain thermal human comfort at an acceptable level and minimize thermal discomfort hours. Surrogate models for thermal load predictions were developed for a single building [11] and a non-residential district [12]. All of the aforementioned works show low computational cost and sufficient accuracy. However, these models primarily rely on other reduced-order models, experimental results, or historical data to generate the input-output data for their surrogate models.

Surrogate modeling is often built from and compared with CFD simulations, producing similarly accurate results. For example, Athavale *et al.* [13], and Fang *et al.* [14] compared different CFD-based surrogate models for temperature prediction in data centers and concluded that results produced by these models are in good agreement with the reference CFD data. Warey *et al.* [15] created an accurate model of vehicle cabin thermal comfort prediction using machine learning algorithms and high-fidelity CFD simulation results. Despite the practical significance of the aforementioned models, they work with specific indoor environments and cannot directly predict flow parameters in a more generic case. On the other hand, Zhang *et al.* [16] used a data-driven approach in general indoor environments with CFD as training data to solve the inverse design problem and identify a possible relationship between thermal comfort and inlet boundary condition. Tian *et al.* [17] used machine learning on CFD and experimental data to model indoor environment indicators in the stratified environments in order to evaluate human thermal comfort. Ding *et al.* [18] developed data-driven regression model for coupled indoor-outdoor flow analysis together with CFD simulations. The researchers note that CFD-based surrogate models produce accurate predictions at a low computational cost and could be a good alternative to classical modeling techniques.

Using CFD simulations for surrogate modeling usually results in high computational cost of dataset generation; thus, the increasing number of works is trying to optimize it by using a multi-fidelity approach. This approach combines a large number of computationally cheap low-fidelity simulations and a smaller number of expensive high-fidelity simulations, in way that ensures a trade-off between simulation cost and surrogate model accuracy. Multi-fidelity is a new approach in surrogate modeling, and not many works have been published on this topic yet. For instance, Lamberti & Gorlé [19] combined RANS and LES simulations in order to create a machine learning model which predicts wind loads on buildings. They showed that the proposed multi-fidelity framework has the potential to significantly reduce the number of expensive LES simulations while retaining a significantly higher accuracy than standard empirical models. The multi-fidelity kriging technique was used by Li *et al.* [20] for the optimization of high-speed train cabin ventilation system design, which led to significant savings of computational time. Zhang *et al.* [21] combined high-fidelity models using a CFD evaluation with fine grid and the low-fidelity models using the same CFD model with a coarse grid to optimize the aerodynamic shape of an airfoil, which improved optimization efficiency and outperformed the single-fidelity method. However, to the best of the author’s knowledge, multi-fidelity surrogate modeling has not yet been applied to simulations of the indoor environment.

In this work, we propose a CFD-based multi-fidelity surrogate model to predict comfort-related flow parameters in a ventilated room with a heated floor. The chosen test case is a classical benchmark test case [22] used by many researchers in the field of indoor environment for testing novel simulation methods [23–26]. This particular test configuration experiences both natural and forced convection phenomena, making it hard for the classical reduced-order models to achieve meaningful results and making expensive CFD simulations indispensable. However, the surrogate models have the capacity to drastically reduce the simulation cost while maintaining an acceptable level of accuracy. The model acts as a proof of concept. The model's inputs are values of temperature and velocity in the locations, which in a practical case could be replaced by sensor readings. The model's outputs are the flow parameters important for evaluating indoor thermal comfort. The main novelty of this work is the adoption of a multi-fidelity approach, which allows to substantially decrease the amount of computational resources spent on the dataset generation and increase the prediction capacity by amplifying the set of working conditions.

The content of this paper is organized as follows: Section 4.2 describes the governing equations and the details of the test case, Section 4.3 describes the numerical details of the CFD simulations and dataset generation; Section 4.4 describes the the developed surrogate models; Section 4.5 shows the results of the comparison of different multi- and single-fidelity approaches; Section 4.6 provides a discussion on model advantages and disadvantages and contains concluding remarks.

4.2 Test case description

This section describes the physical details of the simulated test case, the governing equations of the flow, and the details of the generated dataset.

4.2.1 Governing equations

We use the incompressible Navier-Stokes equations for a Newtonian fluid with constant physical properties. We adopt the Boussinesq approximation to account for the density variations due to temperature differences. Thermal radiation is neglected. Under these assumptions, the governing equations are

$$\nabla \cdot \mathbf{u} = 0, \tag{4.1}$$

$$\frac{\partial \mathbf{u}}{\partial t} + (\mathbf{u} \cdot \nabla)\mathbf{u} = \nu \nabla^2 \mathbf{u} - \nabla p + \beta \mathbf{g} \Delta T, \tag{4.2}$$

$$\frac{\partial T}{\partial t} + (\mathbf{u} \cdot \nabla) T = \alpha \nabla^2 T, \tag{4.3}$$

where $\mathbf{u} = (u, v, w)$ is the velocity vector in Cartesian coordinates $\mathbf{x} = (x, y, z)$, p the kinematic pressure, T the temperature, ν the kinematic viscosity, $\mathbf{g}$ the gravitational acceleration, β the thermal expansion coefficient and α the thermal diffusivity.

Hereafter, all the results are presented in dimensionless form. The reference values of time, velocity, temperature, and length are $t_{ref} = H/U_{ref}$, $U_{ref} = U_{in}$, ΔT, and H, respectively, where H is the cavity height, U_{in} is the inlet bulk velocity, $\Delta T = T_h - T_c$ is the temperature difference, T_h is the temperature of the hot wall, and T_c is the temperature of the cold wall.

4.2.2 Physical problem

The physical setup used in this work is a classical benchmark case of a three-dimensional ventilated cavity with a heated floor. This configuration was first studied experimentally by Blay *et al.* [22]. In our previous work [5] we conducted high-fidelity DNS simulations of this benchmark case in order to validate our CFD results. This flow configuration presents a mixed convection phenomenon, challenging due to the interaction of both natural and forced convection. It resembles an airflow in a middle section of a room with mixing ventilation and thermal exhausts. The geometry of the studied cavity is shown in Figure 4.1 (left). Cold air at $T_c = -0.5$ enters the cavity through the long thin inlet at the top of the left wall. The inlet velocity profile in the vertical (y) direction corresponds to a parabolic Poiseuille flow. The inlet slot has an aspect ratio $A_{in} = h_{in}/H = 0.018/1.04$. The air is discharged through the outlet slot with the aspect ratio $A_{out} = h_{out}/H = 0.024/1.04$ at the bottom of the right wall of the cavity. The bottom wall is maintained at a hot temperature of T_h, while the three other sidewalls are kept at the cold temperature of T_c.

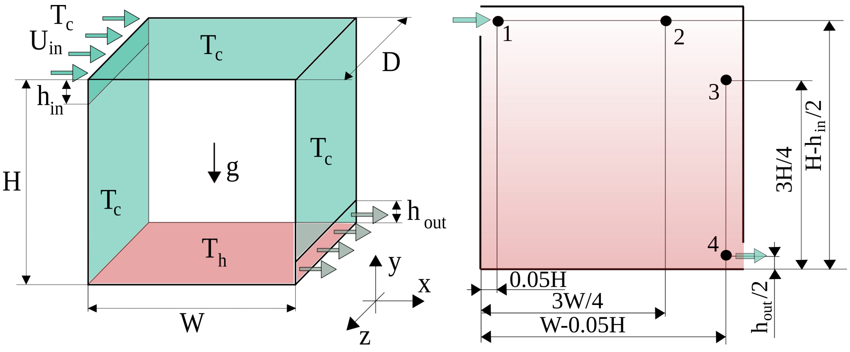

Figure 4.1: Left: geometry of the studied test case. Right: locations of the input data probes at the mid-depth cavity plane ($z = D/2$).

The cavity is filled with air ($Pr = \nu/\alpha = 0.71$). The depth aspect ratio of the cavity is $A_d = D/H = 0.3/1.04$. At the outlet, convective boundary conditions ($\partial\phi/\partial t + U_{in}\partial\phi/\partial x = 0$) are imposed for the velocity and temperature. No-slip boundary conditions are applied on the walls. The initial velocity field is set to zero and the initial temperature is set equal to the temperature at the cold wall. Periodic boundary conditions are used in the spanwise (z) direction.

4.3 Dataset generation

4.3.1 Description of the dataset

We build the input-output dataset by changing the width aspect ratio of the cavity $(A_w = W/H)$, the Rayleigh number based on the cavity height $Ra_H = g\beta\Delta TH^3/(\nu\alpha)$, and the Froude number based on the ratio between the bulk inlet and buoyant velocity ($Fr = U_{in}/U_{buo} = Re_H/\sqrt{Ra_H}$, $Re_H = U_{in}H/\nu$ is the Reynolds number based on the cavity height). Test case configurations used in the generation of the dataset are shown in Table 4.1.

Table 4.1: Combinations of the test case configurations for generating the CFD dataset. "LF" stands for low-fidelity (coarse-grid) "HF" for high-fidelity (fine-grid) CFD simulations. Each combination for A_w and Ra_H is tested for all of the 20 Fr numbers listed in the table.

A_w	Ra_H			
	1.5×10^8	6×10^8	2.4×10^9	9.6×10^9
0.25	HF+LF	HF+LF	HF+LF	LF
0.50	HF+LF	HF+LF	HF+LF	LF
1.00	HF+LF	HF+LF	HF+LF	LF
2.00	HF+LF	HF+LF	HF+LF	-
4.00	LF	LF	LF	-
$Fr = 0.15, 0.20, 0.25, ..., 0.55, 0.60, 0.70, ..., 1.50, 1.60$				
Total number of low-fidelity (LF) simulations				360
Total number of high-fidelity (HF) simulations				240
Total number of simulations				600

Chosen combinations of $A_w - Ra_H - Fr$ are realistic and relevant for indoor environmental applications. For example, assuming that the cavity height is 2.5 meters, the highest Rayleigh number (9.6×10^9) corresponds to a temperature difference of approximately $6°C$. On the other hand, the maximum Reynolds number based on the cavity height used in this work is 9.79×10^5. Considering the same height of 2.5 meters, it corresponds to an inlet velocity of $\approx 1m/s$s.

4.3.2 Input and output parameters

As input parameters of our surrogate model, we consider cavity width aspect ratio (A_w), temperature (T) and velocity magnitude (V) probes at four different locations on the mid-depth cavity plane ($z = D/2$). In a practical situation, apart from the cavity width aspect ratio, the values of the Froude and Rayleigh numbers are not available; hence they are discarded from the current study. In total, we use 9 ($A_w + 4T + 4V$) input parameters. The positions of the probes are shown in the figure 4.1 (right). The positions of the probes are chosen according to the results of our previous work [27]. The probes are located near the walls of the cavity in order to mimic the positions of real temperature and velocity sensors.

As the outputs of the model, we choose five global flow parameters: average Nusselt number on the hot wall - $<Nu>$, average kinetic energy - $<E>$, average enstrophy - $<\Omega>$, average temperature of the cavity - $<T_V>$, and the jet separation point - x_{sep}. They represent basic airflow properties and are relevant for thermal comfort [28]. The average Nusselt number is a measure of heat transfer. It is computed using the temperature gradient at the bottom wall surface:

$$<Nu>= -\frac{1}{WD}\int_{x=0}^{W}\int_{z=0}^{D}\frac{\partial<T>}{\partial y}dx\,dz \quad \text{at} \quad y=0, \tag{4.4}$$

where, the standard bracket "<>" notation is used for time-averaged values. The average temperature is the operative room temperature. It represents the thermal properties of the flow and is averaged over time and cavity volume:

$$<T_V>= \frac{1}{WHD}\int_{x=0}^{W}\int_{y=0}^{H}\int_{z=0}^{D}<T>dx\,dy\,dz. \tag{4.5}$$

Kinetic energy is a measure of the level of motion, whereas enstrophy is a measure of turbulence intensity. Both kinetic energy and enstrophy are directly related to draught and local discomfort. They are averaged over time and cavity volume and calculated as follows:

$$<E>= \frac{1}{WHD}\int_{x=0}^{W}\int_{y=0}^{H}\int_{z=0}^{D}\frac{<\mathbf{u}^2>}{2}dx\,dy\,dz \tag{4.6}$$

$$<\Omega>= \frac{1}{WHD}\int_{x=0}^{W}\int_{y=0}^{H}\int_{z=0}^{D}<\boldsymbol{\omega}^2>dx\,dy\,dz, \tag{4.7}$$

where $\boldsymbol{\omega} = \nabla \times \mathbf{u}$ is the vorticity. Jet separation point is an important parameter to measure velocity comfort in a room. It is determined as a point at the top cavity wall, where the wall-shear stress $<\tau_W>$ is equal to zero:

$$x_{sep} = x, \ \text{at} \ <\tau_W>= \int\frac{\partial<u>}{\partial y}dz = 0, y = H. \tag{4.8}$$

4.3.3 CFD simulations

To generate input and output data for the model, we use large-eddy simulations (LES) on staggered grids with second-order symmetry-preserving spatial discretization [29] and a one-parameter fully explicit second-order temporal discretization scheme [30]. To perform the simulations, we use an in-house CFD code developed by Gorobets *et al.* [31] with the LES-S3PQ turbulence model [32]. The choice of the turbulence model, type of spatial and temporal discretizations, and CFD software is based on the findings of our previous work [5], where we performed an extensive validation and mesh sensitivity analysis of the same test case ($Ra_H = 2.4 \times 10^9$, $Fr = 0.81$, and $A_w = 1$).

Choosing optimal grid discretization for the CFD simulations is a complex procedure, especially if one plans to perform many simulations simultaneously. On the one hand, the nature of LES turbulence modeling requires sufficient spatial discretization [33] in order to obtain accurate simulation results. On the other hand, the high computational cost of the simulations requires optimizing the grid size by tuning it to the physics and geometry of each test case. As a solution to this problem, we have developed an algorithm for the automatic mesh generation based on the variable physical parameters of the experiment (Fr, Ra_H, A_w), previously conducted validations [5], and desired level of mesh refinement.

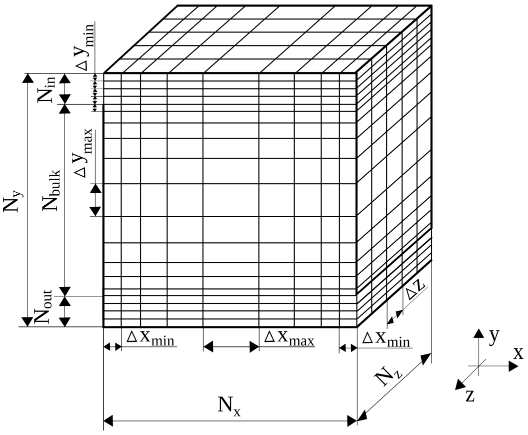

Figure 4.2: Schematic image of the computational grid used in the study.

All of the computational grids are structured and Cartesian. The schematic image of a computational grid used in this study is shown in Figure 4.2. The algorithm is determining the maximum cell size in each direction ($\Delta x_{max}, \Delta y_{max}, \Delta z$) using the Grötzbach estimate [34] based on the average Nusselt number derived from the results of our previous works [35,36]. The minimum cell size in the vertical direction (Δy_{min}) is determined by the flow in the inlet area, and the minimum cell size in the horizontal direction $\Delta x_{min} = 4\Delta y_{min}$. Once minimal and maximal cell sizes are found, the interpolation is done in order to approximate grid concentration factors. The detailed description of this algorithm could be found in our previous work [27].

The developed algorithm estimates the computational grid size required for a fully resolved flow simulation of a direct numerical simulation (DNS). However, the use of LES turbulence modeling allows coarser grids. The high-fidelity simulations are performed on the grids in which are each direction 3 times coarser than the corresponding DNS grids. Meanwhile, the low-fidelity simulations are performed in the grid 6 times coarser than DNS in every direction. According to our previous studies [5], where we performed and validated CFD simulations of the same test case, the computational grids used for high-fidelity simulations are sufficiently fine to achieve accurate results.

4.4 Surrogate models

This section describes the machine learning techniques we used to develop our surrogate model and the details on data preprocessing and metrics. Our work is based on the Gaussian process regression (GPR) approach, which is an attractive machine learning framework capable of constructing nonlinear regression models [37] with some guaranteed theoretical properties [38]. A significant advantage of GPR over other machine learning frameworks is the ability to treat variable fidelity data [38–41], which allows to reduce the computational cost of dataset generation. We investigate the computational complexity and compare accuracies of the following approaches: GPR for single-fidelity data [42], GPR with linear correction (LC GPR), and multi-fidelity GPR (MF GPR) or co-kriging [43]. All of the models use an open-source machine learning library scikit-learn [44].

4.4.1 Gaussian process regression for single-fidelity data

GPR [42] is a kernel-based machine learning technique for non-linear regression problems. A Gaussian Process (GP) is a set of random variables, such that any finite subset of these variables have a joint Gaussian distribution. We consider a training sample $DS = (\mathbf{X}^d, \mathbf{y}^d) = \{\mathbf{x}_i^d, {y^d}_i = y^d(\mathbf{x_i^d})_{i=1}^n$, where a point $\mathbf{x}^d \in \mathbb{X} \subseteq \mathbb{R}^d$ and a function value $y^d(\mathbf{x}^d) \in \mathbb{R}$. We assume that $y^d(\mathbf{x}^d) = f(\mathbf{x}^d) + \epsilon$, where $f(\mathbf{x})^d$ is a GP and ϵ is a Gaussian white noise with a variance σ^2. The goal is to construct a surrogate model for the target function $f(\mathbf{x}^d)$. As a distribution, a GP is characterized by its mean and covariance function:

$$k(x^d, x'^d) = cov(f(\mathbf{x}^d), f(\mathbf{x}'^d)) = \mathbb{E}((\mathbf{x}^d - \mathbb{E}(\mathbf{x}^d)(\mathbf{x}'^d - - - \mathbb{E}(\mathbf{x}'^d))) \tag{4.9}$$

To simplify the ++notations we assume that the mean value to be zero. We also assume that the covariance function belongs to the parametric family $k(x^d, x'^d) = k_\theta(x^d, x'^d)$ for some $\theta \in \Theta$. Then $y(\mathbf{x}^d)$ will be the GP with zero mean and the covariance function $cov(y^d(x^d), y^d(x'^d)) = k_\theta(x^d, x'^d) + \sigma^2 \delta(x^d \hat{a} x'^d)$, where $\delta(x^d \hat{a} x'^d)$ is the Kronecker delta. In this work we use Matérn covariance function, which is a generalization of commonly used squared exponential covariance function. It has an additional parameter ν_k which controls the smoothness of the resulting function. It is parameterized by a length-scale parameter l. The kernel is given by:

$$k(x^d, x'^d) = \frac{1}{\Gamma(\nu_k) 2^{\nu_k - 1}} \left(\frac{\sqrt{2\nu_k}}{l} d(x^d, x'^d) \right)^{\nu_k} K_{\nu_k} \left(\frac{\sqrt{2\nu_k}}{l} d(x^d, x'^d) \right), \tag{4.10}$$

where $d(x^d, x'^d)$ is the Euclidean distance, $K_{\nu_k}(\cdot)$ is a modified Bessel function, and $\Gamma(\cdot)$ is the gamma function. In our work we adopt $\nu_k = 3/2$, while l is approximated during the regression process.

GPR is a flexible approach capable of adapting to a wide range of problems by customizing kernel functions. Yet, GPR usually loses efficiency in high dimensional spaces with many input parameters and cannot handle large datasets. Usually, not more than a few thousand points are used when training Gaussian Process regression [38].

We test thee different single-fidelity GPR:

- HF-GPR - a model trained only high-fidelity (HF) data;
- LF-GPR - a model trained only on low-fidelity (LF) data;
- HFLF-GPR - a model trained on a mix of LF and HF data without distinguishing the data fidelity.

4.4.2 Gaussian process regression with linear correction

Now we consider the case of variable fidelity data: we have a sample of low-fidelity function evaluations $DS_l = (\mathbf{X}_l^d, \mathbf{y_l^d}) = \{\mathbf{x}_i^l, y_l^d(\mathbf{x}_i^l)\}_{i=1}^{n_l}$ and a sample of high-fidelity function evaluations $DS_h = (\mathbf{X}_h^d, \mathbf{y}_h^d) = \{\mathbf{x}_i^h, y_h(\mathbf{x}_i^h)\}_{i=1}^{n_h}$ with $\mathbf{x}_i^l, \mathbf{x}_i^h \in \mathbb{R}^d$, $y_l^d(\mathbf{x}_l^d), y_h^d(\mathbf{x}_h^d) \in \mathbb{R}$. The low-fidelity function $y_l^d(\mathbf{x}_l^d)$ and the high-fidelity function $y_h^d(\mathbf{x}_h^d)$ model the same physical phenomenon but with different fidelities. Using the samples of low- and high-fidelity finction values our aim is to construct a surrogate model of the high-fidelity function - $\hat{\mathbf{y}}_h^d \approx \mathbf{y}_h^d$.

This approach is a modification of single-fidelity GPR detailed in the Section 4.4.1. The developed surrogate model consists of three steps. In the first step we train a single-fidelity GPR model $M_l(\mathbf{X}_l^d, \mathbf{y}_l^d)$ on low-fidelity data and test it on high-fidelity data:

$$M_l(\mathbf{X}_l^d, \mathbf{y}_l^d) = \tilde{\mathbf{y}}_h^d, \tag{4.11}$$

where $\tilde{\mathbf{y}}_h^d$ is the test result on high-fidelity data. In the second step we estimate an error ($\Delta\mathbf{y}_h^d$) between the test results and the actual high-fidelity data and train a linear regression model $\Delta M(\mathbf{X}_h^d, \Delta\mathbf{y}_h^d)$ to predict this error:

$$\Delta\mathbf{y}_h^d = \mathbf{y}_h^d - \tilde{\mathbf{y}}_h^d = \mathbf{y}_h^d - M_l(\mathbf{X}_h^d) \tag{4.12}$$

$$\Delta M(\mathbf{X}_h^d, \Delta\mathbf{y}_h^d) = \Delta\tilde{\mathbf{y}}_h^d. \tag{4.13}$$

In the third step we correct the predictions of low-fidelity surrogate model for the the step one - $M_l(\mathbf{X}_h)$ using the error correction model from the step two:

$$\hat{\mathbf{y}}_h^d = \tilde{\mathbf{y}}_h^d + \Delta\tilde{\mathbf{y}}_h^d = M_l(\mathbf{X}_h^d) + \Delta M(\mathbf{X}_h^d), \tag{4.14}$$

where $\hat{\mathbf{y}}_h^d$ is the corrected prediction result. LC GPR approach allows to compensate simulation-induced errors and reduce the amount of high-fidelity data used in the model training process.

4.4.3 Multi-fidelity Gaussian process regression

In this work we consider a well-known multi-fidelity data model (co-kriging) [43]:

$$\mathbf{y}_l^d(\mathbf{x}^d) = f_l(\mathbf{x}^d) + \epsilon_l \tag{4.15}$$

$$\mathbf{y}_h^d(\mathbf{x}^d) = c y_l^d(\mathbf{x}^d) + y_c^d(\mathbf{x}^d), \tag{4.16}$$

where $y_c^d(\mathbf{x}^d) = f_d(\mathbf{x}^d) + \epsilon_c$ and c is an arbitrary constant. Here $f_l(\mathbf{x}^d)$, $f_d(\mathbf{x}^d)$ are the realizations of independent GP with zero means and covariance functions $k_l(x^d, x'^d)$ and $k_d(x^d, x'^d)$, respectively, and ϵ_l, ϵ_c are Gaussian white noise processes with variances σ_l^2 ans σ_c^2, respectively. We also set $\mathbf{X}^d = \begin{pmatrix}\mathbf{X}_l^d \\ \mathbf{X}_h^d\end{pmatrix}$, $\mathbf{y}^d = \begin{pmatrix}\mathbf{y}_l^d \\ \mathbf{y}_h^d\end{pmatrix}$. Then the posterior mean of high-fidelity values at next points has the form

$$\hat{\mathbf{y}}_h^d(\mathbf{X}_d^*) = \mathbf{K}(\mathbf{X}_d^*), \mathbf{X}^d)) \cdot \mathbf{K}^{-1}\mathbf{y}^d, \tag{4.17}$$

where

$$\mathbf{K}(\mathbf{X}_d^*, \mathbf{X}^d)) = \begin{pmatrix} c\mathbf{K}(\mathbf{X}_d^*, \mathbf{X}_l^d) & c^2\mathbf{K}_l(\mathbf{X}_d^*, \mathbf{X}_h^d) + \mathbf{K}_c(\mathbf{X}_d^*, \mathbf{X}_h^d) \end{pmatrix}, \tag{4.18}$$

$$\mathbf{K}(\mathbf{X}^d, \mathbf{X}^d)) = \begin{pmatrix} \mathbf{K}_l(\mathbf{X}_l^d, \mathbf{X}_l^d) & c\mathbf{K}_l(\mathbf{X}_l^d, \mathbf{X}_h^d) \\ c\mathbf{K}_l(\mathbf{X}_h^d, \mathbf{X}_l^d) & c^2\mathbf{K}_l^d(\mathbf{X}_h^d, \mathbf{X}_h^d) + \mathbf{K}_c(\mathbf{X}_h^d, \mathbf{X}_h^d) \end{pmatrix}, \tag{4.19}$$

$\mathbf{K}_l(\mathbf{X}_a, \mathbf{X}_b)$, $\mathbf{K}_c(\mathbf{X}_a, \mathbf{X}_b)$ are matrices of pairwise covariances between $y_l(\mathbf{x})$ and $y_c(\mathbf{x})$ and points from arbitrary samples $\mathbf{X}_a$ and $\mathbf{X}_b$, respectively. The posterior covariance function has the form

$$\mathbb{V}(\mathbf{X}^d) = c^2\mathbf{K}_l(\mathbf{X}_d^*, \mathbf{X}_d^*) + \mathbf{K}_c(\mathbf{X}_d^*, \mathbf{X}_d^*) - \mathbf{K}(\mathbf{X}_d^*, \mathbf{X}_d) \cdot \mathbf{K}^{-1} \cdot (\mathbf{K}(\mathbf{X}_d^*, \mathbf{X}^d))^T. \tag{4.20}$$

To evaluate the parameters of the covariance functions of GP $f_l(\mathbf{x}^d)$ and $f_c(\mathbf{x}^d)$, the following algorithm is used [40]:

1. Estimate parameters of the covariance function $k_l(x^d, x'^d)$ using the algorithm for the single-fidelity GPR, described in Section 4.4.1 with the sample $DS = DS_l$.
2. Calculate values of the posterior mean $\hat{\mathbf{y}_l^d}$ of the GP $y_l^d(\mathbf{x}^d)$ for $\mathbf{x}^d \in \mathbf{X}^d$.
3. Estimate parameters of the GP $y_c(\mathbf{x}^d)$ with a covariance function $k_c(x^d, x'^d)$ and the parameter c by maximizing likelihood estimation [38].

4.4.4 Data preprocessing and metrics

Data preprocessing is important for the correct performance of the data-driven models, because the difference in values between various parameters could be of several orders of magnitude [45]. In our work, we normalize all the input and output data to fit the range of $[-1, 1]$.

To improve the prediction results and avoid model overfitting (lack of generalization) we use cross-validation. In this study, we adopt a leave-one-out (LOO) cross-validation method. LOO is a specific case of the standard k-fold cross-validation [46]. For the LOO cross-validation at each training run, the learning set is created by taking all the samples except one, the validation set being the sample left out. Thus, for N samples, we have N different training sets and N different validation sets. This cross-validation procedure maximises the amount of data used for training since only one sample is removed from the training set. Moreover, LOO cross-validation is less biased because of the small difference in size between the training set used in each fold and the entire dataset. It is a suitable technique for small datasets. All of the high-fidelity data, not involved in the training process is used for testing. The size of the test dataset varies depending on the analysis performed (see Section 4.5 for details).

In order to quantify the accuracy of the model, we use mean relative error (MRE), which are designed as follows:

$$MRE(\phi) = \frac{1}{N}\sum_{i=1}^{N} \frac{|\phi_{CFD} - \phi_{SM}|}{|\phi_{CFD}|}, \tag{4.21}$$

where N is the number of samples in the test dataset, ϕ_{CFD} represents any one of the 5 comfort-related parameters calculated from the CFD simulations, and ϕ_{SM} represents a prediction from one of the surrogate models of any one of the 5 comfort-related parameters. We assume that less than 10% RE is acceptable for this model.

4.5 Results

This section analyzes the results obtained using different surrogate modeling techniques in terms of computational cost and accuracy. First, the comparison of the single-fidelity models is shown, then the multi-fidelity models are evaluated. All the results are averaged of 15 model runs.

4.5.1 Single-fidelity models

Here we present a comparison between two single-fidelity models, namely HF-GPR - a model trained only high-fidelity data and LF-GPR - a model trained only on low-fidelity data. Both models are tested on HF data. Figure 4.3 shows the MRE for each of the output flow parameters and different number of samples.

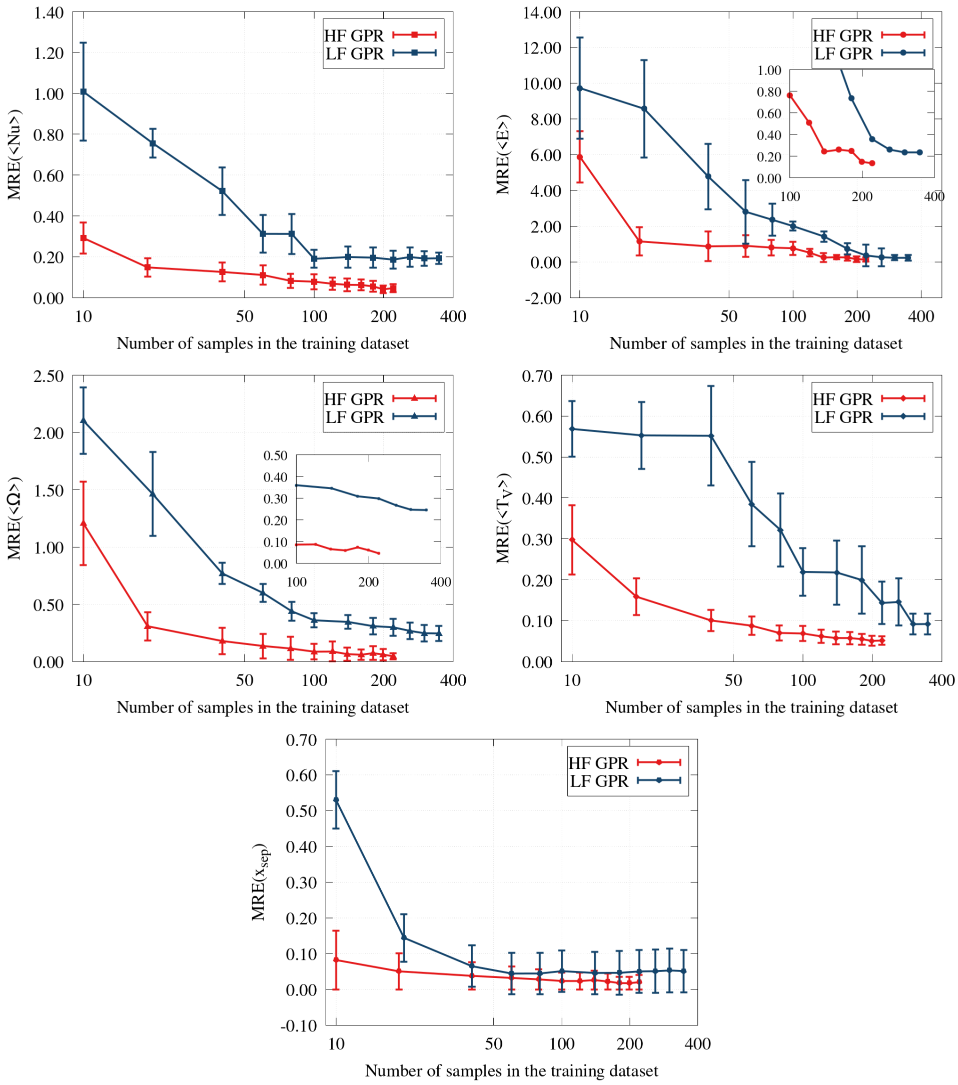

Figure 4.3: Mean relative error (MRE) of the studied flow parameters for different number of samples in the training dataset and different single-fidelity models. Top left: Nusselt number on the hot wall, $< Nu >$. Top right: average kinetic energy, $< E >$. Middle left: average enstrophy, $< \Omega >$. Middle right: average cavity temperature, $< T_V >$. Bottom: flow separation point, x_{sep}.

Nusselt number on the hot wall $< Nu >$ (Figure 4.3, top left) and flow separation point x_{sep} (Figure 4.3, bottom) show steady improvement of accuracy on both HF and LF surrogate models with the increase of the number of samples in the training dataset. However, even with the highest available number of samples, the LF model does not reach the same accuracy. Moreover, the prediction of flow separation point has a high variance. Kinetic energy $< E >$ (Figure 4.3, top right) and average enstrophy $< \Omega >$ (Figure 4.3, center left) show very high MREs on a low number of samples for both HF and LF models while significantly improving the results with the increasing number of samples. Again LF GPR does not reach the accuracy of HF GPR, which is caused by the model-induced errors. On the other hand, average $< T_V >$ (Figure 4.3, center right) is generally poorly predicted by the LF model; even though the results improve for larger training datasets, the prediction error variance is still high for LF GPR.

The performance of these two single-fidelity models establishes the baseline for further comparison between the different multi-fidelity approaches. The minimum size of the dataset is increased to 60 samples, since smaller datasets do not produce accurate results. The high-fidelity dataset is reduced to 130 data samples since all of the studied flow parameters converge to a steady prediction error at this dataset size. On the other hand, the low-fidelity dataset is used entirely since the computational cost of low-fidelity dataset is lower, and both $< \Omega >$ and $< T_V >$ did not reach a steady prediction error. The extensive comparison between different multi-fidelity approaches is made only for the enstrophy $< \Omega >$ since this flow parameter is the most illustrative example due to the highest LF and HF prediction differences. The results for other flow parameters are summarized in Table 4.3.

4.5.2 Multi-fidelity models

This subsection shows the comparison of the performance of different multi-fidelity models, detailed in Section 4.4, namely HFLF GPR single-fidelity GPR, which is trained both high- and low-fidelity data without distinction between them, GPR with linear correction (LC GPR), and multi-fidelity GPR (MF GPR). Figures 4.4-4.6 show the computational cost and accuracy of these models for different combinations of HF and LF data samples. Figure 4.7 shows the comparison of computational cost and accuracy between different modeling approaches using a different number of HF training data samples. Table 4.2 details the training dataset configurations which showed the best trade-off between computational cost and accuracy for different modeling approaches, and Table 4.3 summarises the accuracy of these models.

The main purpose of using the multi-fidelity approach is to reduce the computational cost of dataset generation without substantial loss of accuracy. As we have determined earlier, the HF surrogate models require 130 data samples for optimal performance. The average computational cost of one high-fidelity simulation is approximately 2700 core-hours, while the average cost of one low-fidelity simulation is 285 core-hours. These numbers are approximated using the whole datasets; however, the computational cost of each individual simulation depends on the physical and geometrical parameters of the test case and is highly variable. Nonetheless, the total computational cost of HF GPR model training is 351Kh, which is considered the maximum reference computational cost.

Figure 4.4 (left) shows the MRE of the average enstrophy $< \Omega >$ predicted using the HFLF GPR model. The horizontal axis is the total number of samples in the training dataset, and

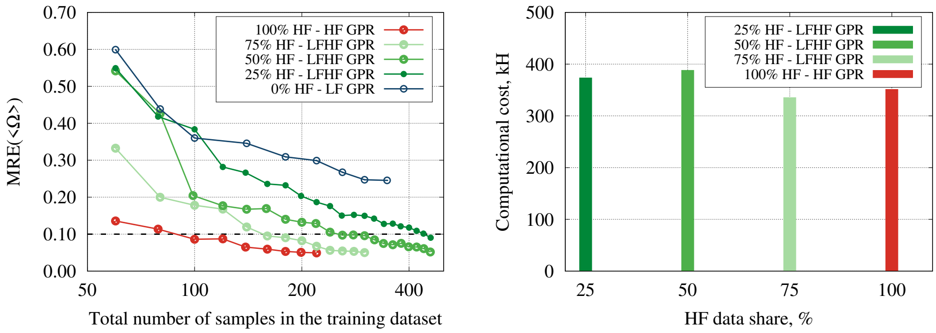

Figure 4.4: HFLF GPR model. Left: Mean relative error (MRE) of the average enstrophy $<\Omega>$ for a different total number of training samples and different percentage of high-fidelity (HF) samples. Right: Computational cost of dataset generation for accurate predictions (< 0.1) using different percentages of HF samples.

the vertical axis is $MRE(<\Omega>)$. Each plot line is obtained by changing the percentage of HF samples in the training dataset. The blue line (0% HF) is the single-fidelity model, trained only on LF data, while the red line (100% HF) is the HF model. The dotted black line marks the $MRE(<\Omega>) = 0.1$ - the required accuracy. Even the small number of HF samples introduced in the dataset successfully improves the model's accuracy to an acceptable level. Figure 4.4 (right) shows the computational cost, $[Kh]$ of CFD simulations, which were required to achieve the desired accuracy ($MRE < 0,1$) for each of the studied dataset configurations. Only the HFLF GPR model with 75% of HF samples could reduce the computational cost compared to the baseline HF model. The reason is that there is no distinction between the samples' fidelity; thus, the model's accuracy mostly depends on the amount of HF data samples.

The accuracy of the LC GPR model for the different number of samples in the training dataset and the different number of HF samples used in the correction step is shown in Figure 4.5 (left). This model is trained on the LF dataset, and the HF data is used inside a submodel that estimates and corrects the error between LF and HF predictions. LC GPR model has relatively low accuracy for the small number of samples, but when more than 200 samples are used, the accuracy is improved substantially. Moreover, the amount of HF samples in the correction step does not significantly influence the model's accuracy, which allows to reduce the computational cost of the dataset generation considerably. Figure 4.5 (right) shows the computational cost of different configurations of LC GPR models in comparison with single-fidelity models and the HFLF GPR model with 75% of HF samples (the only HFLF GPR configuration which was able to reduce the computational cost). LC GPR model has substantial advantages over both HF GPR and HFLF GPR, resulting in lower computational cost since it has achieved the required level of prediction error using only 25% of available HF samples.

Figure 4.6 (left) shows the MRE of the average enstrophy $< \Omega >$ predicted using the MF GPR model for different configurations of the training dataset. The model is performing

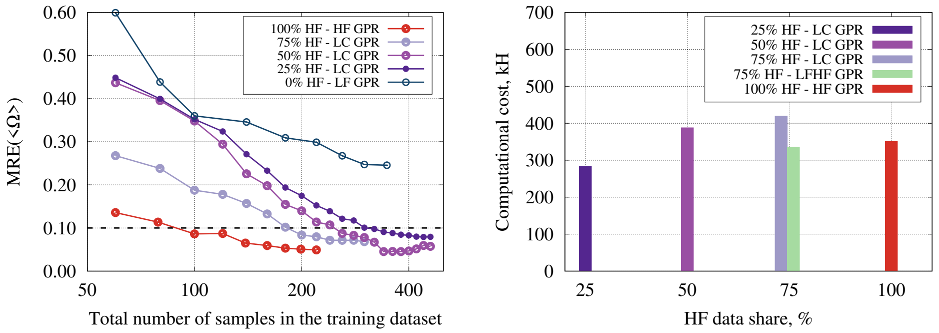

Figure 4.5: LC GPR model. Left: Mean relative error (MRE) of the average enstrophy $<\Omega>$ for different total number of training samples and different percentage of high-fidelity (HF) samples. Right: Computational cost of dataset generation for accurate predictions (< 0.1) using different percentage of HF samples.

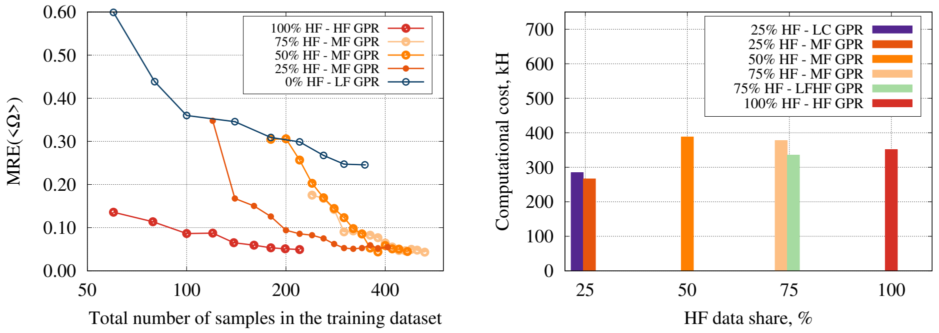

Figure 4.6: MF GPR model. Left: Mean relative error (MRE) of the average enstrophy $<\Omega>$ for different total number of training samples and different percentage of high-fidelity (HF) samples. Right: Computational cost of dataset generation for accurate predictions (< 0.1) using different percentage of HF samples.

similarly to the HFLF GPR and LC GPR; however, it needs smaller datasets in order to reach the desired prediction accuracy. This makes the model computationally cheaper than the others (Figure 4.6, right) since it requires less than 75 HF samples with a total of less than 300 samples to reach less than 10% of the MRE. This makes the MF GPR model the most efficient among the studied multi-fidelity models.

The computational cost of the dataset generation mostly depends on the number of HF simulations used; thus, it is interesting to see more closely how they influence the models'

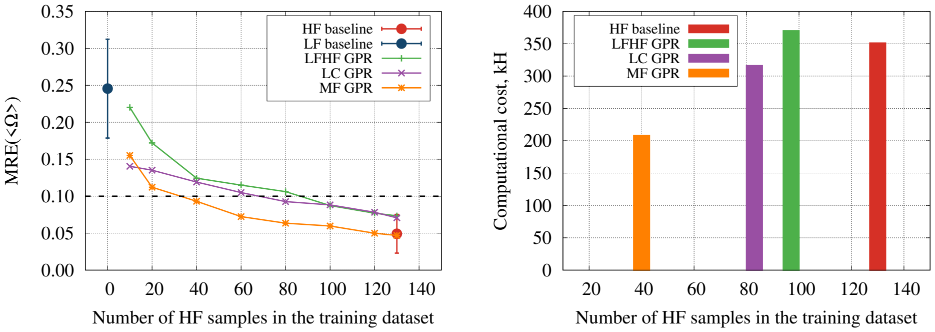

Figure 4.7: Left: Mean relative error (MRE) of the average enstrophy $< \Omega >$ for different number of high-fidelity (HF) training samples using different surrogate models. Right: Computational cost of dataset generation for accurate predictions (< 0.1) using different number HF samples with different surrogate models.

accuracy. In Figure 4.7 (left), we plot the $MRE(<\Omega>)$ for the studied multi-fidelity surrogate models using a different number of HF samples in the training dataset. The number of LF samples is always the same and is equal to 350 (all of the available LF samples). The big blue point on the left corresponds to the $MRE(<\Omega>)$, and its standard deviation obtained using the LF GPR model, while the red point on the right corresponds to the HF GPR model, respectively. The standard deviation of other points was omitted for the sake of clarity. The dotted black line marks the $MRE(<\Omega>) = 0.1$ - maximum acceptable error. All of the studied approaches show a similar tendency and steadily improve the prediction quality with the increase in the amount of HF data samples. However, the MF GPR model requires the least amount of HF samples to reach the required prediction accuracy, while the HFLF model needs considerably more samples. Figure 4.7 (right) shows the minimal computational cost at which the required accuracy was reached for the tests on the left. Both MF GPR and LC GPR models successfully reduce the computational cost of the dataset generation and prove their utility. These models are aware of the fidelity of each sample and learn from the existing dataset more efficiently. On the other hand, the HFLF GPR model results in a computational cost higher than the HF GPR model since it simply mixes all of the available data samples, which results in a higher computational cost.

Table 4.2 summarises the configurations of training datasets which showed the best trade-off between computational cost and accuracy for each of the studied surrogate modeling approaches. These configurations are based on the analysis of Figures 4.4-4.7, where the mean relative prediction error of the enstrophy was plotted. Table 4.3 summarises the prediction errors of all of the studied flow parameters, which are obtained using the models from Table 4.2. The multi-fidelity models have higher accuracy than the single-fidelity model trained only on HF data and reduced the computational cost compared to the baseline HF model. The prediction errors are very similar for all of the multi-fidelity models. However, the MF GPR

Table 4.2: Mean MRE error (see Table 4.3 for details), computational cost and number of low- and high-fidelity dataset samples of the studied models with the best trade-off between computational cost and accuracy.

Model	Samples			Comp cost, [Kh]	Mean MRE
	HF	LF	total		
HF GPR	130	-	130	351	0.060 ± 0.018
LF GPR	-	350	350	100	0.163 ± 0.043
HFLF GPR	120	40	160	335	0.083 ± 0.061
LC GPR	75	225	240	285	0.093 ± 0.050
MF GPR	40	350	380	208	0.080 ± 0.045

has the lowest dataset generation cost.

4.6 Discussion and conclusions

In this work, we presented a multi-fidelity machine learning surrogate model, combining a large number of computationally efficient coarse grid LES simulations with a smaller number of fine grid high-fidelity LES. The model predicts the comfort-related flow parameters in a benchmark three-dimensional ventilated cavity with a heated floor. The developed surrogate model provides almost instant accurate predictions using an ordinary office computer and requires less training computational resources than a similar single-fidelity model. The model's input parameters are the temperature and velocity magnitude values at different probe locations within the cavity domain. The output parameters are the average Nusselt number on the hot wall, the jet separation point, the average kinetic energy, the average enstrophy, and the average temperature of the cavity.

The input data of the developed model is structured to take the values of temperature and velocity in the locations, which could be replaced by sensor readings. This configuration of input data makes it possible to avoid costly CFD simulations at the model execution stage. Moreover, the output parameters of the model are directly related to the parameters of the thermal comfort, such as draft rating index (DR) [47] predicted mean vote (PMV) [28], and local thermal discomfort [48]. DR can be calculated using average kinetic energy $< E >$, average temperature $< T_V >$, and enstrophy $< \Omega >$. The average temperature is also used in calculations of PMV, while Nusselt number $< Nu >$ and flow separation point x_{sep} influence the local discomfort. This methodology for single-fidelity modeling was presented in our previous work [27]. The main purpose of this study is to improve the method by reducing the dataset generation cost using a multi-fidelity approach.

The main computational burden of the surrogate model is the cost of its development

Table 4.3: Mean relative prediction error (MRE) of the studied flow parameters for different models on the test data using training dataset configurations summarized in Table 4.2.

Model	MRE				
	$<Nu>$	$<E>$	$<\Omega>$	$<T_V>$	x_{sep}
HF GPR	0.046 ± 0.02	0.134 ± 0.03	0.046 ± 0.03	0.051 ± 0.01	0.021 ± 0.01
LF GPR	0.193 ± 0.03	0.234 ± 0.04	0.246 ± 0.07	0.092 ± 0.03	0.051 ± 0.06
HFLF GPR	0.042 ± 0.06	0.160 ± 0.09	0.093 ± 0.05	0.102 ± 0.09	0.019 ± 0.02
LC GPR	0.112 ± 0.06	0.145 ± 0.08	0.100 ± 0.05	0.088 ± 0.06	0.020 ± 0.04
MF GPR	0.092 ± 0.04	0.121 ± 0.07	0.093 ± 0.05	0.068 ± 0.04	0.026 ± 0.02

because, at this step, a comprehensive set of high-fidelity data is required. The training data was generated using the MareNostrum 4 supercomputer at the Barcelona Supercomputing Center. We limited ourselves to 750Kh core-hours computational resources; we spent 650Kh on 240 high-fidelity CFD simulations and 100Kh on 350 low-fidelity simulations. In order to create the dataset, we were changing three physical parameters of the cases - Froude number, Rayleigh number, and the cavity width aspect ratio. The range in which these parameters were varying was chosen to represent the realistic indoor environments. Test cases with high Rayleigh numbers and high width aspect ratios are considerably more computationally expensive than the others, and we did not compute them with high-fidelity CFD (see Table 4.1 for details). On the other hand, not only did the low-fidelity simulations completely cover the high-fidelity range, but we were able to run 110 additional simulations with high Rayleigh number and high width aspect ratios.

Three different multi-fidelity approaches, namely HFLF GPR, LC GPR, and MF GPR, were compared against two single-fidelity models - HF GPR and LF GPR. All of the models are based on Gaussian process regression with Matérn kernel function. All models were validated on high-fidelity data, and the validation results were averaged over 15 runs. HF GPR is the model trained only on high-fidelity data; it is the most accurate and computationally expensive among the studied models. LF GPR is trained only on low-fidelity data; the model is the least computationally expensive and least accurate; however, it has shown the required accuracy for predicting average temperature and jet separation point. HF GPR model required 130 training samples to reach the maximum accuracy, while LF GPR has used all of the available 350 low-fidelity samples.

The use of multi-fidelity models allowed us to reduce the computational cost of the dataset generation considerably. Even a simple HFLF GPR model, which mixes high- and low-fidelity data without distinguishing between them, appeared less computationally expensive than the baseline HF GPR model. HFLF GPR model needed 100 high-fidelity samples. More sophisticated multi-fidelity models like LC GPR and MF GRP required not more than 75 and 40 high-fidelity points, respectively, making them at least 1.5 times cheaper than the HF GPR model. LC GPR does not perform as well as the MF GPR since it is a simpler linear model. It corrects the estimated error between HF and LF data, which does not always improve the resulting accuracy because the errors are not necessarily proportional to the model input parameters. The MF GRP, or co-kriging, is a model that uses autocorrelation and cross-correlations between two variable types to make better predictions. This model has shown the best trade-off between computational cost and accuracy among studied multi-fidelity models. It has the potential to significantly reduce the number of costly CFD simulations needed for training while providing notably higher accuracy than standard reduced-order models. Nonetheless, a broad study is required on a proper choice of high-fidelity data in order to further reduce the computational cost and increase the covered range of the operation conditions.

The developed methodology is applicable to flow configurations with complex physical phenomena and commonly used indoor space geometrical configurations, like offices or classrooms. The methodology takes advantage of the detailed information about indoor airflow provided by accurate CFD simulations, which is usually not accessible by multizone and zonal reduced-order models. Moreover, in the case of public buildings, for example, offices, the type of ventilation systems and office geometry does not vary significantly inside one particular building, which makes the generation of the input data easier. As a result, a comprehensive dataset could easily be created. Therefore, the developed methodology could be used for applications where fast and accurate predictions are required, such as ventilation operation control. Moreover, the use of a multi-fidelity approach significantly reduces the computational cost of dataset generation, which is usually the most expensive step in surrogate modeling.

References

[1] J. Axley. Multizone airflow modeling in buildings: History and theory. *HVAC&R Research*, 13(6):907–928, 2007.

[2] A. C. Megri and H. Fariborz. Zonal modeling for simulating indoor environment of buildings: Review, recent developments, and applications. *HVAC&R Research*, 13(6):887–905, 2007.

[3] N. Morozova, R. Capdevila, F. X. Trias, and A. Oliva. Towards real-time CFD simulation of indoor environment. In *Proceedings of 10th International Conference on Computational Fluid Dynamics*, July 9-13, 2018.

[4] N. Morozova, R. Capdevila, F. X. Trias, and A. Oliva. On the feasibility of CFD for transient airflow simulations in buildings. In *Proceedings of Building Simulation 2019: 16th Conference of IBPSA*, September 2-4, 2019.

[5] N. Morozova, F. X. Trias, R. Capdevila, C. D. Pérez-Segarra, and A. Oliva. On the feasibility of affordable high-fidelity CFD simulations for indoor environment design and control. *Building and Environment*, 184:107144, 2020.

[6] A. Afram, F. Janabi-Sharifi, A. S. Fung, and K. Raahemifar. Artificial neural network (ANN) based model predictive control (MPC) and optimization of HVAC systems: A state of the art review and case study of a residential HVAC system. *Energy and Buildings*, 141:96–113, 2017.

[7] P. Westermann and R. Evins. Surrogate modelling for sustainable building design â A review. *Energy and Buildings*, 198:170–186, 2019.

[8] W. Kim, Y. Jeon, and Y. Kim. Simulation-based optimization of an integrated daylighting and HVAC system using the design of experiments method. *Applied Energy*, 162:666–674, 2016.

[9] X. Wei, A. Kusiak, M. Li, F. Tang, and Y. Zeng. Multi-objective optimization of the HVAC (heating, ventilation, and air conditioning) system performance. *Energy*, 83:294–306, 2015.

[10] E. Asadi, M. G. Da Silva, C. H. Antunes, L. Dias, and L. Glicksman. Multi-objective optimization for building retrofit: A model using genetic algorithm and artificial neural network and an application. *Energy and Buildings*, 81:444–456, 2014.

[11] H. Sözer and S. S. Aldin. Predicting the indoor thermal data for heating season based on short-term measurements to calibrate the simulation set-points. *Energy and Buildings*, 202, 2019.

[12] D. Koschwitz, E. Spinnräker, J. Frisch, and C. van Treeck. Long-term urban heating load predictions based on optimized retrofit orders: A cross-scenario analysis. *Energy and Buildings*, 208:109637, 2020.

[13] J. Athavale, M. Yoda, and Y. Joshi. Comparison of data driven modeling approaches for temperature prediction in data centers. *International Journal of Heat and Mass Transfer*, 135:1039–1052, 2019.

[14] Q. Fang, Z. Li, Y. Wang, M. Song, and J. Wang. A neural-network enhanced modeling method for real-time evaluation of the temperature distribution in a data center. *Neural Computing and Applications*, 31(12):8379–8391, 2019.

[15] A. Warey, S. Kaushik, B. Khalighi, M. Cruse, and G. Venkatesan. Data-driven prediction of vehicle cabin thermal comfort: using machine learning and high-fidelity simulation results. *International Journal of Heat and Mass Transfer*, 148:119083, 2020.

[16] T. H. Zhang and X. Y. You. Applying neural networks to solve the inverse problem of indoor environment. *Indoor and Built Environment*, 23(8):1187–1195, 2014.

[17] X. Tian, Y. Cheng, and Z. Lin. Modelling indoor environment indicators using artificial neural network in the stratified environments. *Building and Environment*, 208:108581, 2021.

[18] C. Ding and K. P. Lam. Data-driven model for cross ventilation potential in high-density cities based on coupled CFD simulation and machine learning. *Building and Environment*, 165:106394, 2019.

[19] C. Lamberti, G.and Gorlé. A multi-fidelity machine learning framework to predict wind loads on buildings. *Journal of Wind Engineering and Industrial Aerodynamics*, 214:104647, 2021.

[20] N. Li, L. Yang, X. Li, X. Li, J. Tu, and S. C. P. Cheung. Multi-objective optimization for designing of high-speed train cabin ventilation system using particle swarm optimization and multi-fidelity Kriging. *Building and Environment*, 155:161–174, 2019.

[21] X. Zhang, T. Xie, F.and Ji, Z. Zhu, and Y. Zheng. Multi-fidelity deep neural network surrogate model for aerodynamic shape optimization. *Computer Methods in Applied Mechanics and Engineering*, 373:113485, 2021.

[22] D. Blay, S. Mergui, J. L. Tuhault, and F. Penot. Experimental turbulent mixed convection created by confined buoyant wall jets. In *Proceedings of the First European Heat Transfer Conference, UK*, pages 821–828, 1992.

[23] Z. Zhang, W. Zhang, Z. J. Zhai, and Q. Y. Chen. Evaluation of various turbulence models in predicting airflow and turbulence in enclosed environments by CFD: Part-2: Comparison with experimental data from literature. *HVAC&R Research*, 13(6):871–886, 2007.

[24] A. Limane, H. Fellouah, and N. Galanis. Thermo-ventilation study by OpenFOAM of the airflow in a cavity with heated floor. *Building Simulation*, 8(3):271–283, 2015.

[25] G. Yang, Y. Huang, J. Wu, L. Zhang, G. Chen, R. Lv, and A. Cai. Experimental study and numerical models assessment of turbulent mixed convection heat transfer in a vertical open cavity. *Building and Environment*, 115:91–103, 2017.

[26] J. Y. Wu, R. R. Lv, Y. Y. Huang, and G. Yang. Flow Structure Transition and Hysteresis of Turbulent Mixed Convection Induced by a Transverse Buoyant Jet. *International Journal of Heat and Mass Transfer*, 177, 2021.

[27] N. Morozova, F. X. Trias, R. Capdevila, E. Schillaci, and A. Oliva. A CFD-based surrogate model for predicting flow parameters in a ventilated room using sensor readings. *Energy and Buildings*, 266:112146, 2022.

[28] Ergonomics of the thermal environment â Analytical determination and interpretation of thermal comfort using calculation of the PMV and PPD indices and local thermal comfort criteria. Standard, International Organization for Standardization, Geneva, CH, 2005.

[29] R. W. C. P. Verstappen and A. E. P. Veldman. Symmetry-preserving discretization of turbulent flow. *Journal of Computational Physics*, 187(1):343–368, 2003.

[30] F. X. Trias and O. Lehmkuhl. A self-adaptive strategy for the time integration of Navier-Stokes equations. *Numerical Heat Transfer, Part B: Fundamentals*, 60(2):116–134, 2011.

[31] A. Gorobets, F. X. Trias, M. Soria, and A. Oliva. A scalable parallel Poisson solver for three-dimensional problems with one periodic direction. *Computers & Fluids*, 39(3):525–538, 2010.

[32] F. X. Trias, D. Folch, A. Gorobets, and A. Oliva. Building proper invariants for eddy-viscosity subgrid-scale models. *Physics of Fluids*, 27(6), 2015.

[33] S.B. Pope. *Turbulent flows*. Cambridge University Press, 2000.

[34] G. Grötzbach. Spatial resolution requirements for direct numerical simulation of the Rayleigh-BÃ©nard convection. *Journal of Computational Physics*, 49(2):241–264, 1983.

[35] N. Morozova, F. X. Trias, R. Capdevila, and A. Oliva. Investigating the capabilities of CFD-based data-driven models for indoor environmental design and control. In *Proceedings of 14th WCCM & ECCOMAS Congress 2020*, 2021.

[36] N. Morozova, F. X. Trias, R. Capdevila, and A. Oliva. Data-driven prediction of flow parameters in a ventilated cavity. In *Proceedings of Building Simulation 2021: 17th Conference of IBPSA*, September 1-3, 2021.

[37] M. Belyaev, E. Burnaev, E. Kapushev, M. Panov, P. Prikhodko, D. Vetrov, and D. Yarotsky. GTApprox: Surrogate modeling for industrial design. *Advances in Engineering Software*, 102:29–39, 2016.

[38] A. Zaytsev and E. Burnaev. Large scale variable fidelity surrogate modeling. *Annals of Mathematics and Artificial Intelligence*, 81(1-2):167–186, 2017.

[39] A. Zaytsev and E. Burnaev. Minimax approach to variable fidelity data interpolation. In *Proceedings of the 20th International Conference on Artificial Intelligence and Statistics, AISTATS 2017*, volume 54, 2017.

[40] E. V. Burnaev and A. A. Zaytsev. Surrogate modeling of multifidelity data for large samples. *Journal of Communications Technology and Electronics*, 60(12):1348–1355, 2015.

[41] N. Klyuchnikov and E. Burnaev. Gaussian process classification for variable fidelity data. *Neurocomputing*, 397:345–355, 2020.

[42] C. E. Rasmussen. *Gaussian Processes in Machine Learning*, pages 63–71. Springer Berlin Heidelberg, 2004.

[43] M. C. Kennedy and A. O'Hagan. Predicting the output from a complex computer code when fast approximations are available. *Biometrika*, 87(1):1–13, 2000.

[44] F. Pedregosa, G. Varoquaux, A. Gramfort, V. Michel, B. Thirion, O. Grisel, M. Blondel, P. Prettenhofer, R. Weiss, V. Dubourg, J. Vanderplas, A. Passos, D. Cournapeau, M. Brucher, M. Perrot, and E. Duchesnay. Scikit-learn: Machine learning in Python. *Journal of Machine Learning Research*, 12:2825–2830, 2011.

[45] Q. Zhou and R. Ooka. Influence of data preprocessing on neural network performance for reproducing CFD simulations of non-isothermal indoor airflow distribution. *Energy and Buildings*, 230:110525, 2021.

[46] M. Stone. Cross-validatory choice and assessment of statistical predictions. *Journal of the Royal Statistical Society: Series B (Methodological)*, 36(2):111–133, 1974.

[47] P. O. Fanger, A. K. Melikov, H. Hanzawa, and J. Ring. Air turbulence and sensation of draught. *Energy and Buildings*, 12(1):21–39, 1988.

[48] G. A. Ganesh, S. L. Sinha, T. N. Verma, and S. K. Dewangan. Investigation of indoor environment quality and factors affecting human comfort: A critical review. *Building and Environment*, 204:108146, 2021.

5

Concluding remarks

This thesis presented the methodology for developing multi-fidelity surrogate models for fast predictions of an indoor environment. This work aimed to fill a gap in building simulation tools. Indoor environmental applications can be typically divided into three main types: conceptual design, detailed design, and control. Conceptual design, unlike detailed design, prioritizes computational cost over accuracy. Both of these applications typically need faster than real-time simulations in order to test different design decisions in a reasonable time frame; however, detailed design applications usually have more computational resources available. On the other hand, control applications not only have minimal computational resources (due to energy saving reasons) but must be faster than real-time and rely solely on data available onsite. Generally, indoor airflow in buildings is evaluated either by reduced-order models (typically multizone or zonal) or CFD. The former can provide very rapid predictions but offer limited information due to the assumptions required. On the other hand, CFD is a powerful but computationally expensive tool. As a result, more work is required to develop better models which reduce the computational cost of the simulations while maintaining their accuracy.

In the first part of the work, we analyzed the feasibility of using CFD simulations for routine use in building applications. Over the last decades, there have been significant changes in computer hardware and numerical algorithms, which have the potential to reduce the computational cost of the simulations and improve their robustness. Moreover, when one speaks about the high computational cost of CFD, they have in mind a detailed representation of indoor airflow. This level of detalization is often unnecessary for building applications, where integral flow parameters play a more critical role. With these two ideas in mind, we compared the performance of different LES, URANS, and no-model approaches with both staggered and collocated discretizations on a set of structured Cartesian non-uniform grids. We considered two representative test cases, namely differentially heated cavity and mixed convection.

LES and no-model approaches showed considerably higher accuracy than URANS. Even though URANS simulations were the least computationally expensive, their accuracy was often insufficient. The no-model approach produces similar to LES results but with a lower computational cost. Staggered symmetry-preserving discretization considerably improves the accuracy of coarse and extremely coarse grids. Based on the obtained run-times of the simulations and the building applications requirements, we conclude that fast, high-fidelity

CFD simulations on the office computers are neither feasible for the design nor control of indoor environments. Obtained run-times are too long to make CFD a primary tool for HVAC applications. We estimated the growth of computational resources in the future to determine when CFD would be available for routine use on office computers. The optimistic prediction estimates that CFD would be feasible for conceptual design in 5 years, detailed design in 10-20 years, and 10-25 years for MPC. The pessimistic prediction anticipates at least 15 years for the conceptual design, 25 years for the detailed design, and 35 years for control.

Based on the conclusion from the first part of our work, which stated infeasibility of affordable CFD simulation neither now nor in the near future, we developed a multi-fidelity surrogate model for a fast prediction of comfort-related flow parameters. We used the mixed convection test case from the first part of the work, which is essencially a ventilated room with a heated floor. The input parameters of the model are the values of the temperature and velocity magnitude at different probe locations within the cavity domain. The output parameters are the average Nusselt number on the hot wall, the jet separation point, the average kinetic energy, the average enstrophy, and the average temperature of the cavity. These are the same global integral parameters which were tested in the first part of the work. The developed model provides almost instant accurate predictions using an ordinary office computer.

In order to develop this model, we first tested different single-fidelity machine-learning frameworks. The gradient boosting regression outperformed other methods; however, gaussian process regression showed similar results. For this step, we used seven different probe locations. Next, in order to imitate the sensor readings, the number of probe locations was reduced to two, and the probes were placed near the ceiling and sidewalls of the cavity. Then the developed surrogate model was tested with the data from different combinations of sensor positions to determine the optimal areas of the sensor placement. Once the optimal position of the sensor was determined, we applied a multi-fidelity approach in order to reduce dataset generation cost, which is by far the most computationally expensive step in surrogate modeling.

Three different multi-fidelity approaches were compared against two single-fidelity models based only on high- and low-fidelity datasets. The high-fidelity model is the most accurate and computationally expensive among the studied approaches, while low-fidelity is the least computationally expensive and least accurate. The use of multi-fidelity models allowed us to reduce the computational cost of the dataset generation considerably. Even a simple model, which mixes high- and low-fidelity data without distinguishing between them, appeared less computationally expensive. More sophisticated multi-fidelity models like linear correction and co-kriging are at least 1.5 cheaper. The co-kriging model has shown the best trade-off between computational cost and accuracy among studied multi-fidelity models. It has the potential to significantly reduce the number of costly CFD simulations needed for training while providing notably higher accuracy than standard reduced-order models.

The developed methodology is applicable to flow configurations with complex physical phenomena and commonly used indoor space geometrical configurations, like offices or classrooms. The methodology takes advantage of the detailed information about indoor airflow provided by accurate CFD simulations, which is usually not accessible by multizone and zonal reduced-order models. Moreover, in the case of public buildings, for example, offices, the type of ventilation systems and office geometry does not vary significantly inside one particular building, which makes the generation of the input data easier. As a result, a comprehensive dataset could easily be created. Therefore, the developed methodology could be used for applications where fast and accurate predictions are required, such as ventilation operation control.

There are several possible future directions for this work. The most interesting one is to study the generalization properties of the developed methodology, for example, by combining displacement and mixing ventilation systems in one surrogate model. Moreover, the model could be further analyzed in terms of extrapolation capabilities. Another challenging problem is adapting the existing methodology to a direct prediction of comfort parameters, such as predicted mean vote. This model would require a more realistic dataset, which could be later validated in a practical case. Furthermore, the multi-fidelity part of the surrogate model could be improved by introducing more than two fidelity levels and a more broad study on a proper choice of high-fidelity data in order to further reduce the computational cost and increase the covered range of the operation conditions. And the last challenge is to adapt the existing methodology to optimize indoor airflow conditions to achieve human thermal comfort.

Appendix A

Results from the direct numerical simulation of a turbulent air-filled mixed convection

This appendix presents the results from the direct numerical simulation of a turbulent air-filled ($Pr = 0.71$) mixed convection at $Ra_H = 2.4 \times 10^9$, $Re_{h_{in}} = 684$ and $Fr_{h_{in}} = 5.24$. These results were used to validate the accuracy of the CFD simulations used in this thesis. The available data is shown here only partially; the complete dataset could be downloaded from [1].

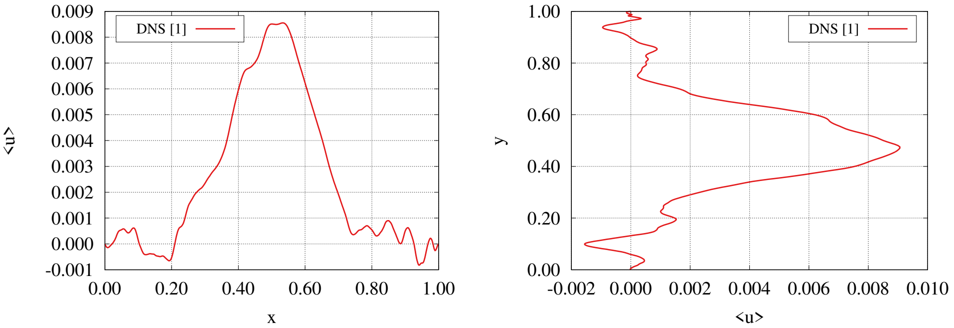

Figure A.1: Mean horizontal velocity in the median plan ($z = 0.15$). Left: at the cavity mid-height ($y = 0.50$). Right: at the cavity mid-width ($x = 0.50$).

We consider a cavity of height H, width W and depth D filled with an incompressible Newtonian viscous fluid. The geometry of the problem is displayed in Figure 4.1 (right). The Boussinesq approximation is used to account for the density variations. Thermal radiation is neglected. The configuration considered here resembles the experimental set-up performed by Blay *et al.* [2]. The height aspect ratio of the cavity is $A_h = H/W = 1$ and the depth aspect ratio is $A_d = D/W = 0.3/1.04$. Cold air at $T_c = -0.5$ enters the cavity through the long thin inlet at the top of the left wall. The inlet velocity profile in the vertical (y) direction corresponds to a parabolic Poiseuille flow with a bulk velocity $U_{in} = 1$. The inlet slot has an aspect ratio $A_{in} = h_{in}/H = 0.018/1.04$.

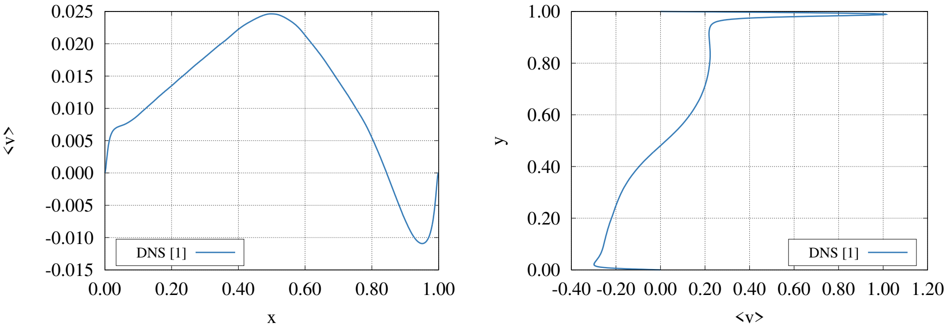

Figure A.2: Mean vertical velocity in the median plan ($z = 0.15$). Left: at the cavity mid-height ($y = 0.50$). Right: at the cavity mid-width ($x = 0.50$).

The air is discharged through the outlet with an aspect ratio $A_{out} = h_{out}/H = 0.024/1.04$ at the bottom of the right wall of the cavity. The bottom wall is maintained at a hot temperature of $T_h = 0.5$, while the three other sidewalls are kept at the cold temperature of $T_c = -0.5$. Periodic boundary conditions are used in the spanwise (z) direction. At the outlet, convective boundary conditions $(\partial\phi/\partial t + U_{in}\partial\phi/\partial x = 0)$ are imposed for the velocity and temperature. No-slip boundary conditions are applied on the walls. The initial velocity field is set to zero and the initial temperature is set equal to the temperature at the cold wall.

Hereafter, the results are presented in dimensionless form. The reference values used for non-dimensionalizing are the cavity height H, the time $t_{ref} = H/U_{ref}$, the velocity $U_{ref} = U_{in}$ and the temperature difference ΔT. Cartesian structured grid detailed in Table 2.2 was used. The grid is uniform in the spanwise (z) direction. In the horizontal (x) direction grids it is refined near the walls using the hyperbolic tangent function given in equation (2.4) with a concentration factor $\gamma_x = 1.5$. In the vertical (y) direction the grid is uniform in the zones of inlet (N_{in}) and outlet (N_{out}) and refined near the lateral walls in the bulk part $(\gamma_y = 2)$. The time integration period for this simulation is 500 non-dimensional time units.

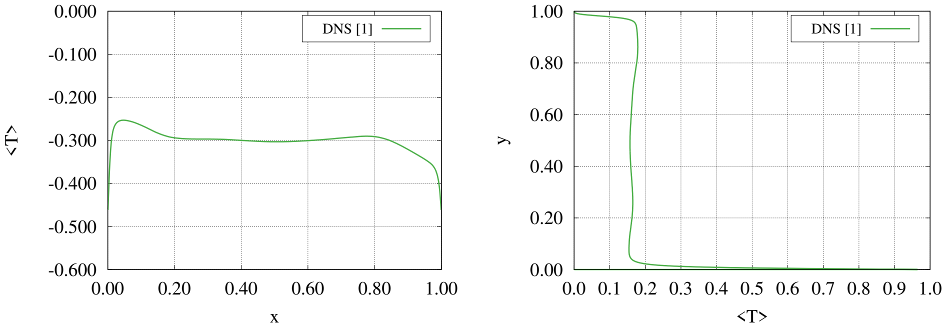

Figure A.3: Mean temperature in the median plan ($z = 0.15$). Left: at the cavity mid-height ($y = 0.50$). Right: at the cavity mid-width ($x = 0.50$).

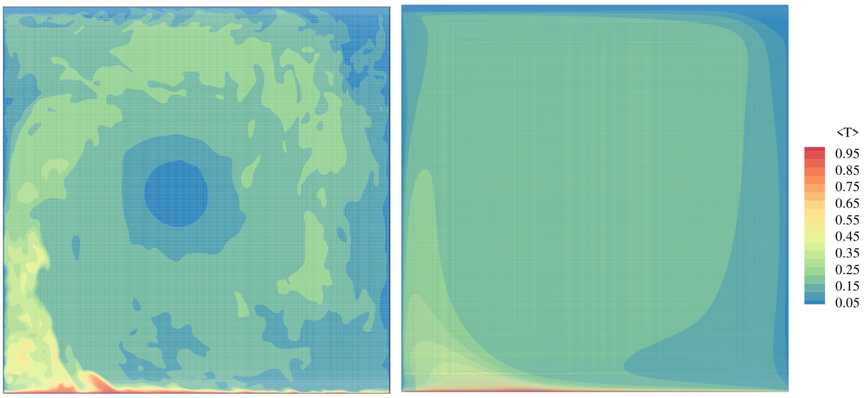

Figure A.4: Instantaneous (left) and averaged (right) temperature fields in the median plan ($z = 0.15$).

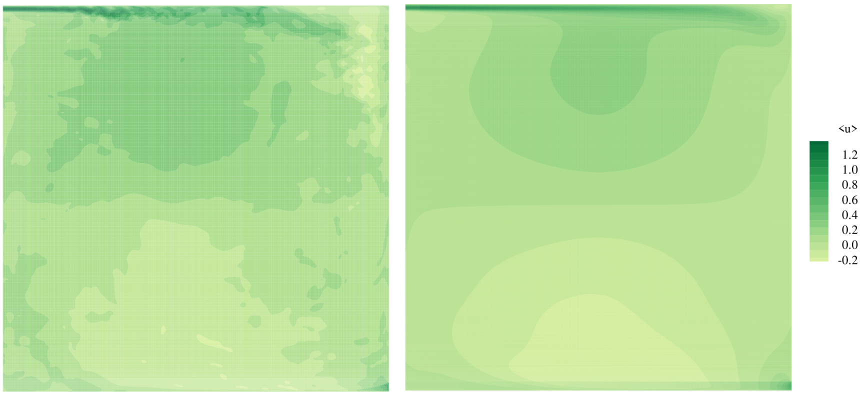

Figure A.5: Instantaneous (left) and averaged (right) horizontal velocity fields in the median plan ($z = 0.15$).

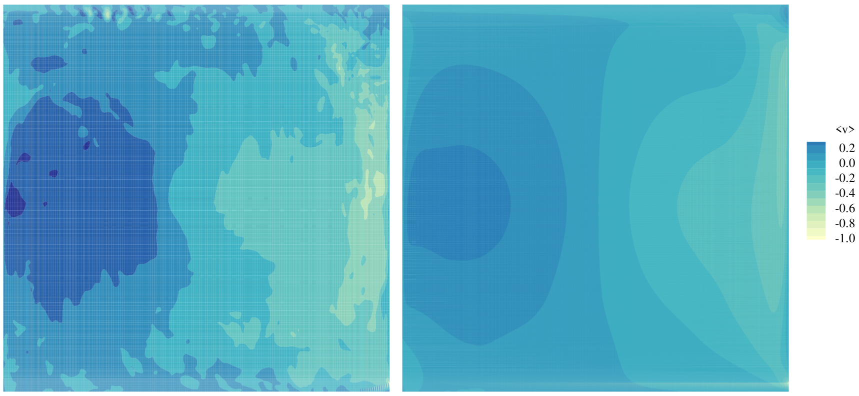

Figure A.6: Instantaneous (left) and averaged (right) vertical velocity fields in the median plan ($z = 0.15$).

References

[1] N. Morozova, F. X. Trias, R. Capdevila, and A. Oliva. Results from a turbulent air-filled $(Pr = 0.71)$ mixed convection at $Ra = 2.4 \times 10^9$ and $Fr = 5.24$ (both based on the inlet height). `http://www.cttc.upc.edu/downloads/MC_RA2_4e9_FR5_24/`, 2020.

[2] D. Blay, S. Mergui, J. L. Tuhault, and F. Penot. Experimental turbulent mixed convection created by confined buoyant wall jets. In *Proceedings of the First European Heat Transfer Conference, UK*, pages 821–828, 1992.